Dissertation zur Erlangung des Doktorgrades

der Fakultät für Chemie und Pharamazie

der Ludwig-Maximilians-Universität München

Transmission Electron Microscopic Investigation of Several Nanostructured Photoelectrodes for Photoelectrochemical Water Splitting

Alexander Müller

aus

Augsburg, Deutschland

2015

Erklärung

Diese Dissertation wurde im Sinne von §7 der Promotionsordnung vom 28. November 2011 von Frau Prof. Dr. Christina Scheu betreut.

Eidesstattliche Versicherung

Diese Dissertation wurde eigenhändig und ohne unerlaubte Hilfe erarbeitet.

München, den 27.10.2015

Dissertation eingereicht am: 27.10.2015

1. Gutachter: Prof. Dr. Christina Scheu

2. Gutachter: Dr. Dina Fattakhova-Rohlfing

Mündliche Prüfung: 26.11.2015

Table of Contents

Abbreviations

ADF	annular dark-field
ATO	antimony-doped tin oxide
APCVD	atmospheric pressure chemical vapor deposition
BF	bright field
CCD	charge-coupled device
CMOS	complementary metal-oxide semiconductor
CTEM	conventional transmission electron microscopy
CTF	contrast transfer function
CV	current-voltage
DF	dark field
EDX	energy-dispersive X-ray spectroscopy
EELS	electron energy-loss spectroscopy
EQE	external quantum efficiency
FEG	field-emission gun
FT	Fourier transformation
FTO	fluorine-doped tin oxide
GIXRD	grazing incidence X-ray diffraction
HAADF	high-angle annular dark field
HER	hydrogen evolution reaction
HRTEM	high-resolution transmission electron microscopy
IMPS	intensity-modulated photocurrent spectroscopy
I_{inst}	instantaneous photocurrent
IPCE	incident photon-to-current efficiency
IQE	internal quantum efficiency
LED	light emitting diode

η_{lh}	light harvesting efficiency
LSPR	localized surface plasmon resonance
MMA	methyl methacrylate
PMMA	poly(methyl methacrylate)
NHE	normal hydrogen electrode
OCV	open-circuit voltage
OER	oxygen evolution reaction
PEIS	photoelectrochemical impedance spectroscopy
RHE	reversible hydrogen electrode
RF	radio frequency
SAED	selected-area electron diffraction
SDD	silicon drift detector
SDS	sodium dodecyl sulfate
SEM	scanning electron microscopy
SPR	surface plasmon resonance
η_{sep}	separation efficiency
I_{ss}	steady-state photocurrent
STEM	scanning transmission electron microscopy
TEM	transmission electron microscopy
$\eta_{transfer}$	transfer efficiency
UV-Vis	ultraviolet-visible
X-FEG	extreme field-emission gun
XRD	X-ray diffraction
XPS	X-ray photoelectron spectroscopy

Abstract

Most renewable energy sources suffer from intermittency and have to be coupled with sophisticated energy conversion and storage technologies. An elegant solution is offered by photoelectrochemical water splitting, where solar energy is directly converted into chemical energy by splitting water into oxygen and the energy carrier hydrogen. Photoelectrochemical water splitting requires two photoelectrodes which are immersed in an aqueous electrolyte. These photoelectrodes are semiconductors with valence and conduction bands straddling the redox potential of water. Upon illumination, electrons and holes are produced, separated and transferred to the electrolyte, leading to the evolution of oxygen at the photoanode and the evolution of hydrogen at the photocathode. The resulting hydrogen can be stored, transported and then either burnt in fuel cells to regain electrical energy or used for industrial applications like the Haber-Bosch process. The photoelectrodes are often nanostructured to increase the surface area, at which the reaction takes place. This strategy has been realized with several morphologies such as nanotubes, inverse opals, etc. and has often lead to performance increases of several hundred percent.

Therefore, detailed knowledge of the morphology is important and can be obtained by scanning electron microscopy (SEM) and transmission electron microscopy (TEM). TEM is a powerful technique that allows imaging samples with a resolution down to the sub-Ångstrom scale. In addition, TEM can be combined with spectroscopic methods such as electron energy-loss spectroscopy (EELS) and energy-dispersive X-ray spectroscopy (EDX) to quantify the chemical composition. In this thesis, three different materials systems were studied by TEM: noble metal nanoparticles on TiO_2 for hydrogen evolution with the sacrificial agent MeOH, Fe_2O_3/WO_3 dual absorber photoanodes and photocathodes out of the novel material FeCrAl oxide.

Titania is one of the most researched photoanode materials. However, it only absorbs UV light. Au and Au/Ag core-shell nanoparticles were deposited by the project partners Michael Karnahl and Sandra Peglow of the LIKAT and the INP Greifswald, respectively, on anatase thin films by photodeposition and radio frequency magnetron sputtering. These noble metal nanoparticles absorb visible light by surface plasmon resonance and also act as co-catalysts for electrons excited in the titania and injected into them. Cross-section were prepared for a detailed TEM investigation of the microstructure. The distribution of the nanoparticles varied greatly with the synthesis method, as photodeposited particles grew in and on top of the titania, whereas the plasma-deposited nanoparticles only grew on top. Different growth and coarsening mechanisms could be identified and correlated to the synthesis conditions by careful particle size distribution determination. In addition to defect-free nanoparticles, several defects such as five-fold twinning, grain boundaries and stacking faults were found.

The TEM analysis was complemented by optical absorption and photocatalysis measurements, and the synthesis as well as the properties could be correlated to microstructural features.

Due to its narrow band gap, hematite is a popular photoanode material. However, it also has several disadvantages, which were addressed by several studies. Tin-doping increased the transfer efficiency and therefore the photocurrent, with the tin being enriched at the surface of the hematite nanoparticles and hinting at a structure-function relationship. Deposition of a Co_3O_4 co-catalyst and the introduction of a conductive scaffold all further increased the photocurrent. Another performance-increasing approach, combining multiple photocatalytically active materials, was tested with Fe_2O_3/WO_3 dual absorbers prepared by Ilina Kondofersky of the group of Prof. Thomas Bein. WO_3 was systematically applied as a scaffold and/or as a surface treatment. The arrangement of the different materials and the interfaces between them was studied in detail by TEM. Both the host-guest approach and the surface treatment strongly increased the performance compared to the pure materials and several beneficial interactions could be identified. For example, WO_3 strongly scatters visible light, resulting in increased absorption by Fe_2O_3 and higher current densities. We also determined a cathodic shift in the onset potential to 0.8 V and, compared to pure Fe_2O_3, increased transfer rates of up to 88 %, and can therefore conclude that the Fe_2O_3/WO_3 dual absorbers are a very promising system.

In spite of all the different performance-enhancing strategies developed so far, it is becoming apparent that all currently available materials, regardless of how heavily they are improved, will not reach sufficient performances. This has led to the search for novel materials and in this thesis, meso- and macroporous photocathodes with the overall stoichiometry $Fe_{0.84}Cr_{1.0}Al_{0.16}O_3$ were investigated in close cooperation with Ilina Kondofersky. Using TEM cross-sections, a phase separation into Fe- and Cr-rich phases was observed for both morphologies and could be correlated to the precursor stabilities. In comparison to the mesoporous layer, the macroporous photocathode had a significantly increased charge collection efficiency and therefore performance, proving the benefits of tuning the morphology.

In all studies, performance-increasing strategies were successfully applied and we found the performance to depend heavily on the morphologies. By combining the results of all techniques, insight into the complex interplay between synthesis conditions, morphology and properties could be achieved and the gained knowledge is expected to benefit future work.

1. Introduction

The current energy mix, which relies heavily on fossil fuels, coal and nuclear power, is proving unsustainable due to environmental pollution, climate change, and eventual resource depletion.[1–3] As a result, research into alternative, sustainable energy sources is thriving and the most promising approaches utilize wind power, solar power, geothermal power, hydropower or biomass/biogenic waste.[1,3] All of these technologies are by design CO_2 neutral during their operation and do not produce any toxic products. Photovoltaic cells, which harvest nearly limitless solar energy, are particularly promising.[4,5] Compared to the other methods, they are cheap to produce, usable in remote locations, do not require any infrastructure, are non-polluting, silent and have low operating costs. Common and cheap commercial products reach conversion efficiencies of around 20 % and in combination with government programs supporting their installation, are becoming more and more common. However, the huge leaps in installed capacity seen in the last few years have led to grid stability and intermittency problems. On sunny days, the contribution of solar power to the energy mix surges, and other, conventional sources have to be shut down to prevent overloading the grid. However, all power plants except for those burning natural gas cannot be shut on and off as quickly as would be required, and as a result, the grid becomes unstable. On the other hand, most energy is used at night, when solar cells do not contribute to the energy mix but people are at home and turn on lights, run washing machines, cook and so on.

A solution to both problems is the development and wide-spread installation of energy storage technologies.[6–8] Multiple approaches are being developed, and all but capacitators rely on converting electricity into another form of power. Conversion into thermal power is an option, as is the conversion into mechanical power by flywheels, pumped storage hydroelectricity or compressed air storage, and into chemical power by power-to-gas technologies or the production of hydrogen. The last approach in particular is very promising, as hydrogen is not only used for industrial applications like the Haber-Bosch process or hydrocracking, but can also efficiently be converted into electrical energy by fuel cells. [2,9–12]

A few technologies aim to utilize solar power for the production of hydrogen from water. Among them are solar thermochemical,[13] photovoltaic/electrolysis,[14,15] and photoelectrochemical water splitting.[16] The last of these approaches in particular is very elegant, as it directly converts solar into chemical energy by splitting water into hydrogen and oxygen at a semiconductor photoelectrode.[15] The semiconductor is chosen so that valence and conduction band straddle the redox energy levels of hydrogen and oxygen and should fulfill several other factors such as good light absorption properties, good charge conductivity, fast surface kinetics, non-toxicity, and stability in aqueous solutions. Several promising candidates are being investigated with these requirements in mind, among them $BiVO_4$, α-Fe_2O_3, WO_3 and TiO_2 as photoanode materials and p-Si, Cu_2O and $CuFeO_2$ as photocathode

materials.[17] However, none of the materials achieves all these requirements. α-Fe_2O_3, for example, absorbs a large portion of the solar spectrum, but suffers from low light absorption coefficients and poor major carrier conductivity,[18] whereas TiO_2 offers excellent charge separation and transport, but has a large band gap and only absorbs a small fraction of the solar spectrum.[19–22] Strategies to mitigate such problems have been in development for decades and have led to drastic performance increases.[15,17] One very popular approach is to increase the surface area of the material, typically by structuring it on the nanoscale.[23–25] This leads to beneficial effects such as shortened carrier collection pathways, reducing bulk recombination, and improved light distribution due to scattering, but can also have detrimental effects such as increased surface recombination or reduced space charge layer thickness.[25] Often, the benefits outweigh the negative aspects and nanostructuring is a very promising performance-enhancing approach.

1.1. Aim of the Thesis

The performance of all photoelectrodes heavily depends on its structure and understanding a photoelectrode's behavior requires investigating it in depth. One of the most powerful methods available is transmission electron microscopy (TEM), which allows imaging samples with a resolution on the Ångstrom-scale. It can also be coupled with spectroscopic methods such as electron energy-loss spectroscopy (EELS) and energy-dispersive X-ray spectroscopy (EDX), two methods that can yield the local chemical composition. This comprehension often gives insight into how to further improve the nano- or macrostructure, and doing so requires relating it to the synthesis protocol. The goal of this thesis therefore is to, by combining a complete structural investigation with knowledge of the synthesis protocol and measurements of the properties, identify correlations between these three fields.

Four photoelectrode systems were investigated. The first, stemming from a collaboration with the groups of Volker Brüser and Henrik Junge and described in Chapter 4, details a strategy aiming to improve light absorption in the established photoabsorber material titania. Titania only absorbs UV lights, and deposition of noble metal nanoparticles, which can absorb visible light via localized surface plasmon resonance and then inject electrons into the titania, can extends this range. In this chapter, several parameters such as the noble metal nanoparticle distribution, particle size distribution, noble metal loading, defect structures and crystallographic structures at interfaces were investigated, mostly by TEM, and connected with optical absorption and photocatalysis measurements. All other materials systems were investigated jointly with the groups of Thomas Bein and Dina Fattakhova-Rohlfing. Further strategies aiming to improve a material, in this case α-Fe_2O_3, are detailed in Chapter 5.[26–28] The transfer efficiency and therefore the performance could be significantly increased by doping with Sn, which accumulated at the surface of the hematite nanoparticles.[26] The performance could be further enhanced by adding Co_3O_4 as a co-catalyst and by depositing it onto a conducting scaffold.[27,28] A different approach is the combination of several

photoabsorber materials that have complementary properties. In Chapter 6, several Fe_2O_3/WO_3 dual absorbers were synthesized and the effect of different WO_3 morphologies, which was applied both as a macroporous scaffold and as a surface treatment, was analyzed. Regardless of all performance-enhancing strategies, the viability of all material systems investigated so far is insufficient and the development of new materials systems is becoming a priority. Successful nanostructuring of the novel photocathode material FeCrAl oxide is described in Chapter 7. In all cases, the structural investigation could be correlated to both synthesis conditions and the catalytic performance, resulting in a better understanding of the materials systems and opening the door for future improvement.

1.2. References

(1) Foley, T.; Thornton, K.; Hinrichs-Rahlwes, R.; Sawyer, S.; Sander, M.; Taylor, R.; Teske, S.; Lehmann, H.; Alers, M.; Hales, D. *Renewables 2015 Global Status Report*; 2015.

(2) Armaroli, N.; Balzani, V. *Angew. Chemie - Int. Ed.* **2007**, *46* (1-2), 52.

(3) U.S. Energy Information Agency. *International Energy Outlook 2014*; 2014.

(4) El Chaar, L.; Lamont, L. A.; El Zein, N. *Renew. Sustain. Energy Rev.* **2011**, *15* (5), 2165.

(5) Parida, B.; Iniyan, S.; Goic, R. *Renew. Sustain. Energy Rev.* **2011**, *15* (3), 1625.

(6) Akinyele, D. O.; Rayudu, R. K. *Sustain. Energy Technol. Assessments* **2014**, *8*, 74.

(7) Díaz-González, F.; Sumper, A.; Gomis-Bellmunt, O.; Villafáfila-Robles, R. *Renew. Sustain. Energy Rev.* **2012**, *16* (4), 2154.

(8) Chen, H.; Cong, T. N.; Yang, W.; Tan, C.; Li, Y.; Ding, Y. *Prog. Nat. Sci.* **2009**, *19* (3), 291.

(9) Styring, S. *Faraday Discuss.* **2012**, *155*, 357.

(10) Maeda, K.; Domen, K. *J. Phys. Chem. Lett.* **2010**, *1* (18), 2655.

(11) Concepcion, J. J.; House, R. L.; Papanikolas, J. M.; Meyer, T. J. *Proc. Natl. Acad. Sci.* **2012**, *109* (39), 15560.

(12) Ausfelder, F.; Beilmann, C.; Bertau, M.; Bräuninger, S.; Heinzel, A.; Hoer, R.; Koch, W.; Mahlendorf, F.; Metzelthin, A.; Peuckert, M.; Plass, L.; Räuchle, K.; Reuter, M.; Schaub, G.; Schiebahn, S.; Schwab, E.; Schüth, F.; Stolten, D.; Teßmer, G.; Wagemann, K.; Ziegahn, K.-F. *Chemie Ing. Tech.* **2015**, *87* (1-2), 17.

(13) Steinfeld, A. *Int. J. Hydrogen Energy* **2002**, *27* (6), 611.

(14) Ogden, J.; Williams, R. *Int. J. Hydrogen Energy* **1990**, *15* (3), 155.

(15) Grätzel, M. *Nature* **2001**, *414* (6861), 338.

(16) Ismail, A. A.; Bahnemann, D. W. *Sol. Energy Mater. Sol. Cells* **2014**, *128* (August), 85.

(17) van de Krol, R.; Liang, Y.; Schoonman, J. *J. Mater. Chem.* **2008**, *18* (20), 2311.

(18) Sivula, K.; Le Formal, F.; Grätzel, M. *ChemSusChem* **2011**, *4* (4), 432.

(19) Zallen, R.; Moret, M. P. *Solid State Commun.* **2006**, *137* (3), 154.

(20) Scanlon, D. O.; Dunnill, C. W.; Buckeridge, J.; Shevlin, S. A; Logsdail, A. J.; Woodley, S. M.; Catlow, C. R. A; Powell, M. J.; Palgrave, R. G.; Parkin, I. P.; Watson, G. W.; Keal, T. W.; Sherwood, P.; Walsh, A.; Sokol, A. A. *Nat. Mater.* **2013**, *12* (9), 798.

(21) Tang, H.; Prasad, K.; Sanjinès, R.; Schmid, P. E.; Lévy, F. *J. Appl. Phys.* **1994**, *75* (4), 2042.

(22) Leng, W. H.; Barnes, P. R. F.; Juozapavicius, M.; O'Regan, B. C.; Durrant, J. R. *J. Phys.*

Chem. Lett. **2010**, *1* (6), 967.
(23) Augustynski, J.; Solarska, R. *Catal. Sci. Technol.* **2013**, *3* (7), 1810.
(24) Zhang, P.; Gao, L.; Song, X.; Sun, J. *Adv. Mater.* **2015**, *27* (3), 562.
(25) Osterloh, F. E. *Chem. Soc. Rev.* **2013**, *42* (6), 2294.
(26) Feckl, J. M.; Dunn, H. K.; Zehetmaier, P. M.; Müller, A.; Pendlebury, S. R.; Zeller, P.; Fominykh, K.; Kondofersky, I.; Döblinger, M.; Durrant, J. R.; Scheu, C.; Peter, L.; Fattakhova-Rohlfing, D.; Bein, T. *Adv. Mater. Interfaces* **2015**, n/a.
(27) Dunn, H. K.; Feckl, J. M.; Müller, A.; Fattakhova-Rohlfing, D.; Morehead, S. G.; Roos, J.; Peter, L. M. P.; Scheu, C.; Bein, T. *Phys. Chem. Chem. Phys.* **2014**, *16* (44), 24610.
(28) Kondofersky, I.; Dunn, H. K.; Müller, A.; Mandlmeier, B.; Feckl, J. M.; Fattakhova-Rohlfing, D.; Scheu, C.; Peter, L. M.; Bein, T. *ACS Appl. Mater. Interfaces* **2015**, *7*, 4623.

2. Photoelectrochemical Water Splitting

One of the biggest advantages of photoelectrochemical water splitting over other sustainable methods for the generation of hydrogen is the easy separation of the products hydrogen and oxygen, as their evolutions take place at different photoelectrodes. Both photoanodes and photocathodes were investigated in this thesis and a brief introduction into the different water splitting processes and the materials investigated in this thesis follows.

2.1. Photoelectrodes

The photoelectrode, regardless of whether water is to be oxidized or reduced at it, has to be a semiconductor with valence and conduction band straddling the redox energy levels of hydrogen and oxygen.[1–3] Three different processes take place at it: the absorption of light, the separation of the electron-hole pair in the space-charge layer and the charge transfer to the electrolyte at the semiconductor-liquid interface (Figure 2-1).

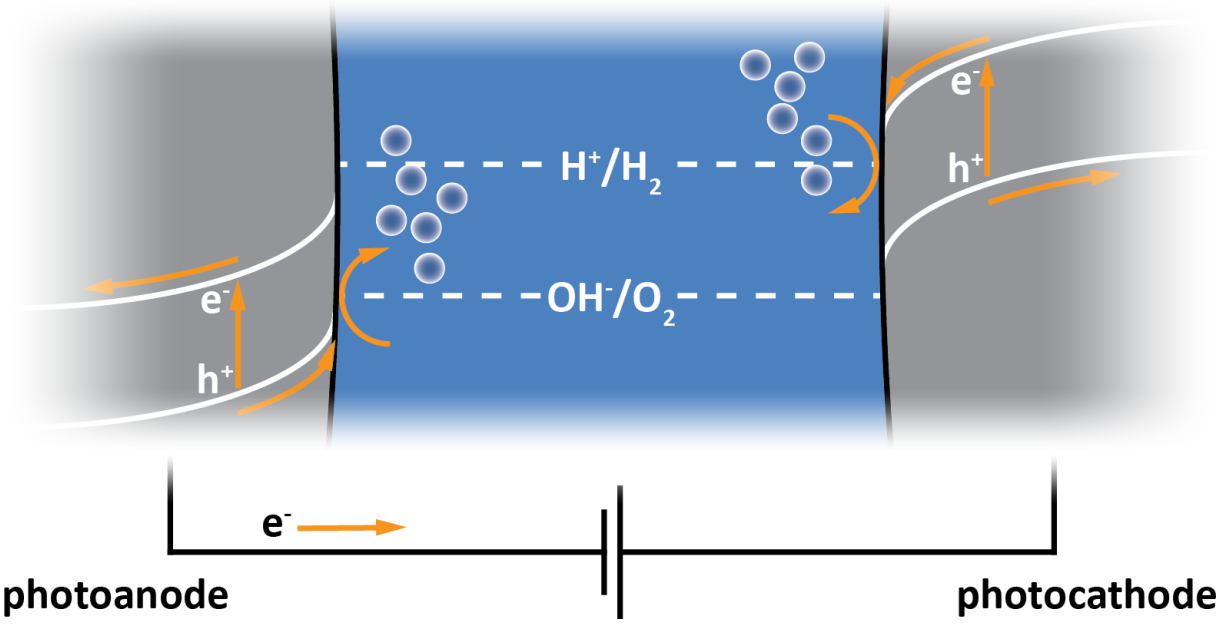

Figure 2-1: Water splitting processes taking place at photoanode and photocathode.

Light is absorbed if its energy is larger than the band gap of the semiconductor and an electron is excited into the conduction band, leaving a hole in the valence band. As smaller band gaps lead to the absorption of larger parts of the visible solar spectrum, the band gap of a material is a major selection criterion. An upper limit is imposed by the rapid intensity drop-off of the solar spectrum at ~ 400 nm, which corresponds to a band gap of 3.1 eV (ultraviolet regime).

Several approaches to calculate a material's performance limits in dependence of the band gap have been published so far.[4–6] These considerations assume that all photons of energies above the band gap are absorbed. However, light absorption of a specific sample also depends on the absorption coefficient. The light harvesting efficiency η_{lh} reflects this and is defined as the percentage of light absorbed by a sample in dependence of the wavelength.[7] Experimentally, it can be calculated from UV-vis spectra.

The generated electron-hole pair has to be separated by a potential gradient, otherwise it recombines.[8,9] This potential gradient is a direct consequence of the photoelectrode being immersed in an aqueous electrolyte and the resulting semiconductor-liquid junction. Electronic equilibrium between semiconductor and electrolyte is reached by current flow across the junction until the Fermi-level of the electrons in the solid is equal to the redox-potential of the electrolyte. In the electrolyte, a double layer of a compact Helmholtz layer followed by a diffuse Gouy-Chapman layer, results.[10,11] The behavior of the photoelectrode depends on whether it is made out of an n- or p-type semiconductor and either electrons or holes, respectively, accumulate at the surface.[1] The resulting band bending at the so-called space-charge layer allows separating electrons and holes. The majority carriers travel through the circuit to the other electrode, and measuring this photocurrent provides one of the simplest performance-describing metrics. In addition, the so-called charge separation efficiency η_{sep}, which quantifies the efficiency of electron-hole separation in the bulk and in the space-charge region, can be used to describe this step.[12,13]

The minority carriers, on the other hand, are injected from the electrode surface into the electrolyte. In the case of a photocathode made out of a p-type semiconductor, the minority carriers are electrons, the electrolyte is reduced and hydrogen is evolved ("hydrogen evolution reaction").[1]

$$4\ H_2O + 4\ e^- \longrightarrow 4\ OH^- + 2\ H_2 \qquad \text{(basic solution)}$$
$$4\ H^+ + 4\ e^- \longrightarrow 2\ H_2 \qquad \text{(acidic solution)}$$

The minority carriers in an n-type semiconductor are holes and oxidation of the electrolyte at the photoanode leads to the evolution of oxygen ("oxygen evolution reaction"). [1]

$$4\ OH^- + 4\ h^+ \longrightarrow 2\ H_2O + O_2 \qquad \text{(basic solution)}$$
$$H_2O + 4\ h^+ \longrightarrow 4\ H^+ + O_2 \qquad \text{(acidic solution)}$$

As four holes are required to produce one O_2 molecule, the recombination rate tends to be high and efficient water oxidation is much more difficult to achieve than efficient water reduction. As with the other two steps, an efficiency, the transfer efficiency $\eta_{transfer}$, can be defined and experimentally determined from photocurrent transient measurements.[13,14]

The two reactions impose a lower limit on the band gap of the semiconductor. In addition to a redox potential of 1.23 eV, thermodynamic losses of ~ 0.4 eV and overpotentials of ~ 0.3 to 0.4 eV have to be considered and a minimum band gap of 1.9 eV, corresponding to an absorption onset of ~ 650 nm, results.[4–6] For unbiased operation, the conduction band should also lie higher than the potential of the H^+/H_2 redox couple and the valence band should lie lower than the potential of the OH^-/O_2 redox couple.

There are several ways of quantifying the performance and so far, photocurrent measurements and the individual efficiencies η_{lh}, η_{sep} and $\eta_{transfer}$ have been discussed. The overall efficiency of a photoelectrode, called the incident photon-to-current efficiency (IPCE), can be determined by multiplying the three individual efficiencies η_{lh}, η_{sep} and $\eta_{transfer}$.[13] It can also be measured by comparing the photon influx to the photocurrent. In combination with η_{lh} and $\eta_{transfer}$ knowing the IPCE allows calculating η_{sep}, which cannot be directly measured.

2.2. Photoelectrode Materials

In addition to the band gap requirements discussed above, a material should also meet several other conditions. The light absorption coefficient should be high, minority and majority carrier conductivities should be high and surface kinetics fast. To be a potential contender for large-scale applications, a material should also be cheap, non-toxic, and stable in aqueous solutions. Several promising materials have so far been identified and most studies focus on improving the properties of these select few materials, which include the photoanode materials $BiVO_4$, α-Fe_2O_3, WO_3 and TiO_2 and the photocathode materials p-Si, Cu_2O and $CuFeO_2$.[2] In this thesis, photoelectrodes out of TiO_2, α-Fe_2O_3, WO_3 and FeCrAl-oxide were analyzed and are introduced below.

No material investigated so far fulfills all of the requirements and several approaches have been developed to enhance its suitability.[1] Doping, for example, can decrease the band gap, leading to increased absorption. It can also enhance charge carrier mobility. The overpotential can be reduced by surface modification with co-catalysts such as Co_3O_4 or Co-Pi.[15] Materials with a low light absorption coefficient benefit from the creation of thicker layers, although this approach is limited to the point at which bulk recombination dominates. Bulk recombination can, in turn be reduced by introducing a porous structure and increasing the surface area.[16,17]

2.2.1. Titanium Dioxide

In addition to several instable or metastable modifications, titanium dioxide mainly crystallizes in one of the three modifications rutile, anatase and brookite.[18–20] Rutile is thermodynamically stable at room temperatures, whereas anatase and brookite are metastable and transform into rutile at temperatures above approximately 1090 °C and 930 °C, respectively.[21] Both modifications can, however, be stabilized by nanostructuring. For example, the large role of

the surface energy leads to the anatase modification being preferred for very small nanoparticles.[22]

The rutile structure can be derived from a slightly disordered hexagonal closed packing of oxygen in which half of the octahedral interstitials are filled with titanium (Figure 2-2a and b).[20] The octahedrons share two vertices such that they form chains along one axis, with edge-sharing leading to a three-dimensional structure. The resulting unit cell is body-centered tetragonal with the space group $I4_2/mnm$ and the lattice parameters a=b=4.594 Å and c=2.958 Å

The other two modifications, anatase and brookite (Figure 2-2c and d), can also be derived from a cubic-closed oxygen package with half of the octahedral interstitials being filled with titanium.[19,20] Contrary to rutile, these TiO_6-octahedrons are connected by three vertices in brookite and four in anatase. Anatase has a unit cell with the space group $I4_1/amd$ and the lattice parameters a=b=3.784 Å and c=9.514 Å, brookite one with the space group Pbca and the lattice parameters a=9.1842 Å, b=5.447 Å and c= 5.145 Å.

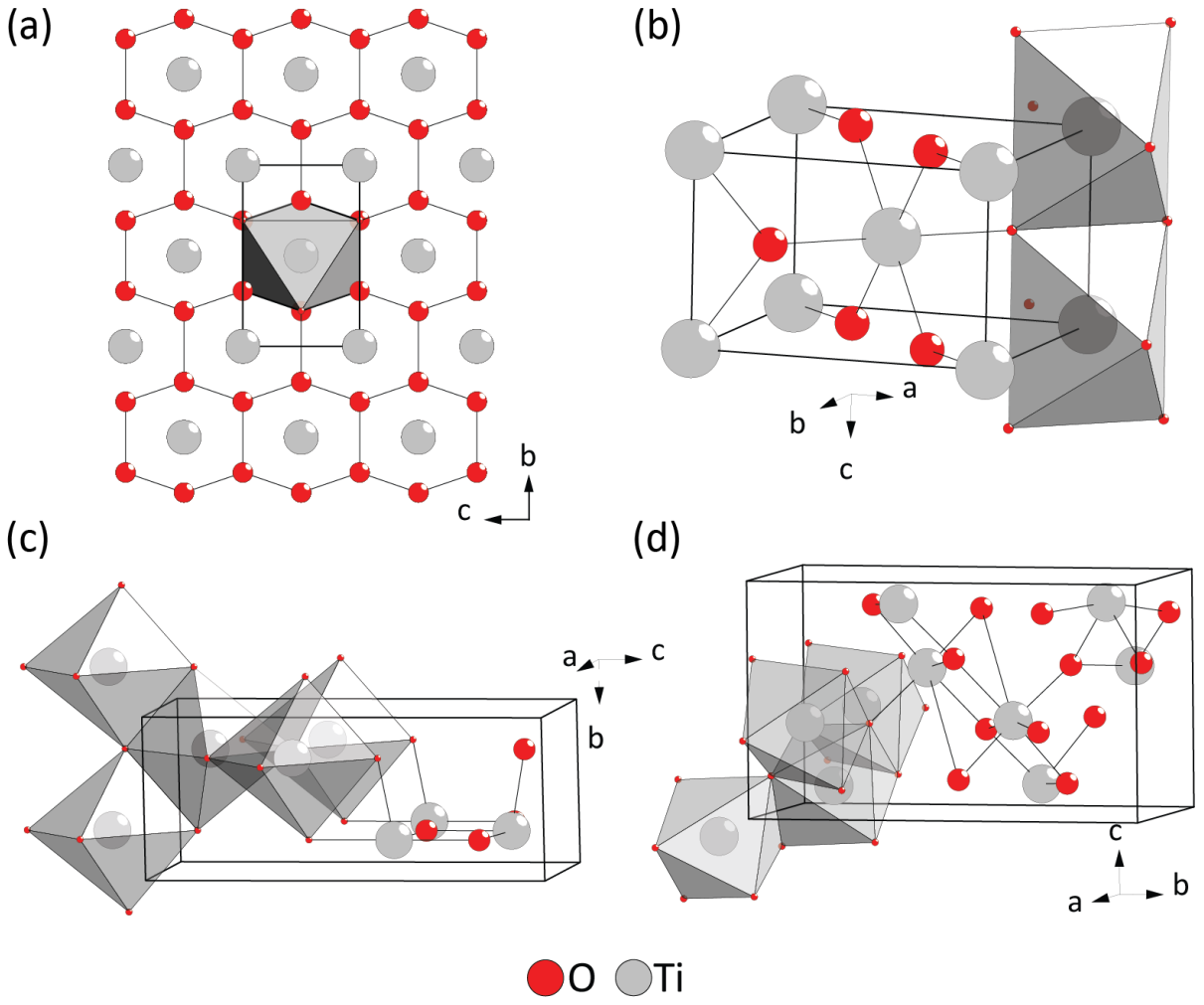

Figure 2-2: TiO_2 crystallizes in three relevant modifications, rutile (a and b), anatase (c) and brookite (d). Ti is represented by grey spheres, O by red spheres.

Titania is an n-type semiconductor and can be used as a photocatalyst or, for photoelectrochemical water splitting, as a photoanode material.[23,24] All three modifications discussed so far have fairly large band gaps, with 3.1 eV for rutile, 3.3 eV for anatase and 1.9 eV for brookite.[25,26] All but brookite therefore absorb in the UV region. However, most works focus on anatase and rutile. Due to the large band gaps, the maximum solar-to-oxygen efficiency is limited to 1.3 % for anatase and 2.2 % for rutile,[6] and working around these intrinsic limits by extending the absorption spectrum is the most promising strategy. This can be achieved by two very different approaches. The first, doping, changes the electronic structure and therefore the band gap. 3d, 4s and 4p orbitals of Ti dominated the conduction band of TiO_2, and its position can be changed by doping with cations.[24] Anion doping, in contrast, typically changes the position of the valence band.[24] Both approaches have been successful and several studies have investigated the influence of dopants on the band structure and the light absorption range.[27–29]

While doping changes a materials' intrinsic properties, the absorption spectrum can also be extended by depositing a photosensitizer that absorbs a different spectral range than TiO_2 and can inject charge carriers into TiO_2. This approach is very popular for dye-sensitized solar cells, where (metal)organic dyes are applied.[30,31] Unfortunately, these dyes are often unstable under the harsh conditions present during water splitting,[30] and a second group of photoesensitizers are noble metal nanoparticles. Light induces localized surface plasmons at the surface of these nanoparticles.[32–35] As the wavelength of the absorbed light strongly depend on the size, shape, material and environment of the nanoparticle, the system can be tuned to absorb visible or even near-infrared light.[32,33,35,36]

However, the large band gap is the material's biggest drawback while charge separation and transport tend to be excellent.[37,38] Another big advantage is that TiO_2 has been heavily investigated for other fields such as dye-sensitized solar cells,[30,31] electrodes,[39] sensor applications,[40] and biomedical applications,[41] and that a lot of prior knowledge is readily available. This advantage also extends to the fabrication of nanostructures, and synthesis protocols for several morphologies such as nanowires, nanotubes, inverse opals, flat layers, porous fibers and porous spheres have already been published.[42–44]

2.2.2. Iron(III) Oxide

While iron can, under extreme conditions, have oxidation numbers between –II and +VI, it is most common with the oxidation numbers +II and +III and forms three different oxides: FeO with Fe^{2+}, Fe_3O_4 with Fe^{2+} and Fe^{3+}, and Fe_2O_3 with Fe^{3+}.[45] Of these, Fe_2O_3 can form four different modifications (α-/β-/γ-/ε-Fe_2O_3), of which only α-Fe_2O_3, also known as hematite, is stable at room temperature. Hematite crystallizes in the corundum structure with the space group $R\bar{3}c$ and has the lattice parameters a=b=5.035 Å and c=13.747 Å.[46] Oxygen is hexagonal closed-packed and iron fills two thirds of the octahedral interstices so that two interstices are filled followed by a vacancy (Figure 2-3).

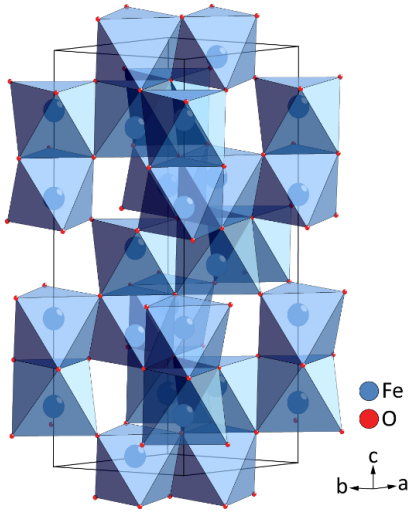

Figure 2-3: Unit cell of hematite. Fe is represented by blue spheres, O by red spheres.

As an n-type semiconductor, hematite can evolve oxygen and fulfills several of the photoelectrode requirements listed above.[47] It is cheap, non-toxic and corrosion resistant.[47,48] Due to a band gap between 1.9 and 2.2 eV, it absorbs a large fraction of visible light and has a potential solar-to-oxygen efficiency of up to 16.8 %.[6,47] However, light absorption in hematite is not very strong, necessitating thick layer in which bulk recombination becomes a major loss mechanism.[13,47] Therefore, photoanodes are often nanostructured to have a very high surface.[47] Further, the flat band potential is too low for water reduction and a bias has to be applied by, for example, a photocathode in tandem. Poor major carrier conductivity can be enhanced by doping or by host-guest approaches with a conducting scaffold.[49–55]

2.2.3. Tungsten Trioxide

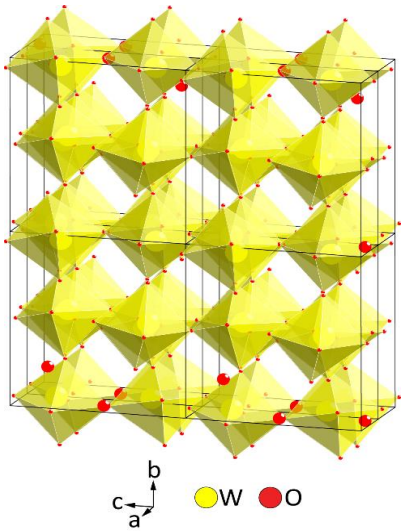

Figure 2-4: Unit cell of monoclinic WO_3. W is represented by yellow, O by red spheres.

In dependence of the temperature, WO_3 crystallizes in five different modifications, with γ-WO_3 being stable at room temperature.[57] Its crystal structure can be derived from the ReO_3–structure, in which ReO_6-octahedra share corners to form a three-dimensional network.[58] However, while ReO_3 is cubic, γ-WO_3 is distorted and a monoclinic structure with the space group $P2_1/n$ and the lattice parameters a=7.30 Å, b=7.53 Å, c=7.68 Å and β=90.54° results (Figure 2-4).[59]

WO_3 has been evaluated for several applications, among them for electrochromic windows,[60] as an electrode materials for solid oxide fuel cells,[61] and as a gas sensor.[62,63] It is also well-suited as a photoanode material. WO_3 is an n-type semiconductor and, with an indirect band gap between 2.5 and 2.8 eV, absorbs light until the blue region of the spectrum.[48,60,64] This band gap limits the overall solar-to-oxygen efficiency to 8 % and, like with titania, band gap engineering is a popular approach to increasing its maximum performance.[6,65–68] However, it has excellent charge transport properties and fast surface kinetics.[64] Several studies have focused on increasing the performance by controlling the morphology, and mesoporous structures, nanowires, thin films, nanorods and nanoplates have been investigated for photoelectrochemical water splitting.[57,69]

2.2.4. FeCrAl Oxide

Fe_2O_3, Cr_2O_3 and Al_2O_3 all crystallize in the corundum structure (Figure 2-3).[70] Steinwehr *et al.* were able to show that FeCrAl oxides form solid solutions in the same structure as the end members with a miscibility gap only at high Al-contents.[70] The band gaps of several compositions were investigated by theoretical studies and found to lie lower than those of the end members, indicating potential as a photocathode material.[71] However, only two publications have so far experimentally investigated the system for this purpose. A combinatorial study identified the highest hydrogen evolution rate at a stoichiometry of $Fe_{0.84}Cr_{1.0}Al_{0.16}O_3$.[72] Even though photocurrents were extremely low, an open circuit photovoltage of 0.95 V and a band gap of 1.8 eV were promising. A follow-up study, also combinatorial in nature, was able to show improved photocurrents by depositing thicker films via reactive magnetron co-sputtering.[73] The combination of small band gap, low photovoltage and demonstration of performance-enhancement by structuring warrants further studies, with a first attempt discussed in Chapter 6.

2.3. References

(1) Grätzel, M. *Nature* **2001**, *414* (6861), 338.
(2) van de Krol, R.; Liang, Y.; Schoonman, J. *J. Mater. Chem.* **2008**, *18* (20), 2311.
(3) Li, Z.; Luo, W.; Zhang, M.; Feng, J.; Zou, Z. *Energy Environ. Sci.* **2013**, *6* (2), 347.
(4) Weber, M. F.; Dignam, M. J. *Int. J. Hydrogen Energy* **1986**, *11* (4), 225.
(5) Bolton, J. R.; Strickler, S. J.; Connolly, J. S. *Nature* **1985**, *316* (6028), 495.
(6) Murphy, A. B.; Barnes, P. R. F.; Randeniya, L. K.; Plumb, I. C.; Grey, I. E.; Horne, M. D.; Glasscock, J. A. *Int. J. Hydrogen Energy* **2006**, *31* (14), 1999.
(7) Tachibana, Y.; Hara, K.; Sayama, K.; Arakawa, H. *Chem. Mater.* **2002**, *14* (6), 2527.
(8) Lindquist, S.-E.; Finnström, B.; Tegnér, L. *J. Electrochem. Soc.* **1983**, *130* (2), 351.
(9) Lewis, N. S. *J. Electrochem. Soc.* **1984**, *131* (11), 2496.
(10) Brüesch, P. *J. Appl. Phys.* **2004**, *95* (5), 2846.
(11) Guidelli, R.; Schmickler, W. *Electrochim. Acta* **2000**, *45* (15-16), 2317.
(12) Gärtner, W. W. *Phys. Rev.* **1959**, *116* (1), 84.
(13) Dunn, H. K.; Feckl, J. M.; Müller, A.; Fattakhova-Rohlfing, D.; Morehead, S. G.; Roos, J.; Peter, L. M. P.; Scheu, C.; Bein, T. *Phys. Chem. Chem. Phys.* **2014**, *16* (44), 24610.
(14) Peter, L. M.; Wijayantha, K. G. U.; Tahir, A. A. *Faraday Discuss.* **2012**, *155* (0), 309.
(15) Yang, J.; Wang, D.; Han, H.; Li, C. *Acc. Chem. Res.* **2013**, *46* (8), 1900.
(16) Augustynski, J.; Solarska, R. *Catal. Sci. Technol.* **2013**, *3* (7), 1810.
(17) Zhang, P.; Gao, L.; Song, X.; Sun, J. *Adv. Mater.* **2015**, *27* (3), 562.
(18) Liu, Q.-J.; Zhang, N.-C.; Liu, F.-S.; Liu, Z.-T. *Phys. Scr.* **2014**, *89* (7), 075703.
(19) Baur, W. H. *Acta Crystallogr.* **1961**, *14* (3), 214.
(20) Cromer, D. T.; Cromer, D. T.; Herrington, K.; Herrington, K. *J. Am. Chem. Soc.* **1955**, *77* (18), 4708.
(21) Mitsuhashi, T.; Kleppa, O. J. *J. Am. Ceram. Soc.* **1979**, *62* (7), 356.

(22) Bahnemann, D. W.; Hilgendorff, M.; Memming, R. *J. Phys. Chem. B* **1997**, *101* (21), 4265.
(23) Ni, M.; Leung, M. K. H.; Leung, D. Y. C.; Sumathy, K. *Renew. Sustain. Energy Rev.* **2007**, *11* (3), 401.
(24) Ma, Y.; Wang, X.; Jia, Y.; Chen, X.; Han, H.; Li, C. *Chem. Rev.* **2014**, No. 114, 9987.
(25) Zallen, R.; Moret, M. P. *Solid State Commun.* **2006**, *137* (3), 154.
(26) Scanlon, D. O.; Dunnill, C. W.; Buckeridge, J.; Shevlin, S. A; Logsdail, A. J.; Woodley, S. M.; Catlow, C. R. A; Powell, M. J.; Palgrave, R. G.; Parkin, I. P.; Watson, G. W.; Keal, T. W.; Sherwood, P.; Walsh, A.; Sokol, A. A. *Nat. Mater.* **2013**, *12* (9), 798.
(27) Borgarello, E.; Kiwi, J.; Graetzel, M.; Pelizzetti, E.; Visca, M. *J. Am. Chem. Soc.* **1982**, *104* (11), 2996.
(28) Choi, W.; Termin, A.; Hoffmann, M. R. *J. Phys. Chem.* **1994**, *98* (51), 13669.
(29) Xu, A.-W.; Gao, Y.; Liu, H.-Q. *J. Catal.* **2002**, *207* (2), 151.
(30) Youngblood, W. J.; Lee, S. A.; Maeda, K.; Mallouk, T. E. *Acc. Chem. Res.* **2009**, *42* (12), 1966.
(31) Yum, J.-H.; Chen, P.; Grätzel, M.; Nazeeruddin, M. K. *ChemSusChem* **2008**, *1* (8-9), 699.
(32) Linic, S.; Christopher, P.; Ingram, D. B. *Nat. Mater.* **2011**, *10* (12), 911.
(33) Wang, C.; Astruc, D. *Chem. Soc. Rev.* **2014**, *43*, 7188.
(34) Warren, S. C.; Thimsen, E. *Energy Environ. Sci.* **2012**, *5* (1), 5133.
(35) Petryayeva, E.; Krull, U. J. *Anal. Chim. Acta* **2011**, *706* (1), 8.
(36) Noguez, C. *J. Phys. Chem. C* **2007**, *111* (10), 3806.
(37) Leng, W. H.; Barnes, P. R. F.; Juozapavicius, M.; O'Regan, B. C.; Durrant, J. R. *J. Phys. Chem. Lett.* **2010**, *1* (6), 967.
(38) Tang, H.; Prasad, K.; Sanjinès, R.; Schmid, P. E.; Lévy, F. *J. Appl. Phys.* **1994**, *75* (4), 2042.
(39) Zhang, Q.; Cao, G. *Nano Today* **2011**, *6* (1), 91.
(40) Bai, J.; Zhou, B. *Chem. Rev.* **2014**, *114* (19), 10131.
(41) Rajh, T.; Dimitrijevic, N. M.; Bissonnette, M.; Koritarov, T.; Konda, V. *Chem. Rev.* **2014**, *114* (19), 10177.
(42) Fattakhova-Rohlfing, D.; Zaleska, A.; Bein, T. *Chem. Rev.* **2014**, *114* (19), 9487.
(43) Lee, K.; Mazare, A.; Schmuki, P. *Chem. Rev.* **2014**, *114* (19), 9385.
(44) Wang, X.; Li, Z.; Shi, J.; Yu, Y. *Chem. Rev.* **2014**, *114* (19), 9346.
(45) Hollemann, A.; Wiberg, N.; Wiberg, E. *Lehrbuch der Anorganischen Chemie*, 102nd ed.; de Gruyter, 2007.
(46) Maslen, E. N.; Streltsov, V. a.; Streltsova, N. R.; Ishizawa, N. *Acta Crystallogr. Sect. B* **1994**, *50* (1903), 435.
(47) Sivula, K.; Le Formal, F.; Grätzel, M. *ChemSusChem* **2011**, *4* (4), 432.
(48) Hodes, G.; Cahen, D.; Manassen, J. *Nature* **1976**, *260* (5549), 312.
(49) Bohn, C. D.; Agrawal, A. K.; Walter, E. C.; Vaudin, M. D.; Herzing, A. A; Haney, P. M.; Talin, A. A.; Szalai, V. A. *J. Phys. Chem. C* **2012**, *116* (29), 15290.
(50) Kondofersky, I.; Dunn, H. K.; Müller, A.; Mandlmeier, B.; Feckl, J. M.; Fattakhova-Rohlfing, D.; Scheu, C.; Peter, L. M.; Bein, T. *ACS Appl. Mater. Interfaces* **2015**, *7*, 4623.
(51) Sivula, K.; Formal, F. Le; Grätzel, M. *Chem. Mater.* **2009**, *21* (13), 2862.
(52) Aroutiounian, V. M.; Arakelyan, V. M.; Shahnazaryan, G. E.; Hovhannisyan, H. R.; Wang,

H.; Turner, J. A. *Sol. Energy* **2007**, *81* (11), 1369.
(53) Deng, J.; Zhong, J.; Pu, A.; Zhang, D.; Li, M.; Sun, X.; Lee, S.-T. *J. Appl. Phys.* **2012**, *112* (8), 084312.
(54) Lian, X.; Yang, X.; Liu, S.; Xu, Y.; Jiang, C.; Chen, J.; Wang, R. *Appl. Surf. Sci.* **2012**, *258* (7), 2307.
(55) Kronawitter, C. X.; Zegkinoglou, I.; Shen, S.-H.; Liao, P.; Cho, I. S.; Zandi, O.; Liu, Y.-S.; Lashgari, K.; Westin, G.; Guo, J.-H.; Himpsel, F. J.; Carter, E. a.; Zheng, X. L.; Hamann, T. W.; Koel, B. E.; Mao, S. S.; Vayssieres, L. *Energy Environ. Sci.* **2014**, *7* (10), 3100.
(56) Feckl, J. M.; Dunn, H. K.; Zehetmaier, P. M.; Müller, A.; Pendlebury, S. R.; Zeller, P.; Fominykh, K.; Kondofersky, I.; Döblinger, M.; Durrant, J. R.; Scheu, C.; Peter, L.; Fattakhova-Rohlfing, D.; Bein, T. *Adv. Mater. Interfaces* **2015**, 10.1002/admi.201500358.
(57) Liu, X.; Wang, F.; Wang, Q. *Phys. Chem. Chem. Phys.* **2012**, *14* (22), 7894.
(58) Meisel, K. *Zeitschrift für Anorg. und Allg. Chemie* **1932**, *207* (12), 121.
(59) Tanisaki, S. *J. Phys. Soc. Japan* **1960**, *15* (4), 573.
(60) Granqvist, C. G. *Sol. Energy Mater. Sol. Cells* **2000**, *60* (3), 201.
(61) Hobbs, B. S.; Tseung, a. C. C. *Nature* **1969**, *221* (5042), 452.
(62) Kukkola, J.; Mäklin, J.; Halonen, N.; Kyllönen, T.; Tóth, G.; Szabó, M.; Shchukarev, A.; Mikkola, J.-P.; Jantunen, H.; Kordás, K. *Sensors Actuators B Chem.* **2011**, *153* (2), 293.
(63) Williams, D. E.; Aliwell, S. R.; Pratt, K. F. E.; Caruana, D. J.; Jones, R. L.; Cox, R. A.; Hansford, G. M.; Halsall, J. *Meas. Sci. Technol.* **2002**, *13* (6), 923.
(64) Santato, C.; Ulmann, M.; Augustyński, J. *J. Phys. Chem. B* **2001**, *105* (5), 936.
(65) Nah, Y.-C.; Paramasivam, I.; Hahn, R.; Shrestha, N. K.; Schmuki, P. *Nanotechnology* **2010**, *21* (10), 105704.
(66) Sun, Y.; Murphy, C. J.; Reyes-Gil, K. R.; Reyes-Garcia, E. A.; Thornton, J. M.; Morris, N. A.; Raftery, D. *Int. J. Hydrogen Energy* **2009**, *34* (20), 8476.
(67) Yang, B.; Luca, V. *Chem. Commun.* **2008**, No. 37, 4454.
(68) Cole, B.; Marsen, B.; Miller, E.; Yan, Y.; To, B.; Jones, K.; Al-Jassim, M. *J. Phys. Chem.* **2008**, *112*, 5213.
(69) Bignozzi, C. A.; Caramori, S.; Cristino, V.; Argazzi, R.; Meda, L.; Tacca, A. *Chem. Soc. Rev. Chem. Soc. Rev* **2013**, *42* (42), 2228.
(70) Steinwehr, H. E. v. *Zeitschrift für Krist.* **1967**, *125*, 377.
(71) Praveen, C. S.; Timon, V.; Valant, M. *Comput. Mater. Sci.* **2012**, *55*, 192.
(72) Rowley, J. G.; Do, T. D.; Cleary, D. A; Parkinson, B. A. *ACS Appl. Mater. Interfaces* **2014**, *6* (12), 9046.
(73) Sliozberg, K.; Stein, H. S.; Khare, C.; Parkinson, B. A.; Ludwig, A.; Schuhmann, W. *ACS Appl. Mater. Interfaces* **2015**, *7*, 4883.

3. Transmission Electron Microscopy

Since the 17th century, microscopy has allowed the analysis of features unresolvable by the naked eye and greatly furthered mankind's understanding of the world around us. The maximum resolution of a microscope, as described by Abbe, is limited by the wavelength of the light source and conventional optical microscopes using visible light can only resolve features of approximately 300 nm.[1] Following these consideration, Ernst Ruska in the 1930s developed ways of substituting visible light with an electron beam, whose wavelength depends on the acceleration voltage.[2] With high acceleration voltages, the resolution can therefore be greatly enhanced to the Ångstrom or, if aberrations are corrected, even the sub-Ångstrom scale. [1] His work led to the development of two different, co-existing methods, scanning electron microscopy (SEM) and transmission electron microscopy (TEM). The first, SEM, often images the surface morphology of samples by scanning a converged electron beam over the sample and measuring the intensity of secondary or backscattered electrons. The second, TEM, requires an electron-transparent sample and, in analogy to classical optical microscopes, uses transmitted electrons to create an image. As the samples discussed in this thesis were mostly investigated by in-depth TEM studies, the method is introduced in more detail below.

3.1. The Transmission Electron Microscope

A simplified build of electron source, condenser lens system, sample, objective lens system, projector lens system and detector already allows understanding most modes a TEM is capable of. There are two different kinds of electron sources, thermionic emitters and field-emission guns (FEG). Thermionic emitters are fine tungsten or LaB_6 tips which are heated, causing them to emit electrons, and to which a bias voltage is applied to bundle the beam. Field-emission guns, on the other hand, work by applying a strong electric field and electrons tunnel out of a tungsten tip. Compared to thermionic emitters, they are brighter, have a longer life-time and a smaller energy spread. However, they require a better vacuum and therefore lead to higher costs. In most modern TEMs, a Schottky emitter is used, where electrons leave the tip via thermally assisted field emission. The condenser lens system controls the convergence of the electron beam at the sample and the intensity of the beam. It consists of at least two electromagnetic lenses and an aperture. The sample needs to be electron-transparent, which imposes a maximum thickness dependent on the density. It also has to be stable in vacuum, imposing restrictions on, for example, biological samples, and not deteriorate under electron irradiation. The objective lens system is once again composed of electromagnetic lenses and an aperture. It is used to create a first image and a diffraction pattern in the backfocal plane. The intermediate lens allows choosing between imaging and

diffraction. The contrast in conventional bright field (BF) images can be enhanced by inserting an objective lens aperture which removes scattered electrons. The objective lens system and the different available modes are discussed in more detail in the following section. The projector lens system creates the final image or diffraction pattern, which is then detected by either a ZnS viewing screen, which fluoresces when hit by electrons, or a charge-coupled device (CCD) camera.

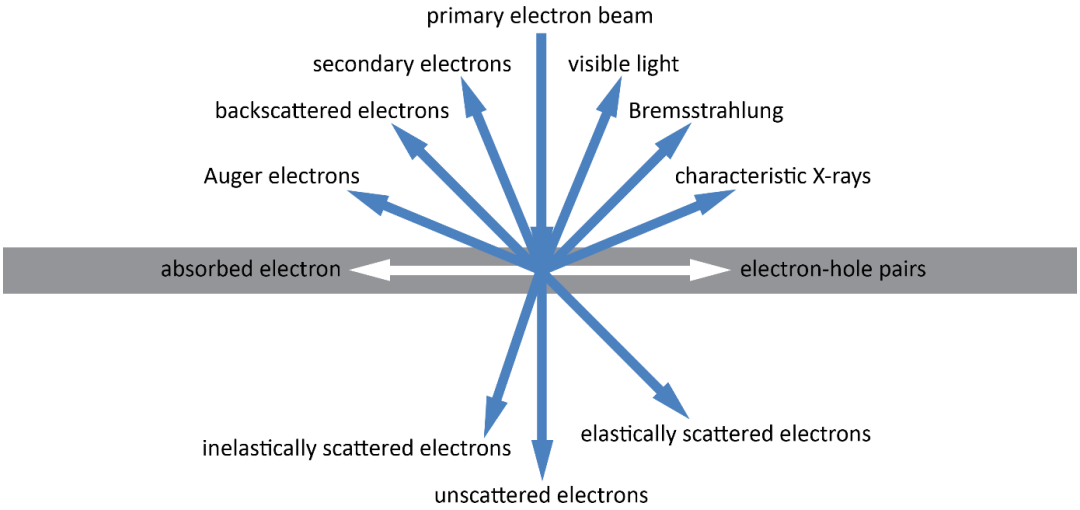

Figure 3-1: An incident electron beam interacts with the sample by several different scattering processes, which leads to several secondary signals such as characteristic X-rays, secondary electrons, Auger electrons and so on.

The primary electron beam interacts with the sample by several elastic and inelastic processes (Figure 3-1), leading to several imaging and spectroscopy methods.[1,3,4] However, visible light, backscattered electrons, secondary electrons, Auger electrons and electron-hole pairs are only rarely measured in the TEM and will not be discussed in greater detail. Much more relevant in this context are unscattered electrons, elastically scattered electrons and inelastically scattered electrons, which are used for several imaging methods as well as electron energy-loss spectroscopy (EELS). Bremsstrahlung and characteristic X-rays are measured to obtain energy-dispersive X-ray spectroscopy (EDX) spectra. Which electrons are used to create an image strongly depends on whether the electron beam is parallel or converged as it reaches the sample. In analogy to optical microscopy, imaging with a parallel beam is called “conventional TEM”, whereas a converged beam scanned over a sample surface is called “scanning TEM”. Both modes are described in more detail in the next two sections.

3.1.1. Conventional Transmission Electron Microscopy

In spite of the many different scattering processes taking place, most CTEM methods can be understood using simple ray tracing diagrams (Figure 3-2).[1,3] A parallel incident electron beam illuminates the sample and a part of it leaves the sample unscattered, while a part is scattered

at different scattering angles. For crystalline materials, the geometric aspect of the diffraction process can be described using the Bragg equation. The objective lens focuses all beams diffracted by parallel lattice planes, which leave the sample at the same angle, in the backfocal plane and creates an image in the first image plane. The intermediate lens follows and allows choosing either diffraction patterns or images. The magnification of the image or the camera length of the diffraction pattern can be chosen with the projector lens, which then creates an image or diffraction pattern on the detector.

These two very basic operations, imaging and diffraction, can be modified by inserting different apertures. In the backfocal plane of the objective lens, the objective aperture allows choosing whether to create an image with the primary beam or one of the diffracted beams. If the primary beam is chosen, the so-called "bright field" image with a strong mass and/or diffraction contrast is formed. Choosing a diffracted beam allows imaging only those parts of a sample with a specific crystallographic orientation and, by acquiring several such so-called "dark field" (DF) images, enables crystallographic orientation mapping. In addition to inserting apertures into the backfocal plane of the objective lens, apertures can also be inserted in the first image plane and the so-called "selected-area electron diffraction" (SAED) allows acquiring diffraction patterns of well-defined regions of the sample (Figure 3-2).

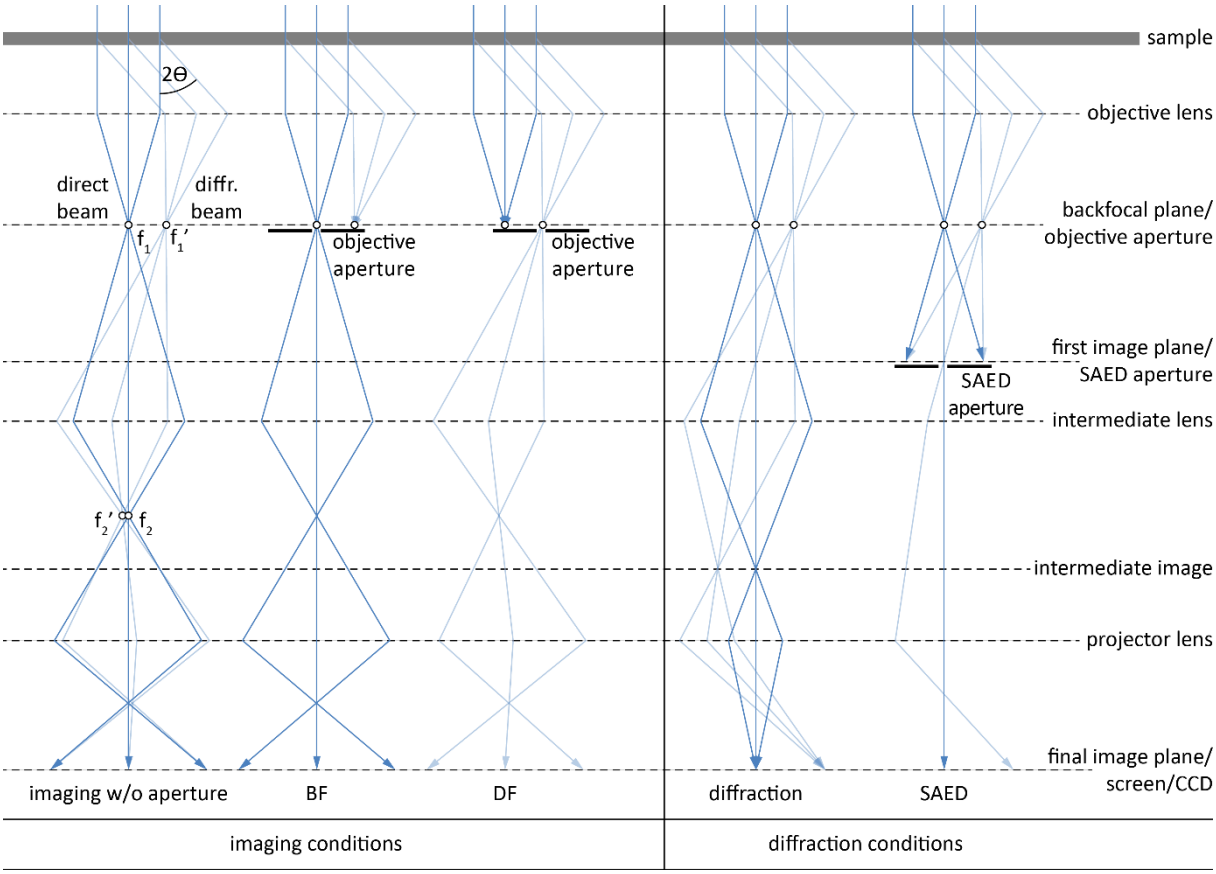

Figure 3-2: Ray tracing diagrams of the lens system in the TEM below the sample and assuming parallel illumination. By inserting apertures and/or changing the excitation of the intermediate lens, different imaging and diffraction modes can be realized. Please note that the so-called "off-axis" DF case is shown here.

For high resolution TEM (HRTEM), not only one but many diffracted beams are used to create an image and interference effects dominate.[1] The primary electron beam is scattered by the sample, with the scattered beams having different phases and amplitudes depending on their path through the sample. All these beams then interfere and a complex pattern results. The incident electron beam can be approximated as a plane wave which is then modified by its interaction with the sample. If the sample is thin, the so-called "weak phase approximation" applies and the exit wave is proportional to the crystal potential. The propagation of the exit wave can be described by the so-called contrast transfer function (CTF), which incorporates several factors such as defocus and aberrations. The detector only measures the intensity, which is equal to the square modulus of the wave function, and the phase of the wave function is lost. This loss of information prevents the straight-forward analysis of HRTEM images and simulations are required for the reconstruction of atomic positions. However, periodicity and symmetry carry over and lattice spacings, angles and symmetry groups can be determined from HRTEM images of periodic structures or their fourier transforms (FT), which transforms an image into the frequency domain and allows the simple analysis of symmetric patterns.

3.1.2. Scanning Transmission Electron Microscopy

As an alternative to the parallel illumination used in CTEM and HRTEM, the beam can also be converged and scanned over the sample. By detecting the scattered electrons, an image can then be constructed. This mode is called "scanning TEM" (STEM).[1,5,3] There are three different STEM detectors for different scattering angles, each corresponding to specific scattering processes. Electrons scattered inelastically or elastically at angles below 10 mrad are detected by the bright field detector (BF-STEM), coherent, elastically scattered electrons (Bragg scattering) are detected at angles between 10 and 50 mrad by an annular dark-field detector (ADF-STEM), and incoherent elastically scattered electrons (Rutherford scattering) at angles above 50 mrad by a high-angle annular dark-field detector (HAADF-STEM). The resolution of HAADF-STEM images is determined by the diameter of the incident beam and by the thickness of the sample. In many modern STEMs, a resolution of up to 1.2 Å can be obtained and probe-correctors even allow for resolutions of up to 0.8 Å. Correctors therefore allow for resolutions comparable to HRTEM. In contrast to HRTEM, where interference pattern are measured, the signal in STEM images, if the image is tilted into a zone axis, corresponds to atomic columns. The interpretation of images is therefore much more straight-forward.

Compared to BF-CTEM and BF-STEM images, where the non-scattered electrons are imaged, the contrast is reversed in ADF- and HAADF-STEM images and heavy elements and thick areas generate a high brightness. This effect is quite strong and HAADF-STEM images often show only mass contrast with a strong dependence on the atomic number Z with $I \approx Z^2$.

3.1.3. Spectroscopic Methods

Two spectroscopic methods, EDX and EELS, are very commonly used in in combination with TEM.

The mechanism by which characteristic X-rays measured in EDX spectroscopy are generated is shown in Figure 3-3.[1,3] An electron hits a core electron and, provided the incident beam has sufficient energy, knocks it out, leaving a vacancy. Such a vacancy in one of the inner shells is energetically unfavorable and is quickly occupied by an electron from a higher shell. This transition moves that electron to a position with a lower potential energy and the energy difference can be released in the form of X-rays. The energy of this X-ray is characteristic for specific elements and can be detected using a semiconductor pin diode. X-rays are also emitted in the form of Bremsstrahlung, which is caused by electrons being slowed down by the Coulomb field of the atomic nucleus. Fortunately, the contribution of Bremsstrahlung to an acquired EDX spectrum can be removed by a background subtraction. The intensities of the element-specific peaks are then integrated and application of the Cliff-Lorimer equation, according to which the ratio of two signals is equal to the ratio of the contents of these elements multiplied by a factor k, yields the elemental composition.

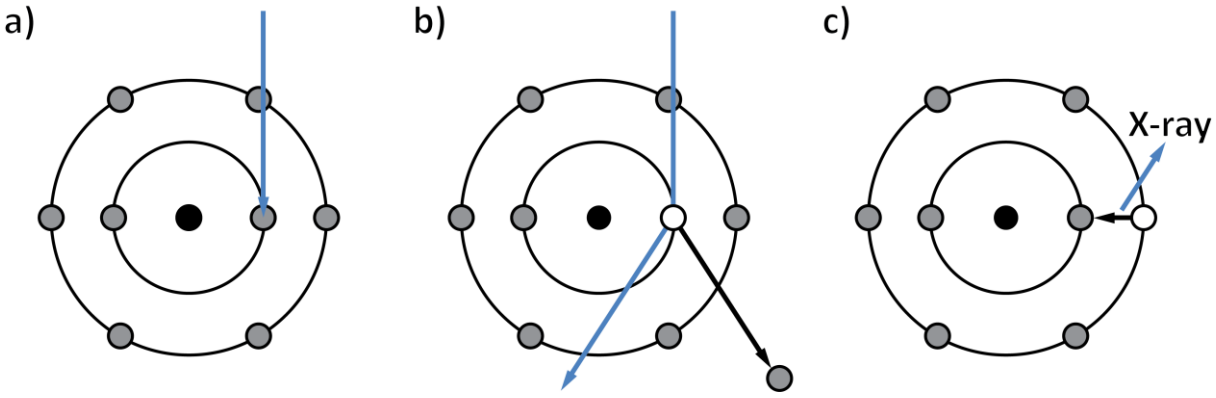

Figure 3-3: Process by which element-characteristic X-rays are generated. The primary electron beam hits the sample (a), knocking out an inner-shell electron (b). An electron from an outer shell fills this unoccupied state and the energy difference is released in the form of an X-ray (c).

The electron beam loses energy via several inelastic processes such as plasmon excitation, intraband transitions and ionization. The energy losses are characteristic for different processes which can be identified by acquiring so-called EELS spectra (Figure 3-4).[1,5,4] Below the sample and at very small scattering angles, a magnetic prism separates the electrons according to their energy. In combination with a lens system to focus and magnify the spectrum and a detector, bases on a CCD or a photodiode array, EEL spectra can be acquired. These spectra have three characteristic regions, corresponding to different dominating processes. Most electrons are elastically scattered and do not lose energy. They lead to a very intense peak centered at an energy loss of 0 eV. This zero-loss peak can be used to align the spectrometer and determine the energy resolution of measurements. The low-loss region

extends up to 50 eV. At these energy losses, plasmon excitations and band-band transitions dominate. This region is particularly useful when investigating semiconductors, as the distance of first transition from the zero-loss peak corresponds to the band gap. It further allows the analysis of plasmons, the identification of phases by fingerprinting using the plasmon position and shape, determination of the dielectric function and, when comparing it to the intensity of the zero-loss peak, of the thickness. After the low-loss region and at energy losses above 50 eV, only ionization processes occur. The onset energies of the resulting edges are characteristic for the elements the sample is composed of. Their shape depends on the shell from which the electron is removed, and the coordination number and valence state of the element. By calculating the ratios of the integrals of different edges under consideration of inelastic cross-sections, the elemental composition can be calculated. EELS therefore allows a very comprehensive analysis of several factors such as the elemental composition, bonding characteristics and the band gap.

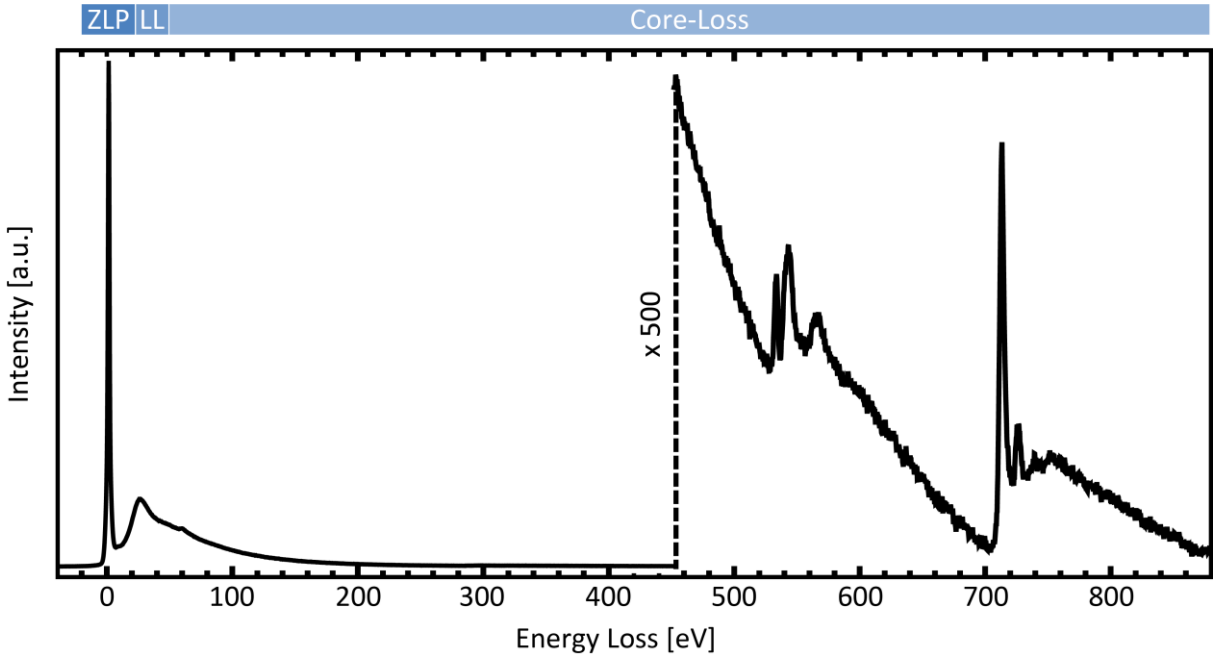

Figure 3-4: Two experimental EELS spectra of Fe_2O_3. The zero-loss peak (ZLP) and the low-loss (LL) region have significantly higher intensities than the element-specific edges in the core-loss region. The O-K edge with an onset at 532 eV and the Fe-$L_{2,3}$ signal with an onset at 708 eV are shown at approximately 500 times higher intensities than ZLP and LL region.

In comparison, both EDX and EELS have advantages and disadvantages. Measuring the signals of light elements is difficult to impossible with EDX, due to both a low fluorescence yield and the absorption of X-rays with energies below 1 kV by the detector. EELS, on the other hand, can be used to determine even low concentrations of elements down to Lithium. In contrast, the EELS edges of heavy elements are at very high energy losses and of very low intensities and measuring them is very time-intensive and can, due to insufficient signal-to-noise ratio, fail. Apart from EDX being better for heavy elements and EELS being better for light elements, the methods also differ in their ease of use. EDX measurements tend to be very fast and easy,

whereas EELS measurements require detailed and time-intensive alignment of the spectrometer prior to measurements. However, EELS spectra can provide significantly more information than EDX spectra, which only yield quantification results.

Conveniently, both methods can be used regardless of whether the beam is parallel or converged. In CTEM, the elemental composition of large areas can be quantified and average values are gained. In STEM, the spatial resolution of both methods can be driven down to, for very thin samples, even atomically resolved measurements. By collecting several spectra, line profiles and maps can be generated, allowing unprecedented analysis of materials.

3.2. Experimental Methods

3.2.1. Sample Preparation

All materials discussed in this thesis were deposited onto substrates composed of a roughly 1 mm thick glass layer and an approximately 300 nm thick fluorine-doped tin oxide (FTO) layer. Consequently, all samples could be prepared similarly for TEM analysis. Two different methods were used.

A straight-forward approach is to scratch material of the substrate using a razor blade, dispersing it in a drop of ethanol and depositing it on a copper grid coated with a holey carbon film. After drying, the sample can be used as is. Even though the geometry of the whole sample is not well-represented, sections up to several micrometers in size can be scratched off undamaged and thin enough for analysis. This quick and convenient preparation was often used to determine whether the synthesis had been successful, and for the analysis of particle sizes, HRTEM images and other features on a small length-scale.

To supplement this preparation method, complex morphologies over large length scales were analyzed by preparing cross-sections using a modified version of the technique developed by Strecker *et al*.[1,6] Compared to scratching material of the substrate, this method allows analyzing the morphology of a sample over large, electron transparent areas. Thin strips are cut out of the sample using a diamond wire saw (Well Precision Vertical Diamond Saw 3242, Figure 3-5a) and their surfaces glued together (Figure 3-5b), protecting them and doubling the area which can be investigated by TEM. Subsequently, this sandwich is embedded into a glue-filled metal tube with a diameter suitable for the TEM holder (Figure 3-5c). This stabilizes the otherwise fragile sandwich and allows easier handling. Slices with a thickness of approximately 220 µm are then cut with a diamond wire saw (Figure 3-5d) and mechanically thinned, first homogenously with a Gatan disc grinder 623 (Figure 3-5e) and then with a Gatan dimple grinder that only thins the middle of the slice (Figure 3-5f). Ar-Ion milling (Gatan Precision Ion Polishing System with both top and bottom ion guns at angles of 4°/4° as a last step thins the sample to the required electron transparency (Figure 3-5g).

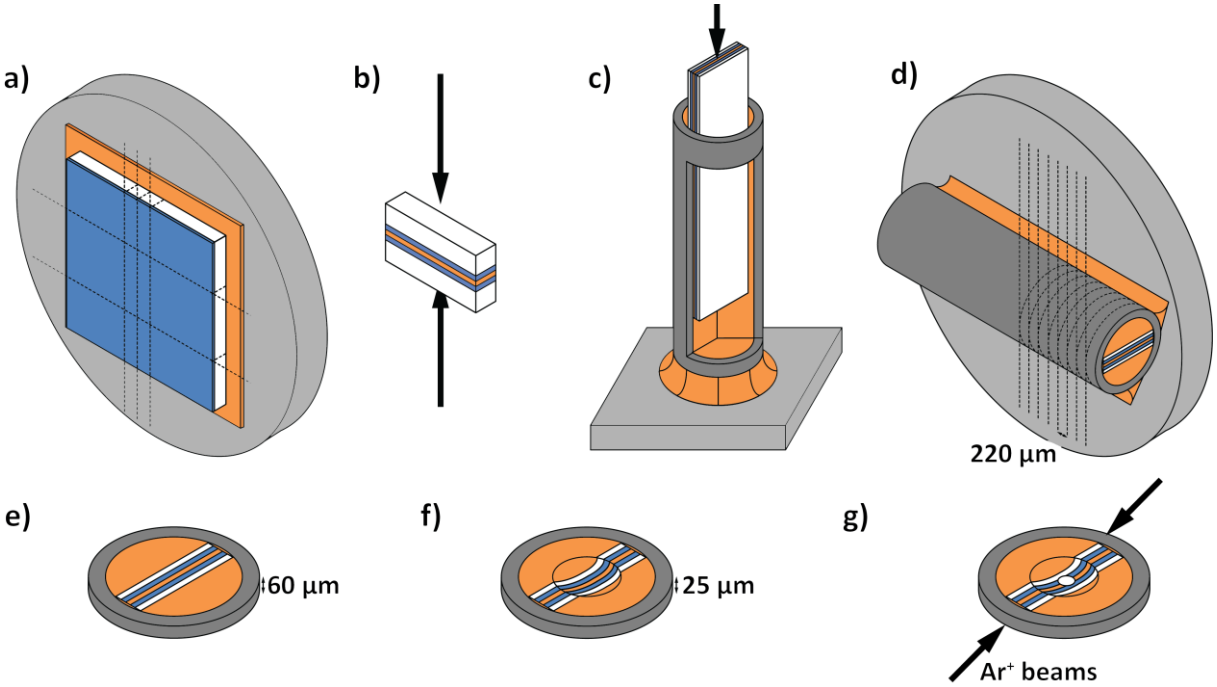

Figure 3-5: Schematic showing how cross-sections were prepared. The figure is color-coded and glues are orange, the sample surface blue, the FTO substrate white, the metal tube dark grey and sample holders light grey. Cuts are marked with dashed lines. The samples were cut into slices (a), which were then glued into a sandwich (b). The sandwich was glued into a metal tube (c), which was then cut into slices (d). Those slices were homogenously thinned (e) and then a dimple was ground into the middle of the slice (f). As a final step, the slice was thinned to electron transparency with Ar-ion beams (g).

3.2.2. Transmission Electron Microscopy Instrumentation

All experiments were done on one of two different TEMs, a FEI Titan and its successor, a FEI Titan Themis.

All measurements described in Chapter 4 were carried out on a FEI Titan(S)TEM 80-300. It was equipped with a field-emission gun (FEG) operated at 300 kV, an EDAX EDX detector, an Gatan Imaging Filter to acquire EELS spectra, a Fischione Instruments Model 3000 HAADF detector and a 2k x 2k Gatan UltraScan 1000 CCD camera.

The measurements described in the chapters 5 and 6 were conducted on a probe-corrected, monochromated FEI Titan Themis 60-300 kV. The microscope is equipped with an X-FEG operated at 300 kV, a Ceta 4k x 4k complementary metal-oxide-semiconductor (CMOS) camera and four dedicated Fischione Instruments STEM detectors: a BF detector, two ADF detectors and a HAADF detector. EDX spectra were acquired by four Super-X Bruker silicon drift detectors (SDD), EELS spectra with a Gatan Enfinium EELS spectrometer.

3.3. References

(1) Williams, D.; Carter, C. *Transmission Electron Microscopy - A Textbook for Materials*

Science; 1996.

(2) Knoll, M.; Ruska, E. *Zeitschrift für Phys.* **1932**, *78* (5-6), 318.

(3) Brandon, D. G.; Kaplan, W. D. *Microstructural Characterization of Materials*, 2nd ed.; John Wiley & Sons, 2007.

(4) Brydson, R. *Electron Energy Loss Spectroscopy*; BIOS Scientific Publishers Limited, 2001.

(5) Van Tendeloo, G.; Bals, S.; Van Aert, S.; Verbeeck, J.; Van Dyck, D. *Adv. Mater.* **2012**, *24* (42), 5655.

(6) Strecker, A.; Salzberger, U.; Mayer, J. *Prakt. Metallogr.* **1993**, *30* (10), 482.

4. Au and Au/Ag Nanoparticles on Titania Layers: Correlation of Deposition Method, Morphology and Photo(electro)-catalytic Properties

This chapter is based on a manuscript by Alexander Müller, Sandra Peglow, Michael Karnahl, Angela Kruth, Volker Brüser, Henrik Junge and Christina Scheu, which is to be submitted.

4.1. Introduction

For decades, mankind has heavily relied on fossil fuels such as coal, oil and gas as well as nuclear power.[1–3] In recent years, concerns over climate change from environmental pollution, resource depletion and nuclear safety have led to a global effort towards the development of more sustainable energies sources.[1–5] Most promising renewable energy technologies make use of the almost unlimited energy of wind and sun, for example generating electricity with wind turbines and solar cells.[2,6] However, the energy output from such sources strongly fluctuates and improved energy storage technologies are required. A promising solution is the sustainable energy carrier hydrogen, which can, for example, be burnt in fuel cells to yield electrical energy and pure water. Several solar-to-hydrogen approaches have been developed, among them solar thermochemical,[7] photovoltaic/electrolysis,[8,6] and photoelectrochemical water splitting.[9] Of these, only the last one directly converts solar into chemical energy by the photoelectrocatalytic splitting of water into hydrogen and oxygen. As well as being a highly sustainable method for the production of hydrogen as a green fuel, both products, hydrogen and oxygen, are relevant for other industries.[1,4,5,10,11] Hydrogen is, for instance, required for the hydrocracking process and the production of ammonia via the Haber-Bosch process, while oxygen is required for the smelting of iron ore into steel or the synthesis of ethylene oxide.[11]

The process of photoelectrochemical water splitting takes place at semiconducting catalysts, often metal oxides.[10,12] Titania, particularly in its low-temperature phase anatase, was the first material found to have conduction and valence band positions suitable for photocatalytic water splitting.[13,14] Other desirable properties are its high corrosion-resistance, abundance, low price and non-toxicity. Therefore, titania is still one of the most studied candidate material for photoelectrochemical water splitting.[5,15,16] The drawback of using titania as a photocatalyst are the relatively large band gaps of 3.2 eV for the anatase modification and 3.0 eV for the rutile phase, leading to absorption edges at 386 and 416 nm, respectively.[16,17] Accordingly, high efficiencies can only be reached within or near the UV region, which accounts for merely 5% of the total energy of the solar spectrum.[18,19] This limits the maximum

efficiency to 1.3 % for anatase and 2.2 % for rutile.[16] As the performance strongly depends on the band gap, it can be enhanced by either narrowing the band gap via doping and/or by depositing a second light-absorbing material that absorbs in the visible region and acts as a photosensitizer.[18,20,21] Popular photosensitizers, at least in dye-sensitized solar cells, are (metal)organic dyes.[22,23] They are, however, often unstable under the harsh conditions present during water splitting.[22]

A second group of photosensitizers are nanoparticles consisting of noble metals such as Pt, Pd, Au or Ag. Light can induce a localized collective electron oscillation at the surface of these nanoparticles.[19,20,24,25] The energy of this so-called localized surface plasmon resonance (LSPR) and therefore the wavelength of the absorbed light strongly depend on the size, shape, material and environment of the nanoparticle.[19,20,25,26] By manipulating these parameters, the wavelength of the surface plasmon resonance (SPR) can be shifted to absorb visible or even near-infrared light.[19,20,25–28] Plasmon-induced electrons can be transferred to titania which is a good electron-acceptor due to its high density-of-state conduction band,[21] increasing the efficiency of the photoelectrochemical reaction. The large scattering cross section related to the plasmon oscillation in noble metal nanoparticles can enhance the optical pathway of the incident photons leading to increased light absorption.[29] In addition to their function as photosensitizer, noble metal nanoparticles can act as co-catalysts by providing chemically active sites with low activation barriers for chemical reactions, prolonging charge carrier lifetime, and serve as a sink for electrons generated in the titania by UV light.[30,31]

So far, most studies were carried out on suspended powders.[31–33] However, unless sacrificial agents are used, O_2 and H_2 are produced in close proximity and the back-reaction is very likely.[34] In contrast, if titania is deposited onto electrodes and either a bias voltage is applied or a sacrificial agent is added, the reactions can be spatially separated, suppressing the back reaction towards water. In this work, anatase thin films were prepared by magnetron sputtering and Au nanoparticles were deposited on them by two different methods, *in situ* photodeposition and radio frequency (RF) magnetron sputtering.[32,35,36] As, bimetallic nanoparticles often show significantly increased catalytic activity compared to the respective monometallic nanoparticles, the latter method was also used for the preparation of Au/Ag nanoparticles.[37,38] The two synthesis procedures produced vastly different particle distributions, particles size distributions and defect structures, all of which could be correlated to the synthesis procedures. We further measured light absorption spectra and the photocatalytic evolution of hydrogen using the sacrificial agent MeOH. The results could be correlated to the structural investigation. By providing an in-depth understanding of the interplay between synthesis conditions, structure and properties, we hope to contribute to future improvements of the system.

4.2. Materials and Methods

4.2.1. Plasma-Deposition of Titania Films

Titania films were deposited onto fluorine-doped tin oxide substrates (FTO, TCO 22-7, Solaronix, 25 x 25 mm) by a direct current (DC) reactive magnetron sputtering process as previously described by Kruth *et al.*[35] The Ti target (Ti-133, Bekaert Advanced Coatings NV) was sputter-cleaned in an Ar atmosphere at 8 kW for 5 min. After stabilizing the process conditions in an O_2/N_2/Ar atmosphere (6 standard cm^3/min (sccm) O_2, 3 sccm N_2, and 60 sccm Ar) at 3 Pa for 8 min, TiO_2 was plasma-deposited at a magnetron power of about 5.3 kW and a magnetron voltage of 450 V. To transform the resulting amorphous TiO_2 into anatase, the samples were annealed for 1 h at 400 °C with a heating rate of 10 °C/min in an oxygen atmosphere at a flow rate of 0.05 standard l/min (slm).

4.2.2. Plasma-Deposition of Au and Au/Ag Nanoparticles

Au and Au/Ag core-shell nanoparticles were deposited onto the titania films described above using a RF-magnetron sputtering process previously published by Peglow *et al*.[36] A benefit of this method is the adjustability of composition and size distribution by alternating deposition and annealing steps. A 3 mm thick Au sputtering target (99.999 %, MaTeck) and a 3 mm thick Ag sputtering target (99.999 %, MaTeck) were placed at respective distances of 9.5 and 5.5 cm from the substrate. Small sputtering rates were achieved by shielding the magnetic field with a 1 mm thick iron disk (99.95 %, MaTeck) placed between the magnetron and the two targets. The deposition was performed at a power of 50 W in a 5 Pa argon atmosphere (15 sccm gas flow). To anneal the films, the samples were placed in a quartz tube which was inserted into a tube furnace (Zirox GmbH) kept at 400 °C by a thermal controller (Eurotherm 2416) for 30 min. The O_2 atmosphere (0.05 slm) was regulated using a gas flow controller (MKS Instruments Multi Gas Controller 647B). Au nanoparticles were synthesized by depositing gold for 300 s, which correlates to a nominal layer thickness of 8 nm, annealing, depositing for another 300 s and annealing once more. To obtain Au/Ag core-shell nanoparticles, Au-deposition for 188 s (5 nm nominal layer thickness) was followed by Ag-deposition for 36 s (3 nm nominal layer thickness) and another annealing step.

4.2.3. *In situ* Photodeposition of Au Nanoparticles

A second series of Au nanoparticles was prepared by *in situ* photodeposition onto titania films following a synthesis procedure described by Gärtner *et al*.[32] The temperature of a double-walled reaction vessel was adjusted to 25 °C by a thermostat and a titania film (25 x 25 mm) inserted into the reactor with a glass holder. Subsequently, the gold precursor ($NaAuCl_4$ x 2 H_2O, 3.1 mg) was added. The whole system was evacuated and flushed with argon to remove any other gases. Then, 40 ml freshly distilled water and 40 ml methanol were added under argon counter flow, resulting in a final concentration of the gold precursor of about

0.1 mmol/l. Photodeposition of the gold nanoparticles was initiated with a Hg-lamp (7.2 W output, Lumatec Superlite 400) equipped with a 320-500 nm filter.[32] A swift color change from light yellow to dark red occurred, with the formed hydrogen escaping by a bubbler. The reaction was stopped after 3 h and the sample was washed with deionized water and ethanol prior to drying in air.

4.2.4. Structural and Morphological Characterization

Phase identity and crystallite sizes were determined from grazing incident X-ray diffractograms (GIXRD). These were measured in a 2Θ-range of 20-80 ° on a Bruker D8 Advance with a Cu-Kα source, an incident angle of 0.5 °, a step width of 0.02 ° and 5 s per step. Crystallite sizes were calculated from the (200) reflection of Au using a combination of Stokes-Wilson and Variance model and fitting the correlated integral widths by a Pearson VII function.[39]

Scanning electron microscopy (SEM) was performed on a Jeol JSM 7500F with a field emission gun, a semi-in-lens conical objective lens and a secondary electron in-lens detector. An acceleration voltage of 15 keV enabled a resolution of 1.0 nm.

A comprehensive structural analysis was done using a FEI Titan 80-300 transmission electron microscope (TEM). Bright-field (BF) and high-resolution TEM (HRTEM) images were recorded on a Gatan UltraScan 1000 CCD, scanning TEM (STEM) images with a Fischione Model 3000 high-angle annular dark-field (HAADF) detector and energy-dispersive X-ray (EDX) spectra with an EDAX system. Samples were prepared by either scratching material of the substrate and depositing it onto a TEM grid with a holey carbon film or by preparing a cross-section according to a procedure adapted from Strecker *et al*. so that the sample was prepared at room temperature.[40]

4.2.5. Optical Characterization

The optical properties of the different layers were investigated using a PerkinElmer Lambda UV-Vis 850 spectrophotometer with an integration sphere (L6020322 150 mm). Calibrated Spectralon Reflectance Standards (>99 % R, USRS-99-020, PerkinElmer Inc.) were attached to provide high reflectivity inside of the sphere. The UV/vis spectra were recorded from 250 nm to 850 nm in transmission mode. Calculation of the absorbance A was carried out under the assumption that no reflection occurs at the sample using the following equation:

$$A = -\log_{10}(I_T/I_0),$$

Where A is the absorbance in arbitrary units, I_T is the measured transmission intensity in percent and I_0 is the incident light intensity, which equals 100 %.

4.2.6. Photocatalytic Measurements

Photocatalytic hydrogen evolution experiments were performed under argon atmosphere with freshly distilled solvents. The sample was introduced into a double-walled, thermostatically-controlled reaction vessel by a glass holder and aligned in parallel to the planar optical window. Subsequently, the photoreactor was connected to an automatic gas burette and repeatedly evacuated and filled with argon. Then, the solvent mixture (80 ml), composed of water and methanol in a ratio of 1/1 (v/v), was added, fully covering the layer. The temperature of the whole system was maintained at 25 °C by a thermostat. After stirring for at least 10 min at 300 rounds per minute to reach thermal equilibrium, the reaction was started by switching on a Hg-lamp (7.2 W output, Lumatec Superlite 400) equipped with a 320-500 nm filter. The amount of evolved gases was continuously monitored by the automatic gas burette, while the gas composition was analyzed by gas chromatography. A more detailed description of the experimental setup has been published previously.[32]

4.3. Results and Discussion

4.3.1. Structural and Morphological Characterization

Three samples total were characterized in depth. Au and Au/Ag core-shell nanoparticles were deposited onto an anatase layer using a radio frequency magnetron sputtering process in combination with subsequent thermal treatment. Au nanoparticles were further prepared by *in situ* photodeposition. GIXR diffractograms (Figure 4-1) proved the successful and phase-pure synthesis of all samples. Annealing the deposited, amorphous titania in an oxygen atmosphere leads to formation of the anatase modification with an average crystallite size of 25 nm. The Au and Au/Ag nanoparticles possess the fcc structure typical of the bulk phase.[41] The Au reflexes of photodeposited Au-TiO_2 are much weaker than in the other two samples, indicating either lower loading or, as the intensity of GIXRD decreases with increasing penetration depth, that they are inside the titania layer. The average crystallite sizes were determined from GIXRD data as 4 nm, 7 nm and 7 nm of Au nanoparticles synthesized by *in situ* photodeposition and of Au and Au/Ag nanoparticles prepared by plasma-deposition were, respectively. Given that the nominal layer thicknesses of plasma-deposited Au/Ag-TiO_2 is half of that of plasma-deposited Au-TiO_2, both plasma-deposited nanoparticles having the same crystallite size is surprising and hints at a complex interplay of different processes. The crystallite size of the noble metal nanoparticles in photodeposited Au-TiO_2 is much smaller, however, determination of the average particle size of this sample is error-prone due to the low intensity of the Au peaks.

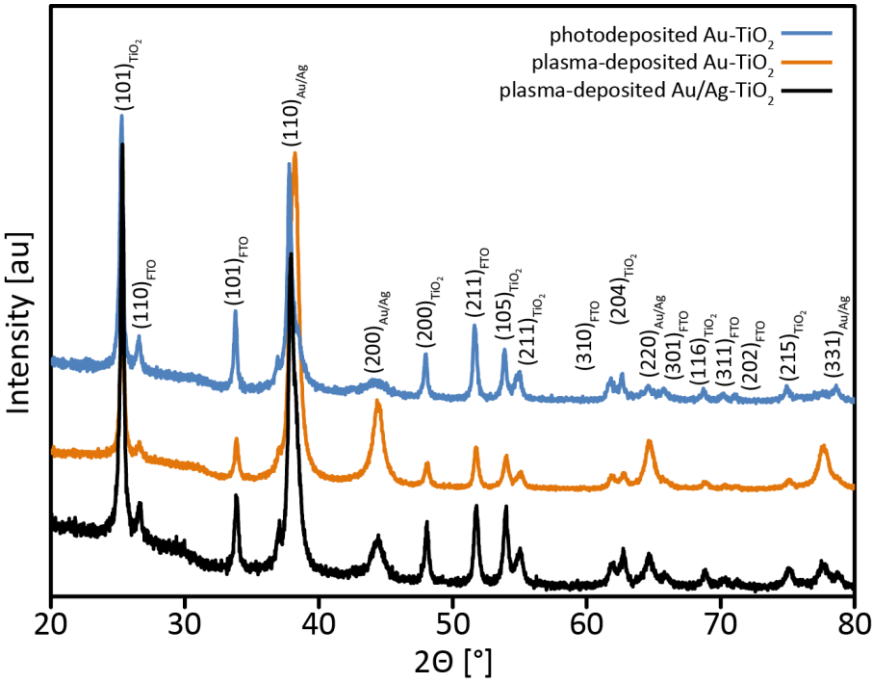

Figure 4-1: GIXR diffractograms of the samples on which noble metal nanoparticles were deposited. A GIX diffractogram of the pure TiO_2 film can be found in the literature.[35,42]

Figure 4-2 shows overview images of the different samples. Top-view images were acquired by SEM (Figure 4-2a, b and c), cross-sections by HAADF-STEM (Figure 4-2d, e and f).

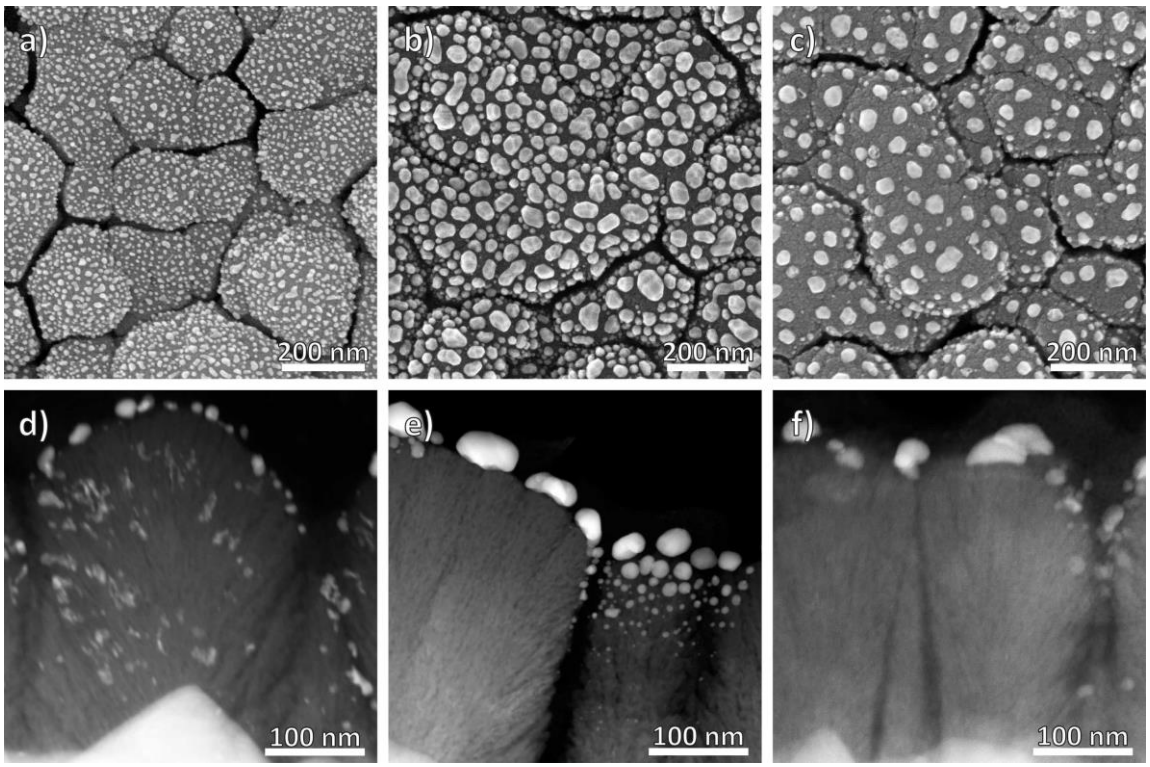

Figure 4-2: Top-view SEM and cross-section STEM images of photodeposited Au-TiO_2 (a and d), plasma-deposited Au-TiO_2 (b and e) and plasma-deposited Au/Ag-TiO_2 films (c and f).

The titania layer is polycrystalline, approximately 300 nm thick and composed of individual pillars, each of them grown on a FTO pyramid. The fibrous titania pillars are in the anatase modification, with 3-5 nm thick pores elongated in the direction perpendicular to the TiO_2/FTO interface. The porosity of the titania was quantified from HAADF-STEM images. The signal intensity I in such images scales with the mean atomic number Z raised by an exponent y. As FTO and the underlying SiO_2 substrate it is deposited on are compact layers, y can be calculated. The mean atomic number of the titania layer is then given by:

$$\frac{I_{Titania}}{I_{FTO}} = \left(\frac{Z_{Titania}}{Z_{FTO}}\right)^{y} \qquad \rightarrow \qquad Z_{Titania} = Z_{FTO} \cdot \sqrt[y]{\frac{I_{Titania}}{I_{FTO}}}$$

The porosity is equal to the ratio of the mean atomic numbers of the measured, porous and the theoretical, compact layer and was determined as ~ 10 %, indicating low porosity.

The photodeposited Au nanoparticles are found both on top of and inside the TiO_2. The latter indicates that some of the pores are open at the surface and can be filled with the precursor solution. Accordingly, wetting of these pores, both by the precursor solution during the photodeposition and by the electrolyte during the photoelectrochemical and hydrogen evolution experiments, can be assumed. In contrast, the RF-sputtered noble-metal nanoparticles (Au and Au/Ag) occur only on top of the titania layer. This is typical for vapor-deposition processes in which the nanoparticles are formed in the gas phase. The particles in the cavities are significantly smaller than on top (Figure 4-2). Compared to plasma-deposited Au-TiO_2, only half the nominal layer thickness was deposited during the synthesis of plasma-deposited Ag/Au-TiO_2. (Figure 4-2b and c). This reduction leads to a sparser distribution of nanoparticles of roughly the same size. The half-as-high loading was also confirmed by EDX measurements (Table 4-1). The noble metal content could be determined by calculating the mass of the TiO_2 layer from the thickness and the density and comparing it with the ratio of noble metals to Ti. In contrast, the masses of deposited Au in photo-deposited Au-TiO_2 and plasma-deposited Au-TiO_2 are very similar.

Table 4-1: Noble metal content of the three samples.

	Au-content [µg/cm^2]	Ag-content [µg/cm^2]
photodeposited Au	17.5 ± 3.7	-
plasma-deposited Au	19.6 ± 6.5	-
plasma-deposited Ag/Au	7.8 ± 3.4	1.4 ± 0.8

In Figure 4-3, size distributions of all three samples are shown. Photodeposited Au nanoparticles grew both inside and on top of the Titania layer, and two different size distributions were evaluated to reflect this. Photodeposited Au nanoparticles inside the titania layer, which account for 66 % of all Au nanoparticles, have a different size distribution than the nanoparticles found on top of the titania layer (Figure 4-3a) A log-normal distribution,

which has previously been successfully applied to the size distributions of Au nanoparticles synthesized by several, solution-based synthesis procedures,[43] could be used to describe them both. The size distribution of Au nanoparticles inside the titania is shifted towards smaller diameters, indicating that the growth is slowed down or stopped within the pores of the titania layer.

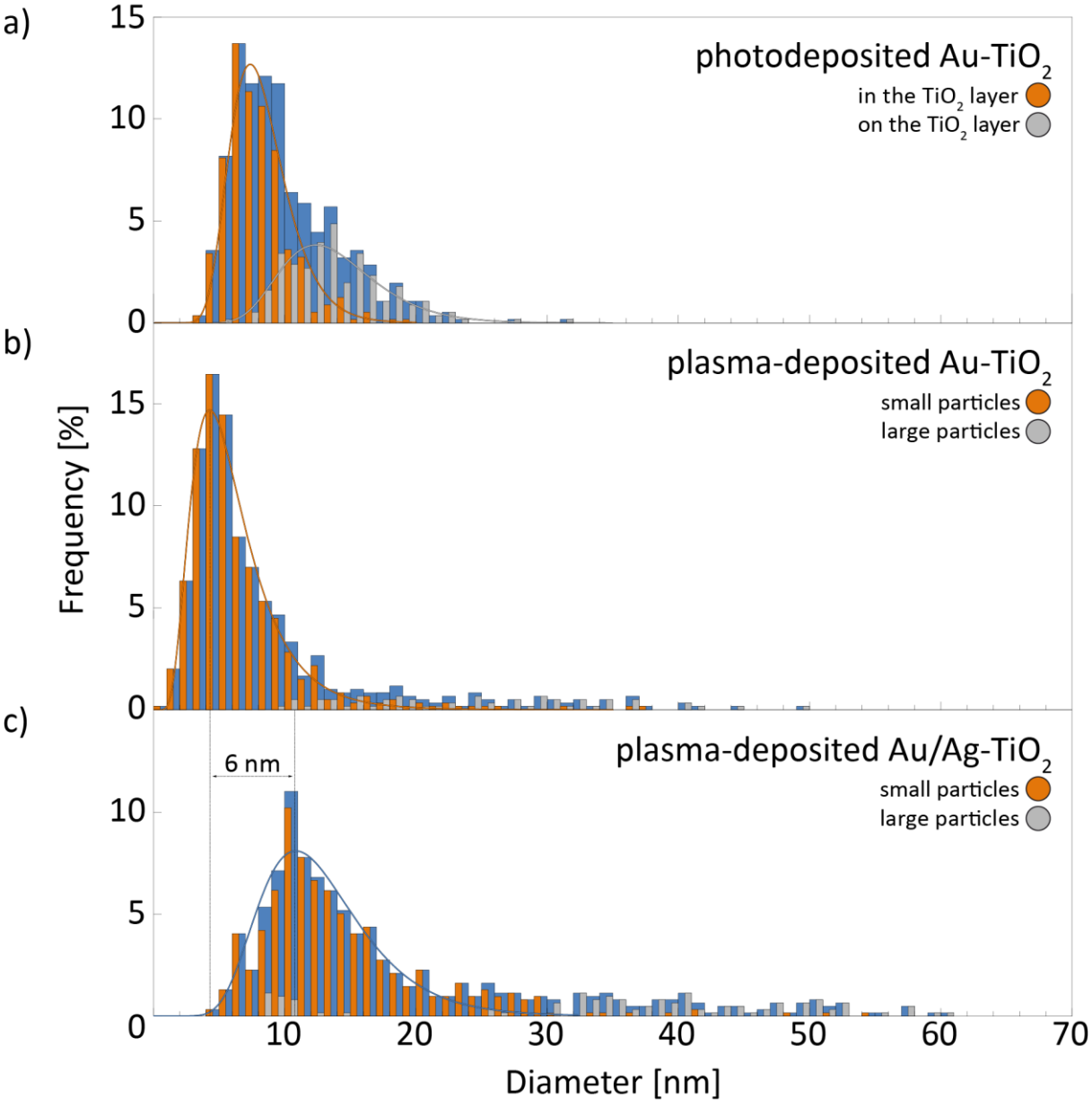

Figure 4-3: Size distributions of the noble metal nanoparticles in a) photodeposited Au-TiO_2, b) plasma-deposited Au-TiO_2, c) plasma-deposited Ag/Au-TiO_2. All size distributions were split into two sub-distributions each. Please note that the frequency values only apply to the size distribution of the whole sample, but not to the sub-distributions.

To interpret the size distributions of plasma-deposited particles (Figure 4-3b and c), two underlying processes, deposition and annealing, have to be considered. Previous studies have

shown that nanoparticle growth in the gas phase leads to a log-normal size distribution, whereas the annealing step should, via a coarsening mechanism, lead to larger particles not described by the initial log-normal distribution.[44,45] The coarsening step is expected to depend strongly on a low surface roughness to prevent particle pinning and facilitate particle diffusion. We used these assumptions to split each size distribution in two by considering large nanoparticles at the top of smooth TiO_2 surfaces result from a coarsening mechanism. With this assumption, the non-coarsened particles, which account for 86 % in plasma-deposited Au-TiO_2 and 83 % in plasma-deposited Au/Ag-TiO_2, can be fit very well with a log-normal distribution. Attempts to model the other particle fraction with a size distribution failed due to an insufficient signal-to-noise ratio. Compared to pure plasma-deposited Au nanoparticles, the maximum of the log-normal distribution of smaller, non-coarsened Au/Ag nanoparticles is shifted from 4 to 10 nm (Figure 4-3b and c). This size increase, in spite of the reduced nominal layer thickness, indicates that the formation of Au nanoparticles in the gas phase dominates in directing their size, and not the subsequent Ag deposition or the annealing step, and hints at the shift being a result of Ag being added to pre-existing Au nanoparticles. Of course, this argument only applies to non-coarsened, small nanoparticles.

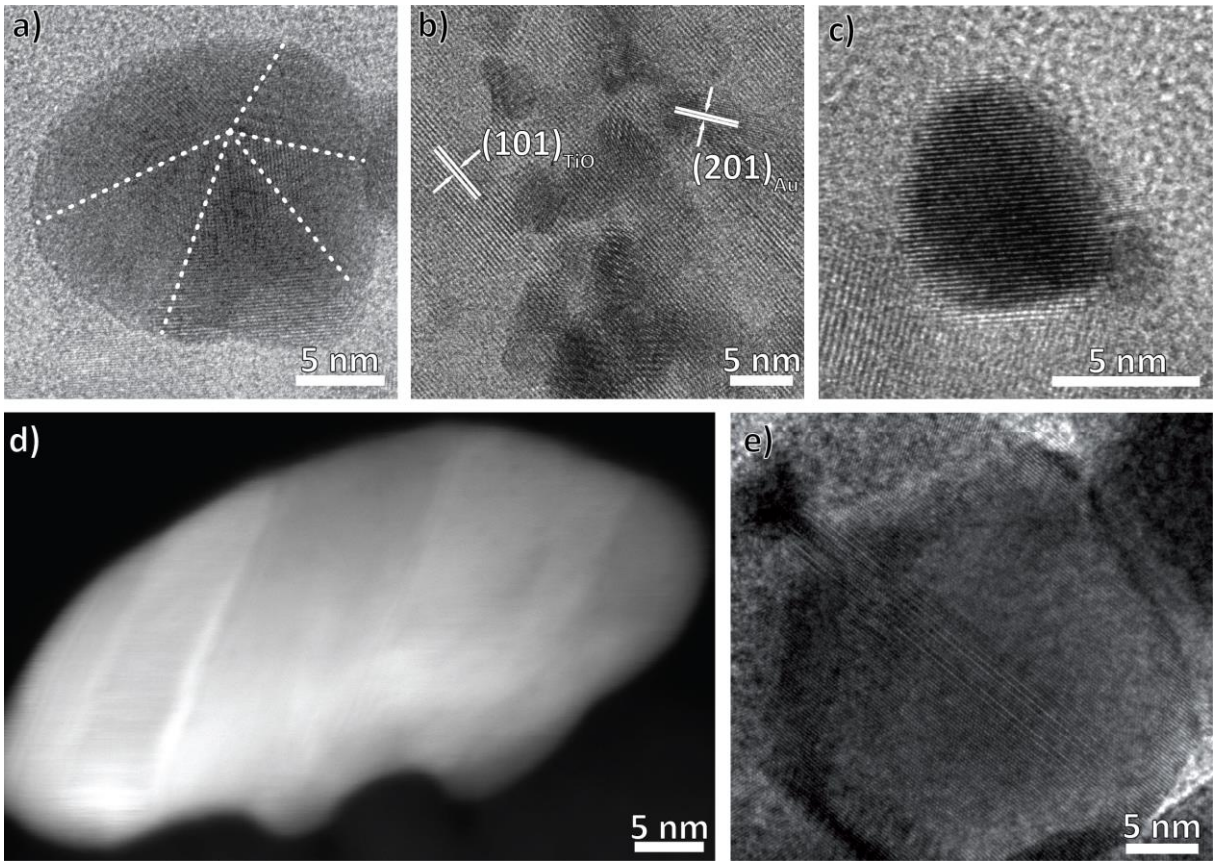

Figure 4-4: Representative images of different defect structures of the noble metal nanoparticles. In (a) and (b) HRTEM images of the photodeposited Au nanoparticles are shown: (a) is a five-fold twinned particle on top of the titania and (b) an agglomerate of defect-free nanoparticles inside the titania. (c), (d) and (e) show RF-sputtered nanoparticles: (c) is representative for small, defect free nanoparticles, (d) of those with stacking faults and (e) of those with grain boundaries.

The nanoparticles possess several different defects (Figure 4-4). The photodeposited Au nanoparticles can be inside and outside of the titania layer, with each fraction having its own predominant defect structure. Photodeposited nanoparticles on top of the titania are predominantly five-fold twinned, with few occurrences of other defect structures such as grain boundaries. Such a twinning is energetically favorable for small nanoparticles and therefore very common.[46–50] In contrast, all particles observed inside the titania were monocrystalline. However, a definite correlation of nanoparticle size and defect structure could not be concluded. The existence of defects not inherent to the metal, such as an oxide shell, could be excluded from HRTEM images and EDX analysis.

For the plasma-deposited nanoparticles, we observed single-crystallinity, five-fold twinning, stacking faults and grain boundaries (Figure 4-4). As with the photodeposited nanoparticles, we could not conclude a correlation of size and defect structure, with the exception being grain boundaries which were very common in big nanoparticles. We tentatively ascribed these to the coarsening process. These particles also often have little protrusions that fill nooks in the titania substrate. Once again, other defects such as an oxide shell can be excluded from HRTEM images and EDX STEM measurements.

The interface between the titania substrate and the nanoparticles was investigated by HRTEM, but a well-defined orientation relationship between the particles and the substrate could not be observed.

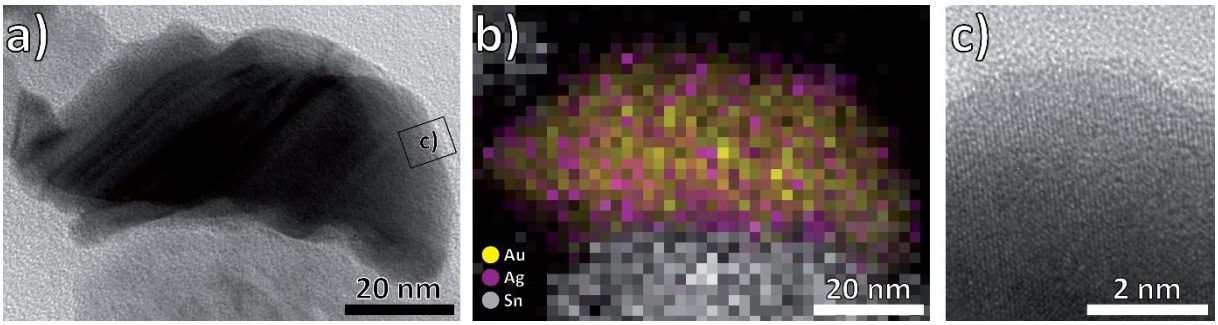

Figure 4-5: a) BF images of a representative Au/Ag nanoparticle, b) EDX map of the same particle, showing a clear accumulation of Ag at the surface, c) HRTEM image of the nanoparticle surface area.

Bimetallic Au/Ag nanoparticles could potentially be alloyed or form core-shell nanoparticles.[51,52] The melting temperatures of Ag and Au decrease with decreasing nanoparticle sizes, but are always high compared to the highest temperature reached during synthesis (400 °C).[53,54] Alloying therefore seems unlikely. In accordance, EDX maps confirmed the formation of a uniform, 2-3 nm thick Ag shell around the Au core. Thanks to both metals crystallizing in the face-centered cubic structure and their lattice parameters differing by only 0.2 %, we observe defect-free continuation of the crystal structure of Au by Ag (Figure 4-5).[41] Previous studies have shown inhomogeneous deposition of gold and silver, and the core-shell nanoparticles presumably result from nanoparticle attachment during the annealing

treatment.[36,55,56] Interestingly, previous experiments by one of the co-authors, in which the Ag/Au deposition order was reversed, also yielded Au/Ag-core-shell nanoparticles.[36] The deposition order can therefore not be the decisive factor when determining which metal becomes the core and which the shell. Unfortunately, growth mechanism studies so far mostly focus on wet-chemical synthesis methods and do not apply to our synthesis method.[57,58] Looking at the thermodynamics of the two possible core-shell configurations, four different enthalpy contributions must be considered: one each for bulk Au and bulk Ag, the interface between Ag and Au, and the surface of the shell material. Of these, only the contribution of the surface changes when exchanging core and shell material. As the surface energies of Au are approximately 40 % higher than those of Ag, we assume this to be a major driving force for the creation of Au/Ag core-shell nanoparticles over Ag/Au core-shell nanoparticles.[59]

4.3.2. Optical Properties

The influence of the noble metal nanoparticles on the light harvesting was investigated by UV-Vis measurements (Figure 4-6). Pure anatase was measured as a reference and has an indirect band gap of 3.2 eV,[16,17] which was previously confirmed for the titania layers used in this work.[35] This results in strong absorption below wavelengths of 386 nm dropping off to a constant, low absorption in the visible range due to FTO and glass.

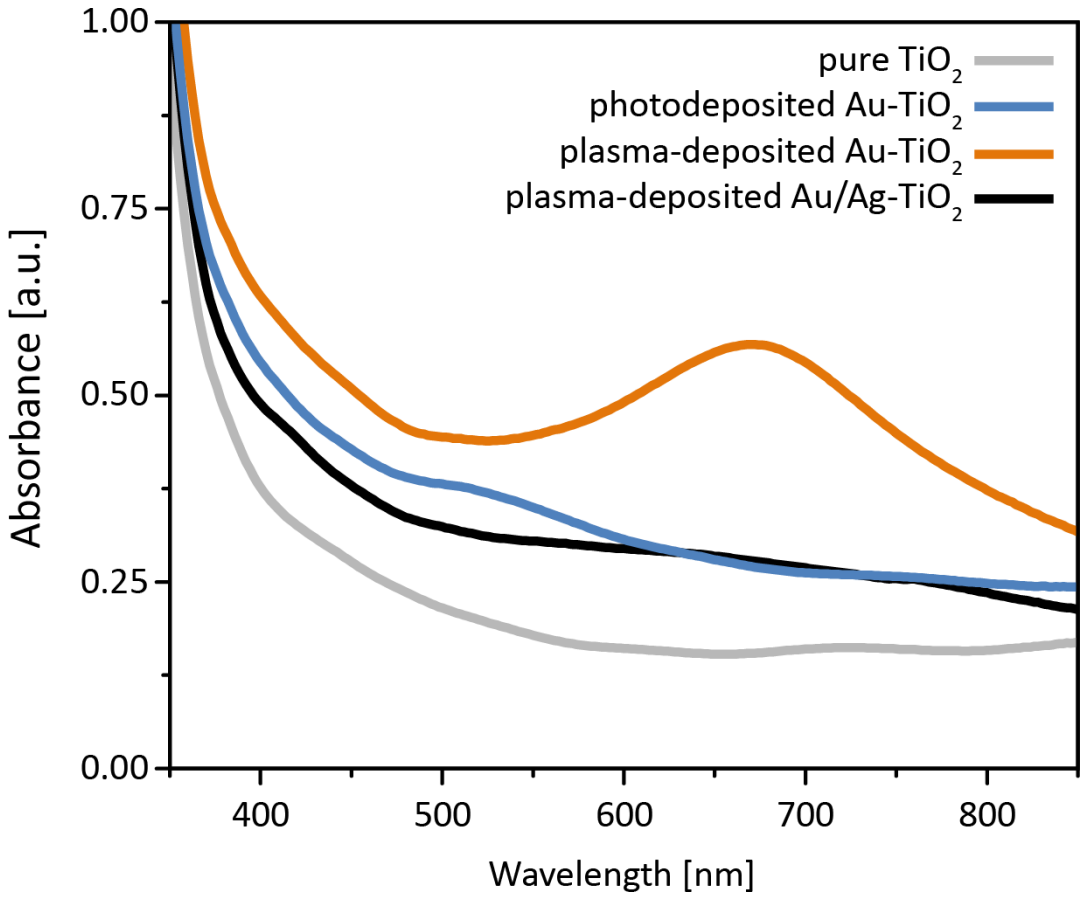

Figure 4-6: UV-Vis spectra of all samples.

Plasma-deposition of Au nanoparticles leads to strong absorbance between 550 and 850 nm, which can be attributed to plasmon excitation (Figure 4-6). These nanoparticle show a high absorption intensity, probably because the resonance is undisturbed from inter-band transitions damping occurring close to the optical cut-off frequency of titania.[60,61] For spherical, isolated gold nanoparticles in a vacuum, enhanced absorption due to a LSPR would occur at about 520 nm.[60,62] The strong shift to higher wavelengths found in our measurements can have several reasons. First, it can be explained by the deviation from the ideal spherical shape. Irregular geometries mainly possessed by coarsened particles having grain boundaries and protrusions lead to asymmetric oscillations resulting in, for the example of ellipsoids, longitudinal and transversal plasmon modes, with the former shifting the resonance frequency towards higher wavelengths.[29,60,61,63] Besides the strong influence of the particle shape, the dielectric properties of the surrounding media have a strong effect on the position of the absorption band, and shift it towards longer wavelengths compared to a vacuum.[64] Because of anatase's high refractive index of 2.5 and the gold nanoparticles adapting to the titania morphology and sharing a large interface area with it, this effect has to be considered.[65] It is even more pronounced for non-spherical particles.[60] The redshift could further be caused by near-field coupling of neighboring particles, which would be particularly pronounced for gap/particle diameter ratios smaller than 0.2, which is fulfilled by the coarsened gold particles on top of the titania surface. This plasmon coupling might lead to the formation of "hot spots" in the particle vicinities.[19,63,64] Because the particles are randomly oriented, the measured absorption spectrum is an overlay of all excited plasmon modes. Hence, the peak broadening can be related to contributions of differently shaped nanoparticles. As the nanoparticles are significantly smaller than the irradiation wavelengths, radiation processes such as plasmon-enhanced scattering can be neglected.[64]

The UV-Vis spectrum of photodeposited Au-TiO_2 differs considerably from that of plasma-deposited Au-TiO_2 in intensity, position and width of the absorption band (Figure 4-6). The comparatively low absorption amplitude could be due to overlap of the LSPR with the gold inter-band transitions from d- to sp-bands leading to dampening at energies greater than 2.4 eV.[21,60,61] The absorption band is located between 480 and 600 nm, indicating spherical nanoparticles like the five-fold twinned structures found on top of the titania and small aspect ratios for elongated particles.[60] As more than half of the particles are found inside the pores, the effect of the dielectric constant of the surrounding titania matrix has to be considered. However, a potentially resulting red-shift of the absorption band cannot be discerned.

In contrast to the two Au-TiO_2 samples, plasma-deposited Au/Ag-TiO_2 does not exhibit an explicit absorption band but shows nearly uniform absorption throughout the visible region with negligible shoulders at 400 - 450 nm and 480 - 540 nm (Figure 4-6). Since both metals show plasmonic behavior, the resonance frequency of Au/Ag core-shell nanoparticles is expected to lie between the 420 nm found for silver and the 520 nm found for gold.[29] A combination of shape variation and resultant deviation in the Au/Ag-ratio might prevent single absorption band formation. Moreover, exceedingly large particle sizes could give rise to higher-order multipole excitation and an additional broadening caused by radiation damping

dominated in large particles.[61] Due to sparse surface coverage, the nanoparticle can be regarded as isolated and near-field coupling can be neglected.

4.3.3. Photocatalytic Properties

Previous experiments conducted with the hole scavenger methanol and under UV illumination have confirmed a drastic increase in hydrogen production upon deposition of noble metal nanoparticles onto TiO_2.[32,66,67] This was confirmed in our experiments, with all samples having an increased hydrogen evolution rate (between 9 and 15 times) compared to pure TiO_2 (Figure 4-7, Table 4-2). To our knowledge, all experiments published so far under similar experimental conditions were conducted on powders. As these results are typically normalized to the mass of the photoabsorber, comparison with our experiments is difficult.

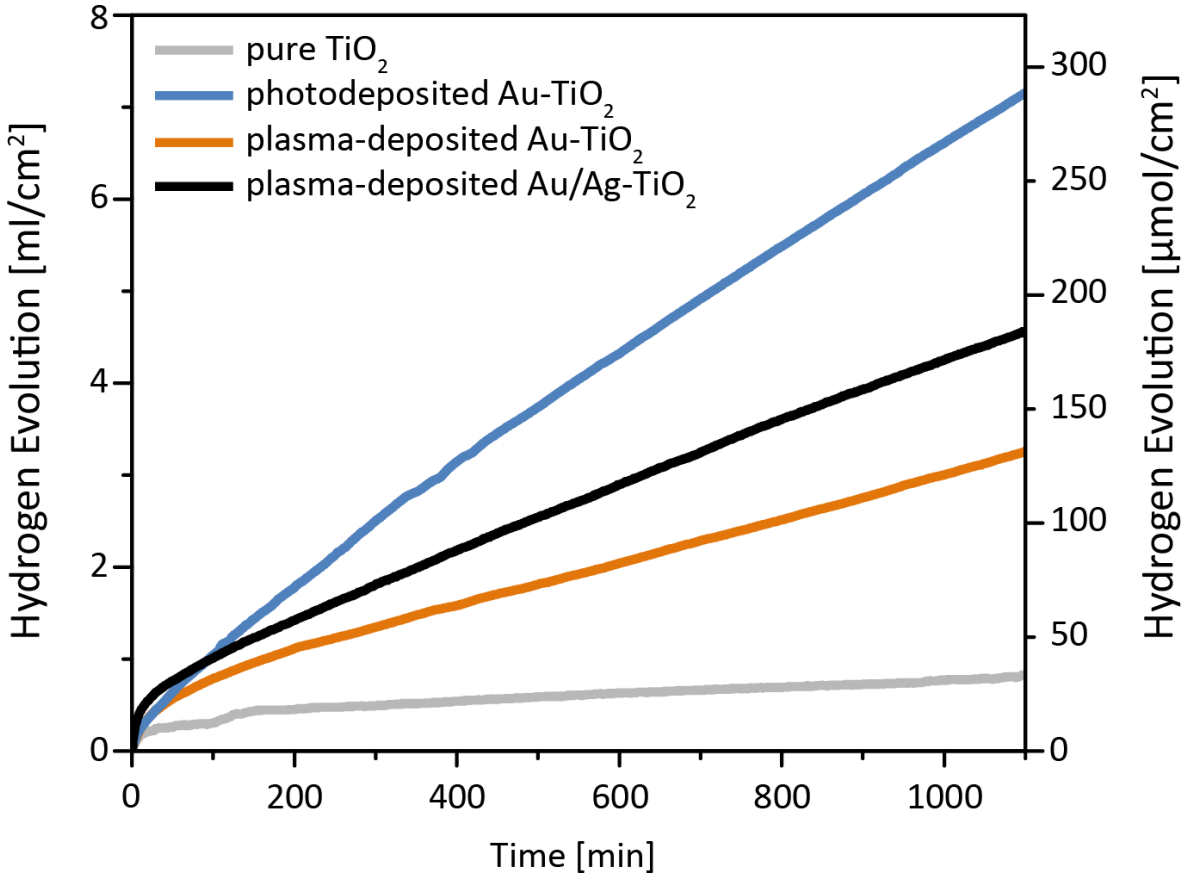

Figure 4-7: Hydrogen evolution over time of the TiO_2 samples with three different noble-metal nanoparticles in comparison with pure TiO_2. The measurements were conducted using the sacrificial agent MeOH and under UV illumination.

Table 4-2: Photocatalytic hydrogen rates of the three noble-metal-TiO_2 samples and of pure TiO_2 determined using the sacrificial agent MeOH and under UV illumination.

	Hydrogen [µl/(h·cm^2)]	Hydrogen [µmol/(h·cm^2]
pure TiO_2	22.1	0.9
photodeposited Au-TiO_2	345.0	13.9
plasma-deposited Au-TiO_2	250.6	10.1
plasma-deposited Ag/Au-TiO_2	205.3	8.3

The measurements show strong initial hydrogen production, followed by a smaller, constant evolution rate. Such behavior is typical of reactions with gaseous products and is related to the bubble evolution process reaching equilibrium.[68,69] The constant region is therefore more representative of the longtime operation desired for industrial applications and we disregarded the first hour of each measurement to determine the hydrogen evolution rates shown in Table 4-2. Photodeposited Au-TiO_2 performs best, with plasma-deposited Au/Ag-TiO_2 second, plasma-deposited Au-TiO_2 third and pure TiO_2 last. It must be pointed out once more that these experiments were conducted under UV light and that the gold nanoparticles only act as co-catalysts. Under visible light illumination, the strong LSPR excitation in plasma-deposited Au-TiO_2 (Figure 4-6) could lead to a different order.

Photodeposited Au-TiO_2 and plasma-deposited Au-TiO_2 have a similar Au-loading as well as similar particle sizes (Table 4-1, Figure 4-3). They mainly differ in the particle distribution, with the first of the two having Au nanoparticles embedded inside the TiO_2 layer. This embedding could lead to a high interface area between gold and titania and to better charge transport, reduced recombination losses and an enhanced performance. Of the two samples with plasma-deposited nanoparticles, Au/Ag-TiO_2 outperforms Au-TiO_2 in spite of the reduced loading (Table 4-1). This is in accordance with previous publications, in which bimetallic nanoparticles outperforming monometallic ones was explained by electron transfer from the Ag shell to the Au core modifying the electronic structure and creating extremely active surface sites.[37,38]

4.4. Conclusion

In this study, structure, optical properties and photocatalytic performance of a total of four samples were determined and compared. A bare TiO_2 film acted as the reference, onto which Au nanoparticles were photo or plasma-deposited. In addition, Au/Ag core-shell nanoparticles were plasma-deposited. Plasma-deposited nanoparticles only grew on top of the TiO_2 layer, whereas photodeposited nanoparticles also infiltrated it. A wide variety of crystal defect structures was found for the nanoparticles in all samples. Only plasma-deposited Au-TiO_2 showed a significant LSPR effect, and band position, broadening and intensity of the LSPR bands of all samples could be explained by a combination of several effects. The water splitting performance was measured with the hole scavenger methanol under UV illumination, and

photodeposited Au-TiO_2 was found to perform best. Of the plasma-deposited samples, Ag/Au-TiO_2 outperformed Au-TiO_2 regardless of a lower noble metal content. By combining synthesis details, morphological investigation and properties, we hope to contribute to an enhanced understanding of the materials system and aid further synthesis approaches.

4.5. Acknowledgements

We would like to thank the DFG SPP 1613 for financial support and for facilitating this collaboration. We are also grateful to Markus Döblinger and Steffen Schmidt for support with TEM measurements, Christoph Heinzl for additional SEM measurements, Harm Wulff for in-depth analysis of the GIXRD measurements and Petra Bartels for help with the catalytic experiments.

4.6. References

(1) Armaroli, N.; Balzani, V. *Angew. Chemie - Int. Ed.* **2007**, *46* (1-2), 52.
(2) Schiermeier, Q.; Tollefson, J.; Scully, T.; Witze, A.; Morton, O. *Nature* **2008**, *5* (August), 10.
(3) Lewis, N. S.; Nocera, D. G. *Proc. Natl. Acad. Sci. U. S. A.* **2006**, *103* (43), 15729.
(4) Styring, S. *Faraday Discuss.* **2012**, *155*, 357.
(5) Concepcion, J. J.; House, R. L.; Papanikolas, J. M.; Meyer, T. J. *Proc. Natl. Acad. Sci.* **2012**, *109* (39), 15560.
(6) Grätzel, M. *Nature* **2001**, *414* (6861), 338.
(7) Steinfeld, A. *Int. J. Hydrogen Energy* **2002**, *27* (6), 611.
(8) Ogden, J.; Williams, R. *Int. J. Hydrogen Energy* **1990**, *15* (3), 155.
(9) Ismail, A. A.; Bahnemann, D. W. *Sol. Energy Mater. Sol. Cells* **2014**, *128* (August), 85.
(10) Maeda, K.; Domen, K. *J. Phys. Chem. Lett.* **2010**, *1* (18), 2655.
(11) Ausfelder, F.; Beilmann, C.; Bertau, M.; Bräuninger, S.; Heinzel, A.; Hoer, R.; Koch, W.; Mahlendorf, F.; Metzelthin, A.; Peuckert, M.; Plass, L.; Räuchle, K.; Reuter, M.; Schaub, G.; Schiebahn, S.; Schwab, E.; Schüth, F.; Stolten, D.; Teßmer, G.; Wagemann, K.; Ziegahn, K.-F. *Chemie Ing. Tech.* **2015**, *87* (1-2), 17.
(12) Takanabe, K.; Domen, K. *ChemCatChem* **2012**, *4* (10), 1485.
(13) Scanlon, D. O.; Dunnill, C. W.; Buckeridge, J.; Shevlin, S. A; Logsdail, A. J.; Woodley, S. M.; Catlow, C. R. A; Powell, M. J.; Palgrave, R. G.; Parkin, I. P.; Watson, G. W.; Keal, T. W.; Sherwood, P.; Walsh, A.; Sokol, A. A. *Nat. Mater.* **2013**, *12* (9), 798.
(14) Reddy, K. M.; Manorama, S. V.; Reddy, A. R. *Mater. Chem. Phys.* **2003**, *78* (1), 239.
(15) Fujishima, A.; Honda, K. *Nature* **1972**, *238* (5358), 37.
(16) Chen, X.; Shen, S.; Guo, L.; Mao, S. S. *Chem. Rev.* **2010**, *110* (11), 6503.
(17) Lan, Y.; Lu, Y.; Ren, Z. *Nano Energy* **2013**, *2* (5), 1031.
(18) Pu, Y. C.; Wang, G.; Chang, K. Der; Ling, Y.; Lin, Y. K.; Fitzmorris, B. C.; Liu, C. M.; Lu, X.; Tong, Y.; Zhang, J. Z.; Hsu, Y. J.; Li, Y. *Nano Lett.* **2013**, *13* (8), 3817.

(19) Linic, S.; Christopher, P.; Ingram, D. B. *Nat. Mater.* **2011**, *10* (12), 911.
(20) Wang, C.; Astruc, D. *Chem. Soc. Rev.* **2014**, *43*, 7188.
(21) Furube, A.; Du, L.; Hara, K.; Katoh, R.; Tachiya, M. *J. Am. Chem. Soc.* **2007**, *129* (48), 14852.
(22) Youngblood, W. J.; Lee, S. A.; Maeda, K.; Mallouk, T. E. *Acc. Chem. Res.* **2009**, *42* (12), 1966.
(23) Yum, J.-H.; Chen, P.; Grätzel, M.; Nazeeruddin, M. K. *ChemSusChem* **2008**, *1* (8-9), 699.
(24) Warren, S. C.; Thimsen, E. *Energy Environ. Sci.* **2012**, *5* (1), 5133.
(25) Petryayeva, E.; Krull, U. J. *Anal. Chim. Acta* **2011**, *706* (1), 8.
(26) Noguez, C. *J. Phys. Chem. C* **2007**, *111* (10), 3806.
(27) Link, S.; El-Sayed, M. A. *Int. Rev. Phys. Chem.* **2000**, *19* (3), 409.
(28) Jain, P. K.; Lee, K. S.; El-Sayed, I. H.; El-Sayed, M. A. *J. Phys. Chem. B* **2006**, *110* (14), 7238.
(29) Garcia, M. A. *J. Phys. D. Appl. Phys.* **2012**, *45* (38), 389501.
(30) Yang, J.; Wang, D.; Han, H.; Li, C. *Acc. Chem. Res.* **2013**, *46* (8), 1900.
(31) Priebe, J. B.; Karnahl, M.; Junge, H.; Beller, M.; Hollmann, D.; Brückner, A. *Angew. Chemie - Int. Ed.* **2013**, *52*, 11420.
(32) Gärtner, F.; Losse, S.; Boddien, A.; Pohl, M.-M.; Denurra, S.; Junge, H.; Beller, M. *ChemSusChem* **2012**, *5* (3), 530.
(33) Priebe, J. B.; Radnik, J.; Lennox, A. J. J.; Pohl, M.; Karnahl, M.; Grabow, K.; Bentrup, U.; Junge, H.; Beller, M.; Brückner, A. *ACS Catalysis* **2015,** *5, 2137*.
(34) Ni, M.; Leung, M. K. H.; Leung, D. Y. C.; Sumathy, K. *Renew. Sustain. Energy Rev.* **2007**, *11* (3), 401.
(35) Kruth, A.; Peglow, S.; Quade, A.; Pohl, M.-M.; Weltmann, K.-D. *J. Phys. Chem. C* **2014**, *118*, 25234.
(36) Peglow, S.; Pohl, M.-M.; Kruth, A.; Brüser, V. *J. Phys. Chem. C* **2015**, *119*, 563.
(37) Zhang, H.; Haba, M.; Okumura, M.; Akita, T.; Hashimoto, S.; Toshima, N. *Langmuir* **2013**, *29* (33), 10330.
(38) Jiang, H.; Akita, T.; Ishida, T. *J. Am. Chem. Soc.* **2011**, *133*, 1304.
(39) Wulff, H. *Introduction to Complex Plasmas*; Bonitz, M., Horing, N., Ludwig, P., Eds.; Springer, 2010.
(40) Strecker, A.; Salzberger, U.; Mayer, J. *Prakt. Metallogr.* **1993**, *30* (10), 482.
(41) Jette, E. R.; Foote, F. *J. Chem. Phys.* **1935**, *3* (10), 605.
(42) Kruth, A.; Quade, A.; Brüser, V.; Weltmann, K.-D. *J. Phys. Chem. C* **2013**, *117* (8), 3804.
(43) Claus, P.; Brücker, a.; Mohr, C.; Hofmeister, H. *J. Am. Chem. Soc.* **2000**, *122* (7), 11430.
(44) Söderlund, J.; Kiss, L.; Niklasson, G.; Granqvist, C. *Phys. Rev. Lett.* **1998**, *80* (11), 2386.
(45) Robson, J. D. *Mater. Sci. Technol.* **2004**, *20* (4), 441.
(46) Cleveland, C.; Luedtke, W.; Landman, U. *Phys. Rev. Lett.* **1998**, *81* (10), 2036.
(47) Marks, L. D. *Reports Prog. Phys.* **1999**, *57* (6), 603.
(48) Nam, H.-S.; Hwang, N.; Yu, B.; Yoon, J.-K. *Phys. Rev. Lett.* **2002**, *89* (27), 1.
(49) Ascencio, J. A.; Gutiérrez-Wing, C.; Espinosa, M. E.; Marín, M.; Tehuacanero, S.; Zorrilla, C.; José-Yacamán, M. *Surf. Sci.* **1998**, *396* (1-3), 349.

(50) Barnard, A. S. *J. Phys. Chem. B* **2006**, *110* (48), 24498.
(51) Hubenthal, F.; Ziegler, T.; Hendrich, C.; Alschinger, M.; Träger, F. *Eur. Phys. J. D* **2005**, *34* (1-3), 165.
(52) Douglas, F.; Yañez, R.; Ros, J.; Marín, S.; De La Escosura-Muñiz, A.; Alegret, S.; Merkoçi, A. *J. Nanoparticle Res.* **2008**, *10*, 97.
(53) Shyjumon, I.; Gopinadhan, M.; Ivanova, O.; Quaas, M.; Wulff, H.; Helm, C. a.; Hippler, R. *Eur. Phys. J. D* **2006**, *37* (3), 409.
(54) Buffat, P.; Borel, J.-P. *Phys. Rev. A* **1976**, *13* (6), 2287.
(55) Banfield, J. F.; Welch, S. A; Zhang, H.; Ebert, T. T.; Penn, R. L. *Science* **2000**, *289* (5480), 751.
(56) Zhang, Q.; Liu, S.-J.; Yu, S.-H. *J. Mater. Chem.* **2009**, *19* (2), 191.
(57) Fan, F. R.; Liu, D. Y.; Wu, Y. F.; Duan, S.; Xie, Z. X.; Jiang, Z. Y.; Tian, Z. Q. *J. Am. Chem. Soc.* **2008**, *130* (22), 6949.
(58) Tsuji, M.; Yamaguchi, D.; Matsunaga, M.; Alam, M. J. *Cryst. Growth Des.* **2010**, *10* (12), 5129.
(59) Skriver, H. L.; Rosengaard, N. M. *Phys. Rev. B* **1992**, *46* (11), 7157.
(60) Jain, P. K.; El-Sayed, M. A. *Chem. Phys. Lett.* **2010**, *487* (4-6), 153.
(61) Hartland, G. V. *Chem. Rev.* **2011**, *111*, 3858.
(62) Huang, X.; El-Sayed, M. A. *J. Adv. Res.* **2010**, *1* (1), 13.
(63) Hayashi, S.; Okamoto, T. *J. Phys. D. Appl. Phys.* **2012**, *45* (43), 433001.
(64) Stockman, M. I. *Phys. Today* **2011**, February Issue, 39.
(65) Heo, C. H.; Lee, S.-B.; Boo, J.-H. *Thin Solid Films* **2005**, *475* (1-2), 183.
(66) Priebe, J. B.; Radnik, J.; Lennox, A. J. J.; Pohl, M.-M.; Karnahl, M.; Hollmann, D.; Grabow, K.; Bentrup, U.; Junge, H.; Beller, M.; Brückner, A. *ACS Catal.* **2015**, *5*, 2137.
(67) Silva, C. G.; Juárez, R.; Marino, T.; Molinari, R.; García, H. *J. Am. Chem. Soc.* **2011**, *133* (22), 595.
(68) Brandon, N. P.; Kelsall, G. H. *J. Appl. Electrochem.* **1985**, *15*, 475.
(69) Vogt, H.; Balzer, R. J. *Electrochim. Acta* **2005**, *50* (10), 2073.

5. Improvement of Hematite Photoanodes by Sn-Doping

This chapter is based on the following publication:

"Tin Doping Speeds Up Hole Transfer During Light-Driven Water Oxidation at Hematite Photoanodes" by Halina K. Dunn, Johann M. Feckl, Alexander Müller, Dina Fattakhova-Rohlfing, Samuel G. Morehead, Julian Roos, Laurence M. Peter, Christina Scheu, and Thomas Bein, which was published in Physical Chemistry Chemical Physics 16, 24610 (2014).

5.1. Introduction

The photoelectrochemical splitting of water into hydrogen and oxygen under solar irradiation holds the promise of providing a vital fuel for a future low-carbon energy economy. In order to reach competitive efficiencies for hydrogen production, tandem cell architectures will be required.[1] Tandem photoelectrolysis cells can either use a wide bandgap semiconductor photoelectrode such as α-Fe_2O_3 (hematite) connected in optical series to a low-cost solar cell that absorbs the longer wavelength component of the solar spectrum,[2-5] or alternatively two semiconductor photoelectrodes can be used, one n-type and one p-type.[6] Regardless of which of these designs ultimately proves to be the most effective, research into semiconductor materials able to perform one of the half-reactions in water splitting must be targeted to surmount the obstacles that currently limit the performance of light-driven water splitting systems.

Chemical stability, abundance, visible light absorption and suitable valence band energy make hematite a promising n-type material for the light-driven oxygen evolution reaction (OER). However, its relatively weak absorbance at longer wavelengths (due to its indirect bandgap) and poor hole-mobility lead to an inherent trade-off between sufficient light absorption and carrier collection. Nano-structuring of the photoanode offers an elegant solution to this issue by decoupling the hole collection depth from the light absorption depth.[7,8] Vapour-phase deposition techniques and spray pyrolysis have been used to produce high surface area hematite electrodes that generate up to 1.8 mA cm^{-2} at the reversible oxygen reduction potential (1.23 V vs. RHE) under AM 1.5 irradiation in a basic medium without application of a catalyst.[9-11] Very recently, wormlike nanostructured hematite electrodes have achieved current densities exceeding 4.3 mA cm^{-2}, corresponding to around one third of the theoretical limit set by the band gap of the oxide.[12]

On a fundamental level, the performance of hematite photoanodes is primarily limited by the sluggish kinetics of the multistep (4-electron) oxygen evolution reaction (OER). This kinetic bottle-neck leads to a large build-up of photogenerated holes that are vulnerable to

recombination with electrons, lowering the efficiency of hole-transfer to the solution phase. Speeding up the interfacial hole transfer reactions by catalysis is therefore an attractive route to improve the overall efficiency of hematite photoanodes, with IrO_2 and various cobalt species showing promise as OER catalysts.[13-15] However, suppression of surface recombination is equally important, and in some cases at least, the adsorption of cobalt species evidently improves the performance of hematite by inhibiting recombination rather than by catalysing the charge transfer reaction.[16,17]

Doping of hematite with additives such as Sn,[18-22] Si,[9,10,23-25] Ti,[18,26-30] Pt,[31,32] Cr,[33] Mo,[33] Zn[34] and I,[35] has proven to be a successful strategy to enhance the performance of hematite for the light-driven OER. Several studies have attributed the effect of such dopants to changes in bulk hematite properties such as conductivity,[11,18,19,21,23,25,26,36] or crystallinity.[9] Few of these studies have considered what other possible beneficial roles dopant atoms may play in the processes that are involved in light-driven oxygen evolution. A more quantitative approach to interpreting the role of dopants is to analyse in detail the photoelectrochemical (PEC) behaviour of the photoanode under water oxidation conditions. For example, comparison of the wavelength dependence of the photocurrent response for illumination from the electrolyte and the substrate sides has been used to identify improvements in electron collection caused by doping.[11,26,35] By contrast, a reduction of electron-hole recombination brought about by Pt-doping of hematite was deduced from the dependence of photocurrent on light intensity, which was changed from square root to linear by Pt-doping.[31] In another quantitative study, investigation of the thickness-dependence of the photocurrent response of Ti-doped hematite grown by atomic layer deposition revealed that doping reduced losses arising from electron-hole recombination at the fluorine doped tin oxide (FTO) hematite interface (the so-called "dead layer effect").[37] Finally, Chemelewski *et al.* compared the photocurrent from Si-doped hematite in the presence and absence of a hole scavenger and concluded that the efficiency of interfacial hole transfer improved upon doping.[24] However, none of these studies used dynamic methods to obtain values of the rate constants that are directly relevant to photoanode performance. In the present work, we show that analysis of the transient and periodic photocurrent responses can be used to distinguish between the effects of catalysis and inhibition of surface recombination in the case of Sn doped hematite electrodes.

Several theoretical studies have predicted that foreign metal atoms located at the hematite surface should influence the intermediate steps of the OER. By applying *ab initio* density functional theory (DFT + U) calculations to fully hydroxylated hematite (0001) surfaces, Liao *et al.* predicted the overpotential for the OER on doped hematite by calculating the minimum applied potential resulting in all intermediate steps proceeding spontaneously. They found that replacing Fe sites with other transition metals altered the relative binding energies of the O, OH and OOH reactive species, which in turn affected the overpotential, which was predicted to decrease if Ni or Co were used.[38] Similarly, Busch *et al.*[39] considered the energetics of the reaction from adsorbed hydroxides to oxygen via a μ-peroxo bridge and found the reaction should proceed more favourably at certain bi-nuclear transition metal

sites, such as Fe-Co. These theoretical insights, along with the need to find effective catalysts for the OER on hematite, motivated us to take a deeper look at the role of surface properties in determining the performance of Sn-doped hematite electrodes for light-driven OER.

In practice, one of the most widely encountered effects of doping of hematite layers is a modification of the nanostructure morphology, leading in many cases to a reduction in feature size and thus to an increase in surface area.[9,11,19,21-23,27,30,33,40] Although this effect may be partly responsible for the reported performance improvement, it complicates the task of uncovering other possible roles played by the dopant atoms. In order to circumvent this problem, we have developed a simple solution-processed route to fabricate model systems in which up to 3.2 atomic % Sn can be incorporated into thin nanostructured hematite films with only minimal morphological change. The films are about 50 nm thick, and produce 0.06 mA cm^{-2} at 1.23 V vs. RHE under AM 1.5 illumination. The extremely thin nature of these films leads to a low light harvesting efficiency, and consequently modest performance. However, they make good model systems because their *internal* quantum efficiency (IQE) under standard conditions is comparable to that of benchmark hematite prepared by atmospheric pressure chemical vapour phase deposition, APCVD,[41] (see supporting information for details).

In the present study, the transient photocurrent responses of the hematite electrodes to chopped illumination were analysed in order to assess the efficiency of interfacial hole-transfer during light-driven OER. The results revealed that the incorporation of tin into the hematite films improves the efficiency of hole-transfer in the light-driven OER. In principle, such an improvement could either be explained by a higher rate constant for the transfer of holes across the interface or by suppression of surface electron-hole recombination. The rate constants for surface recombination and charge transfer were deconvoluted using intensity-modulated photocurrent spectroscopy, IMPS, which showed that Sn-inclusion increases the rate constant for hole-transfer by more than an order of magnitude. The material composition was characterized by analytical transmission electron microscopy (TEM), which probes the degree of Sn-incorporation in the bulk of the hematite crystallites and provides insights into the spatial distribution of Sn. It emerged that Sn-atoms preferentially occupy sites located at the surface of the hematite nanoparticles, resulting in a core-shell structure. The results of the study therefore clearly link the surface-specific enrichment of Sn in the hematite nanocrystals with catalysis of the light-driven OER.

5.2. Theory

The external quantum efficiency, EQE(λ), of light-driven water oxidation taking place at bulk semiconductor electrolyte junctions depends on the product of the efficiencies of light harvesting, $\eta_{LH}(\lambda)$, charge separation, $\eta_{sep}(\lambda)$, and hole-transfer, η_{trans}, to the electrolyte, the first two being functions of the light wavelength, λ.

$$EQE(\lambda) = \eta_{LH}(\lambda)\eta_{sep}(\lambda)\eta_{trans} \quad (1)$$

Equation (1) will also apply to nanostructured electrodes provided that the width of the space charge region, W_{sc}, is smaller than the feature size of the structure. As shown below, this is the case for the hematite electrodes studied here. In the absence of light scattering, the light harvesting efficiency can be calculated from the wavelength-dependent absorption coefficient, $\alpha(\lambda)$, and the film thickness, d.

$$\eta_{LH}(\lambda) = 1 - e^{-\alpha(\lambda)d} \qquad (2)$$

For a planar electrode geometry, the electron-hole separation efficiency $\eta_{sep}(\lambda)$ can be calculated using the Gärtner equation[42] (see below) if the width of the space charge region, W_{sc}, and the hole diffusion length, L_p, are known. However, this calculation will not be correct if substantial recombination takes place in the space charge region (in which case η_{sep} is lower) or if the electrode is nanostructured (see supporting information). For this reason, we derive $\eta_{sep}(\lambda)$ from the external quantum efficiency using the light harvesting efficiency calculated from the absorption spectrum and the transfer efficiencies derived from photocurrent transient measurements or IMPS.

Hematite photo-anodes respond to chopped illumination with a characteristic "spike and overshoot" photocurrent transient.[43-45] This transient response is typical for systems with a large degree of surface electron-hole recombination.[17,45] When the light is switched on, holes generated in the space charge region are swept rapidly towards the semiconductor electrolyte junction. Due to the slow kinetics of the 4-hole oxidation of water to molecular oxygen, the concentration of holes builds up considerably at the interface until the rate of arrival of holes is balanced in the steady state by the rates of charge transfer and recombination. Since surface recombination leads to a flux of electrons towards the surface, the resulting photocurrent transient is the sum of the hole and electron contributions. The instantaneous photocurrent measured when the illumination is switched on corresponds to a charging or displacement current due to the initial movement of photo-generated holes towards the surface. By contrast, the steady-state photocurrent corresponds to the flux of holes that are transferred successfully to the electrolyte without undergoing recombination with electrons at the surface. It follows that the ratio of the steady state photocurrent to the instantaneous photocurrent, $j_{ss}/j_{(t=0)}$, is a measure of the efficiency of hole-transfer from the electrode to the electrolyte. This situation has been modelled in terms of the surface concentration of holes using a simple phenomenological approach.[46,47] Assuming that both hole transfer and recombination are pseudo-first order in the surface hole concentration, the transfer efficiency can also be expressed in terms of the phenomenological first order rate constants of hole transfer, k_{trans}, and recombination, k_{rec}.

$$\eta_{trans} = \frac{j_{ss}}{j_{t=0}} = \frac{k_{trans}}{k_{trans} + k_{rec}} \qquad (3)$$

An example of the type of predicted transient photocurrent response is shown in Figure 5-.

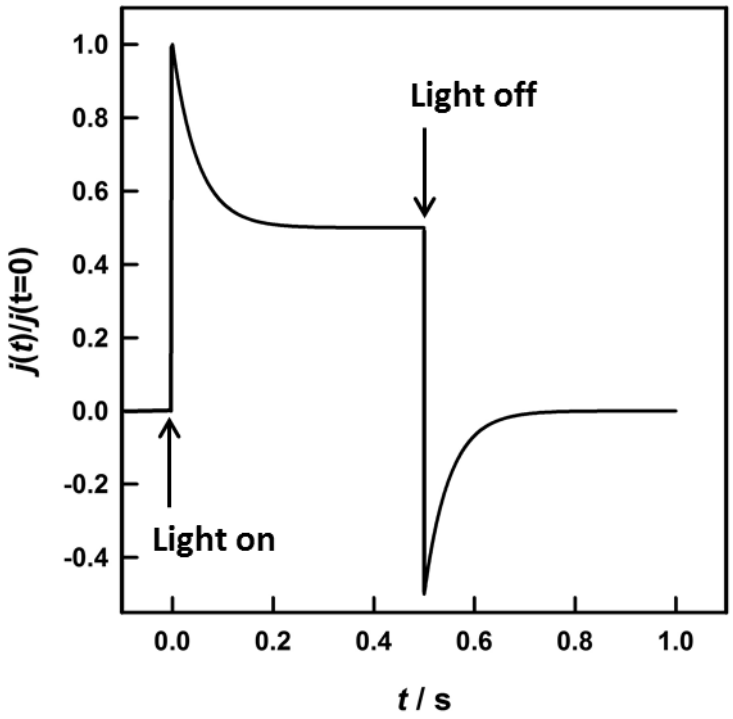

Figure 5-1. Normalized transient photocurrent response calculated for $k_{tr} = k_{rec} = 10\ s^{-1}$. The decay time constant in this case is $(k_{rec} + k_{tr})^{-1} = 50$ ms and the hole transfer efficiency = $k_{tr}/(k_{tr} + k_{rec}) = 0.5$, so that the steady state current is half of the instantaneous current.

In principle, the exponential decay of the current towards the steady state, which is characterized by the time constant $(k_{trans} + k_{rec})^{-1}$, can be analysed, and then k_{trans} and k_{rec} can be separated using equation (3). In practice, however, it is more convenient to determine the time constant using small amplitude frequency-resolved measurements such as IMPS[17] or photoelectrochemical impedance spectroscopy (PEIS).[48] The IMPS method involves small amplitude (< 10%) variable frequency sinusoidal modulations of the light intensity about a dc value. The resulting phase and amplitude of the photocurrent are recorded as a function of frequency, and the results are displayed in the complex plane.[49,50] The imaginary component of the photocurrent reaches a maximum when the frequency, ω_{max}, matches the characteristic relaxation constant of the system, *i.e.* the same time constant $(k_{trans} + k_{rec})^{-1}$ seen in the exponential decay of the transient photocurrent.

$$\omega_{\max} = k_{trans} + k_{rec} \qquad (4)$$

The high and low frequency intercepts of the IMPS response in the complex plane correspond respectively to the instantaneous and steady state photocurrents seen in Figure 5-1, and their ratio is therefore given by equation (3). The main advantage of the IMPS technique is that it involves a small amplitude modulation, so that changes in band bending induced by illumination are minimized (the effect on the IMPS response of light-induced modulation of band bending has been considered elsewhere[51]). By contrast, large changes in band bending may occur with chopped illumination (this probably explains the lack of symmetry between

transient 'on' and 'off' responses in Figure 5-a). The IMPS response is also attenuated by the RC time constant determined by the product of the series resistance, R_{series}, and the space charge capacitance, C_{sc}. This attenuation gives rise to a high semicircle in the opposite quadrant with a maximum circular frequency equal to the product $R_{series}C_{sc}$, which allows estimation of the space charge capacitance, C_{sc}, if the series resistance is known. An example of the IMPS response predicted for the same values of k_{trans} and k_{rec} as those used for the transient in Figure 5-1 is shown in Figure 5-2.

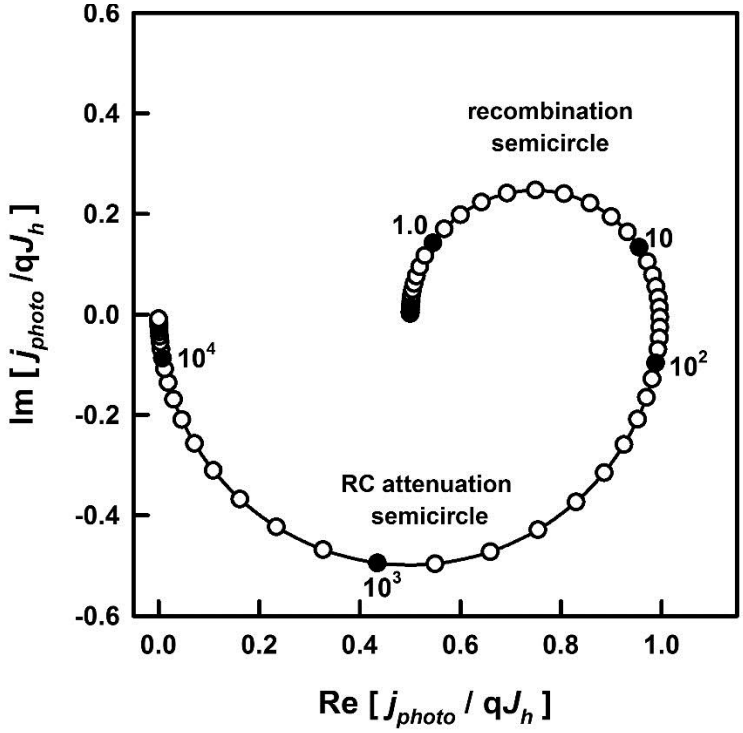

Figure 5-2. IMPS response predicted for $k_{rec} = k_{trans} = 10\ s^{-1}$, $C_{sc} = 1\ \mu F\ cm^{-2}$, $R_{ser} = 20\ \Omega$. The response is normalized to the hole current, qJ_h, generated by collection of holes in the space charge region. The radial frequency corresponding to the maximum of the upper recombination semicircle is equal to $k_{trans} + k_{rec}$, and the normalized low frequency intercept is equal to $k_{trans}/(k_{trans} + k_{rec})$, which corresponds to the ratio of the steady state current to the instantaneous current in Figure 5-1.

As noted above, this interpretation of photocurrent transients and IMPS is valid for semiconductors with a well-defined depletion layer at the interface with the electrolyte. To be applicable to structured semiconductors, such as those studied here, W_{SC} should be smaller than the average feature size. One method to determine the width of the depletion region is through the measurement of the electrode capacitance. The flat band potential, V_{fb}, and donor density, N_d, derived from the Mott Schottky relationship (equation (5)), are then used to calculate values of W_{SC} as a function of applied potential (equation (6)), where ε_r is the relative permittivity, ε_0 is the permittivity of free space, A is the electrode area, V is the applied potential, q is the elementary charge, k_B is Boltzmann's constant and T is the temperature.

$$\frac{1}{C_{sc}^2} = \frac{2}{\varepsilon_r \varepsilon_0 N_d A^2}\left[\left(V - V_{fb}\right) - \frac{k_B T}{q}\right] \quad (5)$$

$$W_{sc} = \left(\frac{2\left(V - V_{fb}\right)\varepsilon_r \varepsilon_0}{qN_d}\right)^{1/2} \quad (6)$$

Another method to estimate the width of the space charge layer in illuminated semiconductor electrolyte junctions under reverse bias involves using the Gärtner equation.[42] This equation applies if holes are consumed so rapidly at the interface that there are no recombination losses (this is the case if a fast redox system is used to capture holes). For materials with very small hole-diffusion lengths, L_p, such as hematite, only carriers generated in the space charge layer contribute to the photocurrent, simplifying the Gärtner expression.

$$EQE(\lambda) = 1 - \frac{e^{-\alpha(\lambda)W_{sc}}}{1 + \alpha(\lambda)L_p} \approx 1 - e^{-\alpha(\lambda)W_{sc}} \quad (7)$$

However, in the case of the light driven OER, some fraction of the holes reaching the surface is lost by surface recombination so that the *EQE* is lower than predicted by equation (7). If we take the non-unity transfer efficiency into account, the simplified Gärtner equation can be rearranged to give the width of the space charge region.

$$W_{sc} = -\frac{1}{\alpha(\lambda)}\ln\left(1 - \frac{EQE}{\eta_{trans}}\right) \quad (8)$$

5.3. Materials and Methods

5.3.1. Synthesis Route for the Incorporation of Sn into Mesoporous Hematite Electrodes

Hematite precursor solutions were prepared according to the following procedure. 0.630 g (1.56 mmol) $Fe(NO_3)_3 \cdot 9\,H_2O$ was dissolved in a solution of the block copolymer Pluronic P123 (0.25 g) in 10 mL *tert*-butanol under sonication for 15 minutes. 2.5 mL water (Millipore) was then added, forming a dark red solution. The solution was stirred at room temperature overnight resulting in a light brown dispersion of iron oxide (Fe_2O_3). The synthesis is a development of the protocol described by Redel *et al.*.[52] However, these authors did not use any surfactant, and their synthesis led to formation of a two-phase mixture of hematite and maghemite, in the ratio of 65:35. By contrast, addition of the surfactant yields phase-pure hematite.

For the preparation of the Sn-containing hematite, $Sn(OAc)_4$ was added to the solution described above, see Table 1 in the supporting information for further details. The desired amounts of $Sn(OAc)_4$ were first dispersed under vigorous stirring for 5 h followed by 15 min sonication in the above mixture of Pluronic P123 and *tert*-butanol. The remaining steps of the

synthesis then followed those described above for pure hematite. It is important to note that throughout the following text, the Sn:Fe-ratio refers to the atomic ratio of the two elements *in the precursor solutions*, unless stated otherwise.

After cleaning the FTO glass (Pilkington TEC 15 Glass™, 2.5 × 1.5 cm) by sequential sonication for 15 min each in detergent (1 mL Extran in 50 mL Millipore water), water (Millipore) and ethanol, the substrates were dried and masked with Scotch Tape on the conducting side to retain a non-covered area of 1.5 × 1.5 cm. The backs of the substrates were completely masked to avoid contamination during the spin-coating procedure.

Before spin-coating, the fresh solutions were filtered through a 220 nm syringe filter (Sartorius Minisart cellulose acetate membrane) to remove agglomerates, ensuring the preparation of homogeneously smooth films. The masked substrates were covered with 100 µL of solution and spun at 1000 rpm for 30 seconds. To remove the surfactant and crystallize the material, the samples were calcined in air in a laboratory oven (3 hour ramp to 600 °C, 30 min dwell time), resulting in films of about 50 nm thickness. To obtain thicker films, the films were dried for 5 minutes at 60 °C and the spin-coating step was repeated. Powders for X-ray diffraction (XRD) and TEM analysis were obtained by scraping material off the substrate with a razor blade.

5.3.2. Thin Film Characterization

XRD measurements were performed on a STOE powder diffractometer in transmission geometry (Cu-Kα_1, λ = 1.5406 Å) equipped with a position-sensitive Mythen-1K detector. Scanning electron microscopy (SEM) was performed on a JEOL JSM-6500F scanning electron microscope equipped with a field emission gun. Material was scraped from the substrate, and deposited on a copper grid with a carbon film for TEM analysis. The analysis was carried out on a FEI Titan 80-300 (S)TEM with a Fischione Instruments (Model 3000) high angle annular dark field (HAADF) detector and an EDAX energy-dispersive X-ray spectroscopy (EDX) detector. All measurements were conducted at an acceleration voltage of 300 kV.

The UV-visible transmission and reflection of the mesoporous thin films on FTO-coated glass substrates was measured with a Perkin Elmer Lambda 1050 UV/Visible/NIR spectrophotometer equipped with an integrating sphere. For transmission measurements, the sample was placed directly outside the integrating sphere with the film facing inwards, and for reflection measurements, the sample was placed directly after the integrating sphere with the glass substrate facing the incoming beam. The Naperian absorbance spectra of the hematite layers Abs_H were calculated from the wavelength dependent transmission of the FTO substrate and hematite-coated substrate, T_S and T_{S+H}, respectively, and reflection of the substrate and hematite coated sample, R_S and R_{S+H}, according to the following formula, which is derived in reference[53].

$$Abs_H = \ln\left(\frac{T_{S+H} / T_S}{1 - \frac{R_{S+H} - R_S}{T_S^2}}\right) \quad (9)$$

5.3.3. Photoelectrochemical Characterization

Hematite photoelectrodes were masked with a PTFE-coated glass fiber adhesive tape leaving a circular area of 1 cm in diameter exposed to a 0.1 M NaOH aqueous electrolyte. Electrochemical measurements were carried out in a cubic glass cell using a μ-Autolab III potentiostat (Metrohm) equipped with an FRA 2 impedance analyser connected to a saturated Ag/AgCl reference electrode (Sigma Aldrich, 0.197 V *vs.* SHE) and a Pt mesh counter electrode. Electrode potentials versus the reversible hydrogen electrode, V_{RHE}, were calculated from those measured at pH 13 versus the Ag/AgCl electrode, $V_{Ag/AgCl}$, according to

$$\left(\frac{V_{RHE} - V_{Ag/AgCl}}{V}\right) = 0.197 + 0.059\,pH \quad (10)$$

The light intensity was measured at the position of the electrode inside the cell using a 4 mm^2 photodiode, which had been calibrated against a certified Fraunhofer ISE silicon reference cell equipped with a KG5 filter.

The current-voltage characteristics of the films were obtained by scanning from negative to positive potentials in the dark or under illumination with a 20 mV s^{-1} sweep rate. Illumination, provided either by a high-power light emitting diode (LED, Thorlabs, 455 nm) or by a solar simulator (AM1.5G. Solar Light Model 16S) at 100 mW cm^{-2}, was incident through the FTO-coated glass substrate. For external quantum efficiency (EQE) measurements, chopped monochromatic light (chopping frequency 2 Hz) was provided by a 150 W xenon lamp in combination with a monochromator and order-sorting filters. The cell was biased close to 1.2 V *vs*. RHE under simulated solar irradiation to ensure realistic operating conditions. The current recorded by the Autolab potentiostat was output to a lock-in amplifier synchronized to the chopper frequency.

Photocurrent transients were used to estimate the transfer efficiency of holes to the solution phase.[17] The high power light emitting diode, LED, was switched on and off every 500 ms. The hematite electrodes were held at a given potential, and the transient current was sampled at 0.1 ms intervals. This fast sampling allowed the instantaneous current to be determined. In cases where the current transient had not reached a steady state value after 500 ms, additional photocurrent transients were recorded with 5 s on/off times, sampled at 1 ms intervals. Electrochemical impedance spectroscopy (EIS) was carried out in the dark at applied potentials at which no significant dark current flows (between 0.75 and 1.5 V vs RHE), and the potential was modulated by 10 mV at frequencies ranging logarithmically from 100 kHz to

1 Hz. Intensity modulated photocurrent spectroscopy (IMPS) was carried out using a PGSTAT302N Autolab (Metrohm), equipped with an FRA32M frequency response analyser, connected to an LED driver kit which powered a 470 nm high-power LED. The light intensity was modulated by 10 % between 100 kHz and 0.1 Hz.

5.4. Results and Discussion

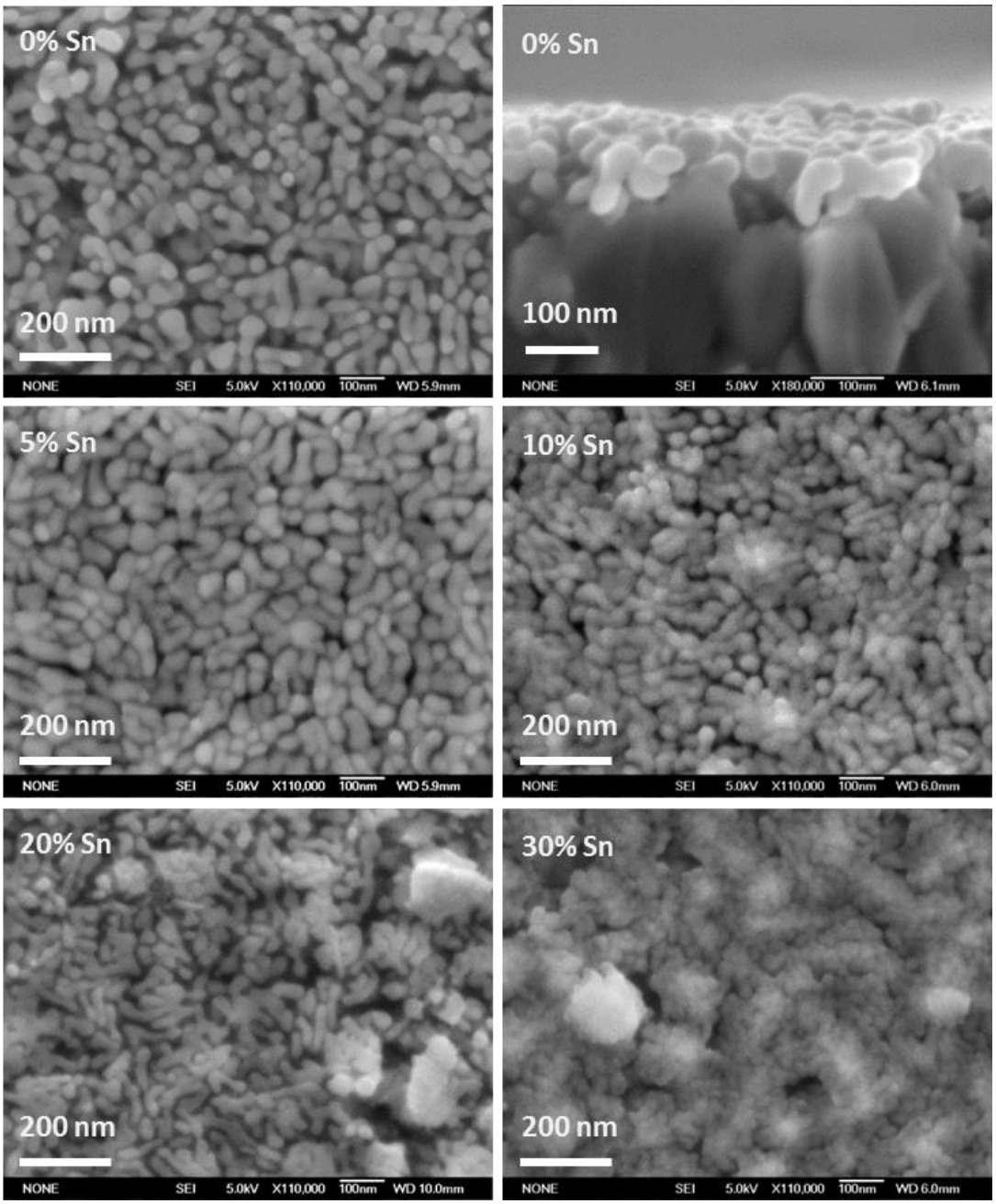

Figure 5-3. Top view and cross section SEM images of undoped hematite films (top). Top view SEM-image of films prepared with 5 %, 10 %, 20 % and 30 % Sn-precursor in the hematite synthesis. Each item is labelled with the appropriate Sn-precursor percentage, all films are on an FTO coated glass substrate.

Figure 5-3 gives an overview of the impact of Sn-doping on the film morphology. The SEM top view images show a disordered mesoporous "worm-like" structure for films prepared with up to 20 % Sn-precursor, similar to that seen for various hematite films prepared by other solution-based synthetic routes.[19,21,22,54,55] The morphology remains unchanged up to the addition of 10 % Sn-precursor to the hematite synthesis, with a mean particle size of approximately 35 x 80 nm. When 20 % Sn-precursor is added to the synthesis, the mean feature size decreases somewhat (to *ca.* 30 x 70 nm), and the addition of 30 % Sn-precursor leads to a more compact and less well defined morphology. The cross section SEM view indicates that the film is approximately made up of a monolayer of "worm-like" particles. The roughness factor of the films, of the order of 2.5 was estimated from this description of the morphology, see the supporting information.

Figure 5-4 compares the steady state current-voltage characteristics of films prepared from precursors containing 0 % Sn, 5 % Sn, 10 % Sn, 20 % Sn and 30 % Sn. In the case of the pure hematite film, the photocurrent density is very low. For films prepared using precursor solutions with a Sn-content above 5 %, the photocurrent increases substantially, reaching a maximum for the 20 % Sn film. The drop in photocurrent observed for the 30 % Sn film is accompanied by a significant change in morphology, see Figure 5-. While the smaller feature size of the 20 % Sn sample may contribute to the higher photocurrent, this cannot be the dominant factor, because even at 5 % Sn-precursor, the rise in photocurrent is substantial, although the feature size does not change. The goal of this study was to determine the role played by Sn-doping in improving the PEC performance of hematite during water oxidation. Under standard operating conditions, these films have an IQE of the order of 3 %, in close agreement to the IQE of benchmark Si-doped hematite films prepared by APCVD,[41] see the supporting information for the full analysis. We therefore conclude that these films are suitable model systems for this study.

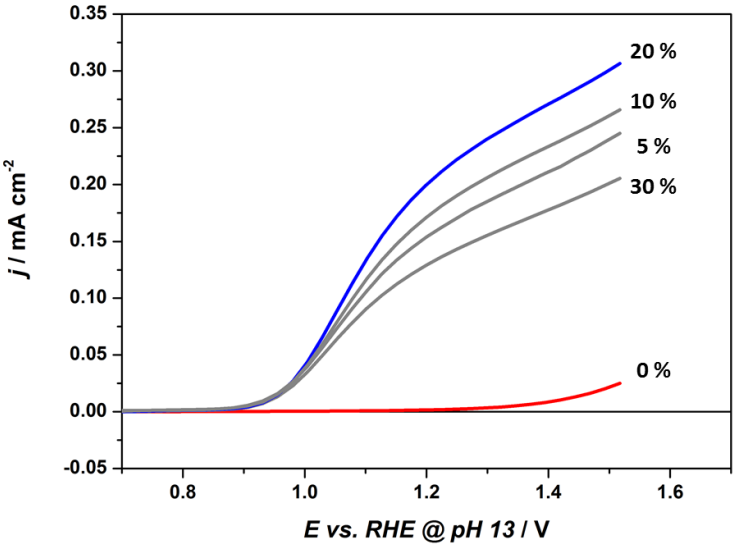

Figure 5-4. Current-voltage curves for single layers of mesoporous hematite prepared with 0 %, 5 %, 10 %, 20 % and 30 % Sn-precursor added to the synthesis. Electrolyte: 0.1 M NaOH. Illumination was

through the substrate. λ = 455 nm, incident photon flux = 10^{17} cm^{-2} s^{-1}. In all cases, the dark current was negligible over the potential range (see Figure SI 5-1 for dark current voltage curves).

In order to elucidate the role of Sn-incorporation in our system, photocurrent transients were recorded, as illustrated in Figure 5-a. In order to ensure that the theoretical treatment outlined above is applicable, the condition that the depletion layer should be narrower than the nanostructure feature size was tested; see supporting information for the full experimental details. Calculation of the width of the space charge region requires knowledge of the relative permittivity, ε_r, of hematite. Values of the relative permittivity of hematite in the literature vary enormously. For example Glasscock *et al.*[56] measured values of ε_r between 31 and 57, whereas Lunt *et al.*[57] have recently calculated values between 7.6 and 26.4 for different crystal orientations and a mean value of around 25 using DFT. At 1.2 V vs. RHE, values of W_{SC} obtained from the Mott-Schottky analysis for the 20 % sample in the dark ranged from 10 to 25 nm for values of relative permittivity of 25 and 57, respectively. By contrast, analysis of the EQE data using equation (8) indicated much smaller values of the space charge layer in the range of a few nm (see supporting information for details). This reduction of band bending (and hence a lower value of W_{sc}) under illumination could arise from the build-up of a positive surface charge associated with free or trapped holes, which results in more potential being dropped across the Helmholtz layer rather than across the depletion layer. It follows that - under illumination at least - the condition of a well-defined depletion layer with W_{sc} smaller than the feature size ($\geq$ 30 nm) should be satisfied. This reduction in W_{sc} under illumination highlights why small amplitude perturbation methods such as IMPS are preferable to large amplitude ones such as photocurrent transients.

The photocurrent transients shown in Figure 5-5a clearly indicate that almost all holes reaching the surface of the 0 % Sn sample recombine, leading to a negligible steady state photocurrent. Upon addition of only 5 % Sn-precursor to the hematite synthesis, both the instantaneous and steady state current densities increase significantly. Since $j_{(t=0)}$ corresponds to the flux of holes swept to the surface upon illumination, an increase in its value may indicate that the "bulk" properties of the material improve, perhaps due to a reduction in space charge recombination losses. Interestingly, $j_{(t=0)}$ decreases with further addition of Sn. This is most pronounced for the 30 % Sn doped sample, which has a significantly less well-defined morphology compared to the rest of the series, see Figure 5-4. The slight decrease in $j_{(t=0)}$ for the 20 % sample can also be correlated to a similarly small decrease in feature size, although it is not clear at present whether these observations are directly related.

Most remarkably, the transfer efficiencies, obtained from the ratio $j_{ss}/j_{(t=0)}$ according to equation (3), increase steadily with increasing Sn content, see Figure 5-5b. The increased transfer efficiency brought about by the incorporation of tin into the hematite can be explained in terms of the competition between interfacial transfer of holes taking part in the OER, and electron-hole recombination at the surface, see equation (3). On the one hand, the transfer efficiency can be improved by increasing the rate of hole transfer across the interface,

the kinetics of which are known to be very slow at hematite photoanodes.[58] On the other hand, given the slow transfer kinetics mentioned above, surface electron-hole recombination is very detrimental to the transfer efficiency, so that suppression of surface recombination significantly enhances performance.[16,17] The objective of the present study was to distinguish clearly between these two possibilities.

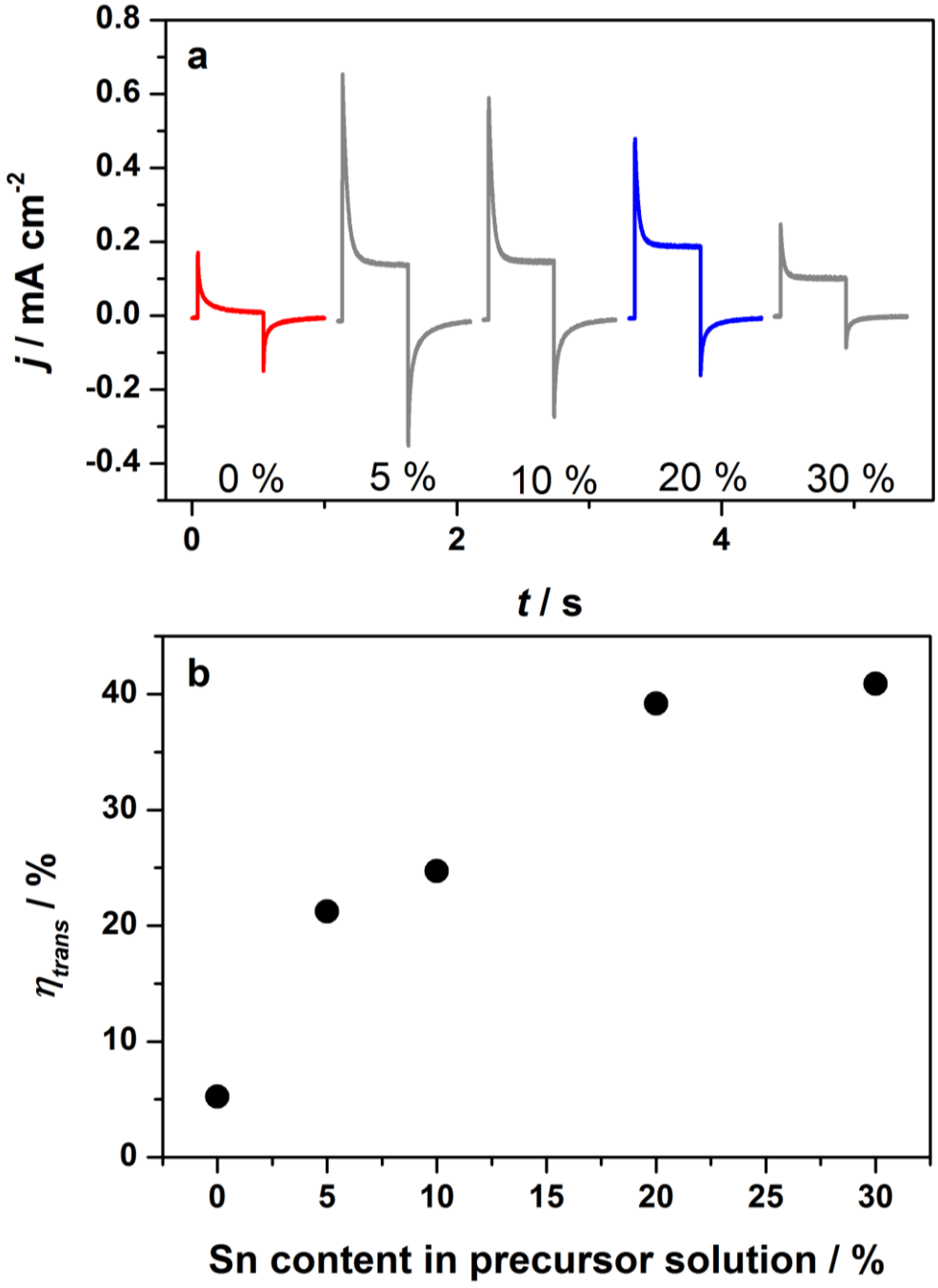

Figure 5-5. a) Photocurrent transients of hematite films prepared with 0 %, 5 %, 10 %, 20 % and 30 % Sn precursor in the synthesis. Measured at 1.164 V vs. RHE under 455 nm illumination, incident photon flux 10^{17} $cm^{-2}s^{-1}$. b) Transfer efficiency calculated from the photocurrent transients according to equation (3).

Although the analysis of photocurrent transients suffices to demonstrate the beneficial effect of adding tin, the quantitative results may not be accurate since illumination is likely to change the band bending as a consequence of the build–up of holes at the surface (note the asymmetry between the “on” and “off” transients). For this reason, we used IMPS to extract the time constants for hole-transfer and surface electron-hole recombination as described in the theory section. In the following discussion, we focus on the comparison of the pure hematite and 20 % Sn doped sample, since this gave the highest photocurrent. Typical IMPS spectra obtained for samples doped with 0 % and 20 % Sn are shown in Figure 5-66. Both doped and undoped samples give very similar high-frequency semi-circles in the lower quadrant, which correspond to the RC attenuation of the IMPS response with the time constant $R_{series}C_{sc}$. Since the series resistance is of the order of 25 Ω for both samples, this indicates that the space charge capacitance, and hence the width of the space charge layer, is not changed by the incorporation of Sn. Provided the time constant of the recombination semicircle is at least two orders of magnitude slower than the RC time constant, RC attenuation does not interfere with the kinetic analysis.

By contrast, the low-frequency semicircles in the upper quadrant, which correspond to the competition between charge transfer and recombination, are quite different. Whereas the undoped sample gives a semicircle that returns almost to the origin at low frequencies, the semicircle for the Sn-doped sample is much smaller with a low frequency intercept that is much larger. The ratios of the high and low frequency intercepts of the recombination semicircles give values of the transfer efficiency, see Figure 5-7a. These values are in excellent agreement with the results obtained from the analysis of the corresponding photocurrent transients, see Figure 5-b. The potential dependence of k_{trans} and k_{rec} obtained from the analysis of the IMPS responses is illustrated in Figure 5-7b & c. The k_{rec} values are very similar for both samples, except at the most negative potentials, where the 20 % Sn sample exhibits slightly faster recombination. Strikingly, Sn-inclusion increases k_{trans} by more than an order of magnitude across almost the whole potential range, indicating that Sn catalyses the light-driven OER (note the logarithmic scale in Figure 5-7c).

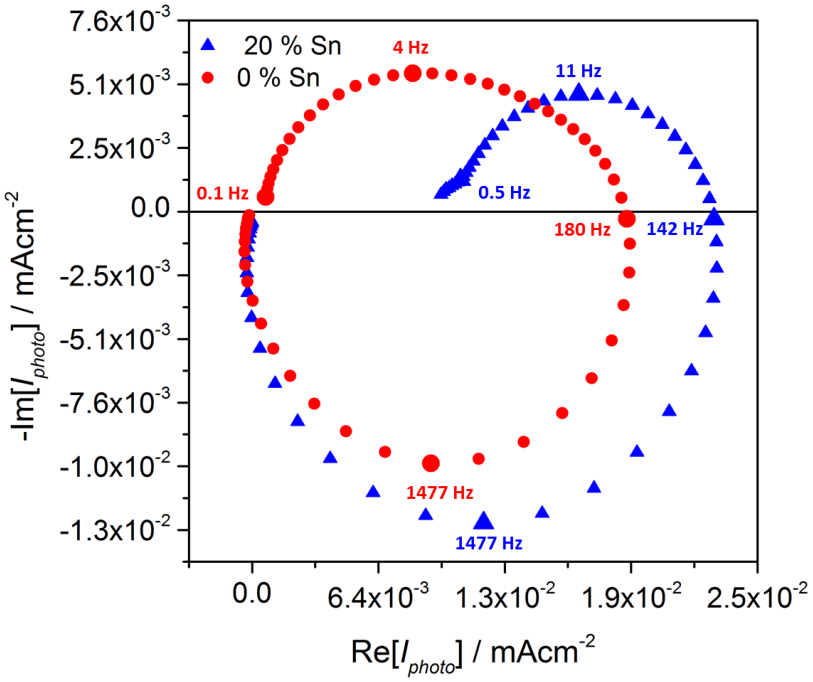

Figure 5-6. IMPS spectra of samples prepared with 0 % and 20 % Sn-precursor in the synthesis, recorded at 1.164 V vs. RHE. λ = 470 nm, incident photon flux 10^{17} $cm^{-2}s^{-1}$. Note the large difference in the low frequency semicircles, which reflect the competition between charge transfer and recombination.

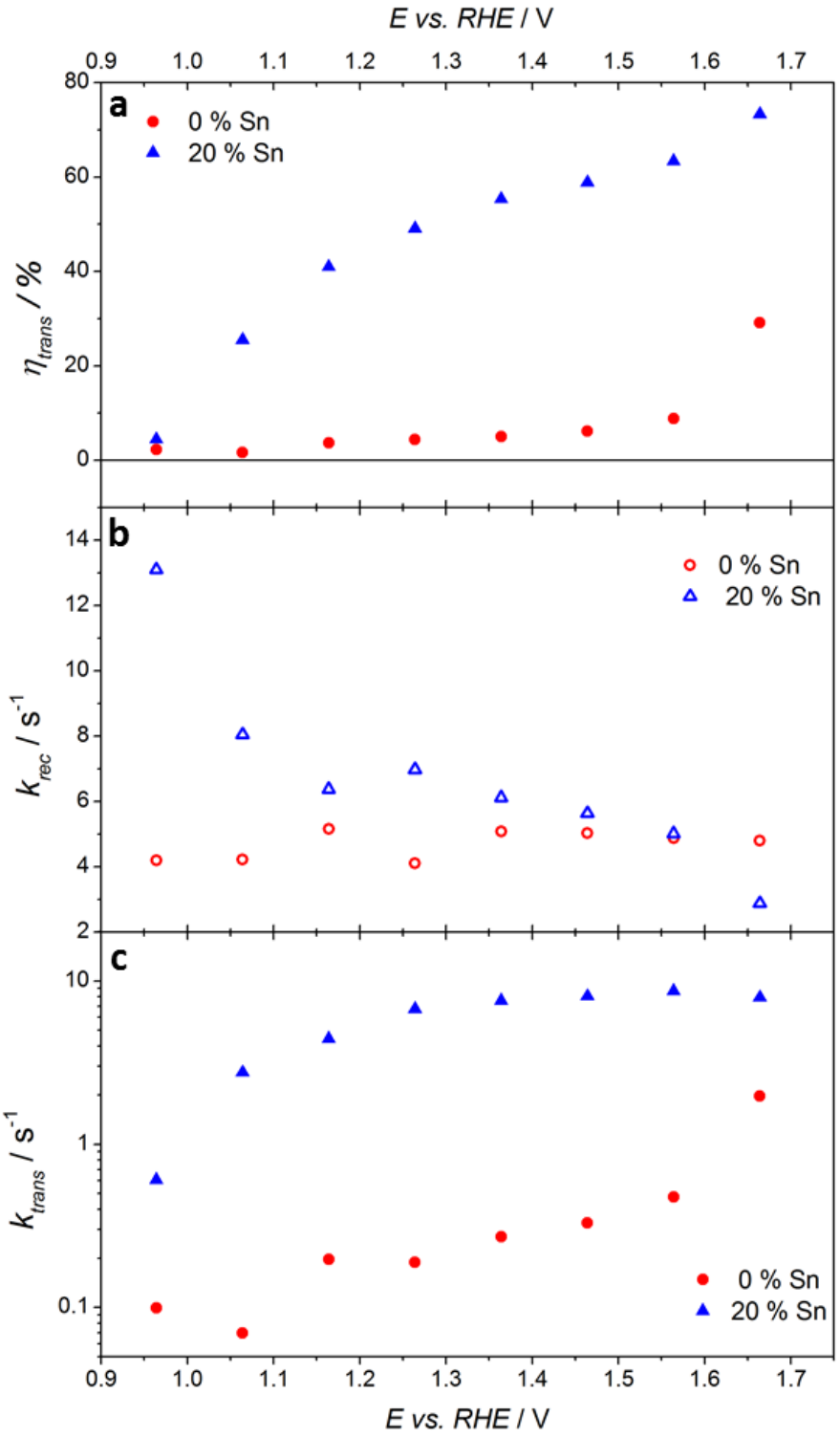

Figure 5-7. Parameters extracted from IMPS of photoanodes prepared with 0 % and 20 % Sn-precursor in the synthesis, illuminated by a 470 nm LED, intensity 10^{17} $cm^{-2}s^{-1}$. a) Transfer efficiency, b) rate constant for electron-hole recombination, c) rate constant for hole transfer.

Having established that the improved performance of hematite photoanodes prepared with an additional Sn-precursor in the synthesis is due to the catalysis of the OER reaction, we investigated the location of the Sn in the structure. Powder XRD and electron diffraction in

TEM mode (Figures SI 5-2 and SI 5-3 in the supporting information) indicate that the overall structure of the material remains that of hematite, without the formation of secondary phases (SnO_2, for example). Furthermore the Mott-Schottky analysis does not point towards a significant change in the electron donor density, indicating that Sn is not acting as an electrical dopant (see Figure SI 5-4 in the supporting information). The presence of Sn in the hematite layers was confirmed by EDX in TEM mode. 25 individual EDX spectra were acquired on 20 % Sn doped samples, for which both the position of the electron beam and its diameter were chosen at random, leading to EDX-measurements of areas of several micrometers as well as of individual particles. All measurements yielded similar Sn contents, indicating a homogeneous distribution on the micron scale. A mean Sn-concentration of 3.2 ± 1.5 atomic-% was calculated using the Cliff-Lorimer equation.

Since these measurements did not probe the distribution of Sn within the individual hematite particles, scanning transmission electron microscopy (STEM) was employed in combination with EDX to probe the Sn-content with a step size of approximately 2 nm. To this end, an electron beam with a diameter of less than 1 nm and, consequently low intensity, was used. Line scans across the width of a particle can reveal inhomogeneities between surface and bulk compositions, as illustrated in the inset of Figure 5-88b. Six particles were probed along lines approximately perpendicular to the surface, such as the one depicted in Figure 5-88a. Due to an insufficient signal-to-noise-ratio, background subtraction could not be performed, and therefore the local atomic ratio could not be quantified. However, the ratio of the intensity of the signals attributable to Sn and that obtained from both Sn and Fe (including the background), revealed a substantial Sn-enrichment at all measured surfaces. The Sn-content strongly decays towards the middle of the particle, where very little signal attributable to Sn was detected. The enrichment of Sn at the surface is also visible in the HAADF-STEM images as a white brim. Since the signal in HAADF-STEM images is approximately proportional to the square of the atomic number, the bright rim is attributed to a higher average atomic number, which is consistent with the inclusion of Sn in the surface atomic columns. Thus, we conclude from our EDX line scan and HAADF STEM results that the introduction of a Sn-precursor into the hematite synthesis leads to a core-shell structure with incorporated Sn-atoms preferentially located near the surface. Due to the small overall content of Sn, an investigation of the mode of tin incorporation into the hematite structure proved difficult. However, in HRTEM images such as those shown in Figure 5-8c, 5-8d, the lattice planes of both an undoped and a doped sample extend to the particle edge, and there is no evidence for newly formed separate phases such as SnO_2 or SnO at the surface. We therefore conclude that the Sn incorporates into the hematite structure without substantial structural changes.

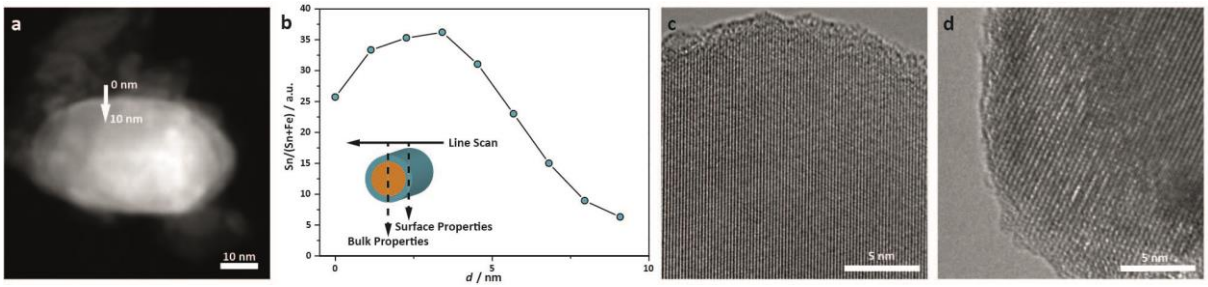

Figure 5-8: a) a HAADF-STEM image of the 20 % Sn particles probed with EDX and b) relative atomic content of Sn to total metal atomic content as a function of position along the line-scan marked in a). The sketch inset in b) illustrates how the STEM beam probes the bulk and surface properties of the particles. Furthermore, HRTEM images of c) undoped, and d) Sn-doped, hematite are shown. In c), the (202) lattice planes are shown, in d) the (012) lattice planes.

This structure-function relationship between an enrichment of Sn at the surface of hematite, and catalysis of the OER is in good agreement with theoretical predictions that mixed metal sites at the hematite surface (*i.e.* surface doping) could play a role in balancing the intermediate energetic barriers involved in the OER.[38,39] Although these studies considered many common hematite dopants such as Si and Ti, Sn was not included. Given the phenomenological nature of the rate constants obtained here, it is plausible that Sn atoms on the hematite surface affect the OER intermediates, which would, in turn lead to an increased k_{trans}. Zandi *et al.*[37] observed an increased transfer efficiency in Ti-doped hematite prepared by ALD, although exclusively coating the hematite surface with TiO_2 had no beneficial effect on undoped hematite, which we suggest may also be due to the existence of neighbouring Ti and Fe sites. Similarly, Chemelewski *et al.* noted an increased transfer efficiency of hematite photoanodes upon Si doping.[24] Although these studies identified an enhanced transfer efficiency by comparing the photoanode performance in the presence and absence of a hole scavenger, determining whether this enhancement was due to a catalytic effect or a passivation of surface recombination was not possible. To the best of our knowledge, the present study provides the first demonstration that doping hematite photoanodes can catalyse the OER. A parallel can be drawn between our findings and recent work by Riha *et al.*,[15] who showed by analysis of PEIS spectra that a sub-monolayer Co-coating also catalyses the OER on hematite photoanodes. Interestingly, the authors note that the existence of neighbouring Fe and Co sites may be crucial to this catalytic activity. We suggest that this may be another example of the behavior predicted by Busch and Carter.[38,39] While many Co species are well-known dark OER catalysts, Sn showed unexpected catalytic activity towards the OER on hematite photoanodes. We are therefore encouraged to believe that the search for catalysts for photoelectrodes can be extended beyond successful dark catalysts, as the mechanisms involved may be very different.

5.5. Conclusion

We have synthesized thin Sn-enriched hematite layers as model systems to investigate the role of Sn doping under light-driven water oxidation conditions. Although the performance of this material was low due to its modest light harvesting efficiency, the internal quantum efficiency is similar to those reported for benchmark hematite photoanodes prepared by AACVD and ultrasonic spray pyrolysis, making it a useful model system. Transient photocurrent responses to chopped illumination revealed that the efficiency of hole-transfer to the solution phase during the OER increased significantly due to the Sn doping. A study by IMPS revealed a tenfold increase in the rate of hole-transfer, *i.e.* catalysis of the OER. This is remarkable, as very few studies of surface treatments have found convincing evidence of catalysis, with many observing passivation of surface recombination. To the best of our knowledge, we report the first example of a dopant catalysing the OER on hematite. STEM-EDX line scans revealed a Sn-enrichment at the surface of the nanoparticles, indicating a structure-function relationship between the surface nature of the Sn doping, and the improved catalytic properties at the surface. While we do not claim that all dopants affect hematite in this way, we believe that catalysis due to surface doping may be a widespread effect, and suggest more routine application of techniques such as IMPS to distinguish between changes in the rates of hole transfer and surface recombination brought about by inclusion of dopant atoms. We also hope that these results will motivate the search for catalysts beyond traditional dark OER catalysts.

5.6. Subsequent Work: Ultrasmall Co_3O_4 Nanoparticles as Co-Catalysts

This segment is based on the following publication:

"Ultrasmall Co_3O_4 Nanocrystals Strongly Enhance Solar Water Splitting on Mesoporous Hematite" by Johann M. Feckl, Halina K. Dunn, Peter M. Zehetmaier, Alexander Müller, Stephanie R. Pendlebury, Patrick Zeller, Ksenia Fominykh, Ilina Kondofersky, Markus Döblinger, James R. Durrant, Christina Scheu, Laurence M. Peter, Dina Fattakhova-Rohlfing, and Thomas Bein, which was published in Advanced Materials Interfaces, DOI: 10.1002/admi.201500358 (2015).

Hematite suffers from slow surface kinetics, which can be improved by depositing co-catalysts. In this study, Co_3O_4 nanoparticles were synthesized and applied as co-catalysts to the mesoporous, Sn-doped hematite films discussed above.[59] Compared to prior work, Co_3O_4 was prepared prior to application, allowing homogenous deposition as shown by TEM. The nanoparticles were 3 to 7 nm in diameter, non-agglomerated and perfectly dispersible in ethanol. Deposition led to a photocurrent increase of up to several hundred % throughout the current-voltage curve. However, the performance dropped significantly if the Co_3O_4 loading was increased beyond a certain level, which was attributed to blocking of the Fe_2O_3 surface

(Figure 5-9). Transient absorption spectroscopy showed the enhanced performance to be due to suppression of surface electron-hole recombination on the scale of milliseconds to seconds.

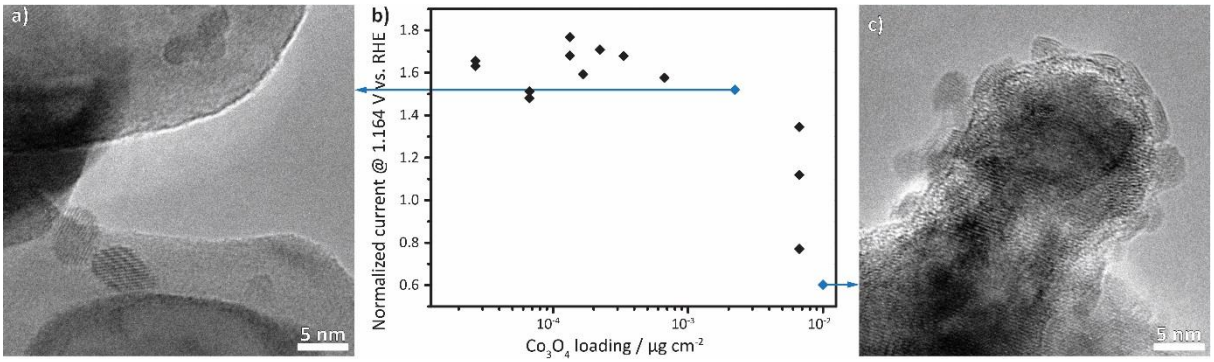

Figure 5-9: The normalized photocurrent at 1.164 V versus RHE (pH 13) under 455 nm illumination, of Co_3O_4-treated 150 nm thick Sn-doped hematite films as a function of Co_3O_4 nanoparticle loading on the active area of the electrodes is shown in (b). The normalized current is displayed as a ratio of photocurrent of Co_3O_4 nanoparticle–treated electrodes to that of an untreated electrode of the same thickness. (a) and (b) show TEM images to illustrate the different surface coverages. The figure is taken from [59].

5.7. Subsequent Work: Introduction of a Current-Collecting Scaffold

This segment is based on the following publication:

"Electron Collection in Host−Guest Nanostructured Hematite Photoanodes for Water Splitting: The Influence of Scaffold Doping Density" by Ilina Kondofersky, Halina K. Dunn, Alexander Müller, Benjamin Mandlmeier, Johann M. Feckl, Dina Fattakhova-Rohlfing, Christina Scheu, Laurence M. Peter, and Thomas Bein, which was published in ACS Applied Materials and Interfaces 7, 4623 (2015).

The poor electron collection of hematite has led to the emergence of host-guest architectures, in which hematite nanoparticles are deposited onto a transparent electron collector.[60] In this study, the Sn-doped Fe_2O_3 nanoparticles described above were applied to a macroporous antimony-doped tin oxide (ATO) scaffold.[61] TEM cross-sections were prepared as described in Chapter 3. The homogenous distribution and complete infiltration of the scaffold by the hematite nanoparticles was shown with EDX maps of TEM cross-sections (Figure 5-10). An average pore size of 300 nm could be determined, and the nanoparticle shapes and sizes were similar in meso- and macroporous samples. The impact of the morphology and the material combination was investigated by comparing its performance to that of an undoped SnO_2 host and to that of unscaffolded, mesoporous Sn-doped Fe_2O_3. Analysis of the IPCE spectra for substrate and electrolyte side illumination reveals that the electron diffusion length in the host−guest electrodes based on an undoped SnO_2 scaffold is increased substantially relative to the nanostructured hematite electrode without a supporting scaffold. Nevertheless,

electron collection is still incomplete for electrolyte illumination. By contrast, an electron collection efficiency of 100 % is achieved with the ATO scaffold, showing that the conductivity of the scaffold is crucial for the device performance.

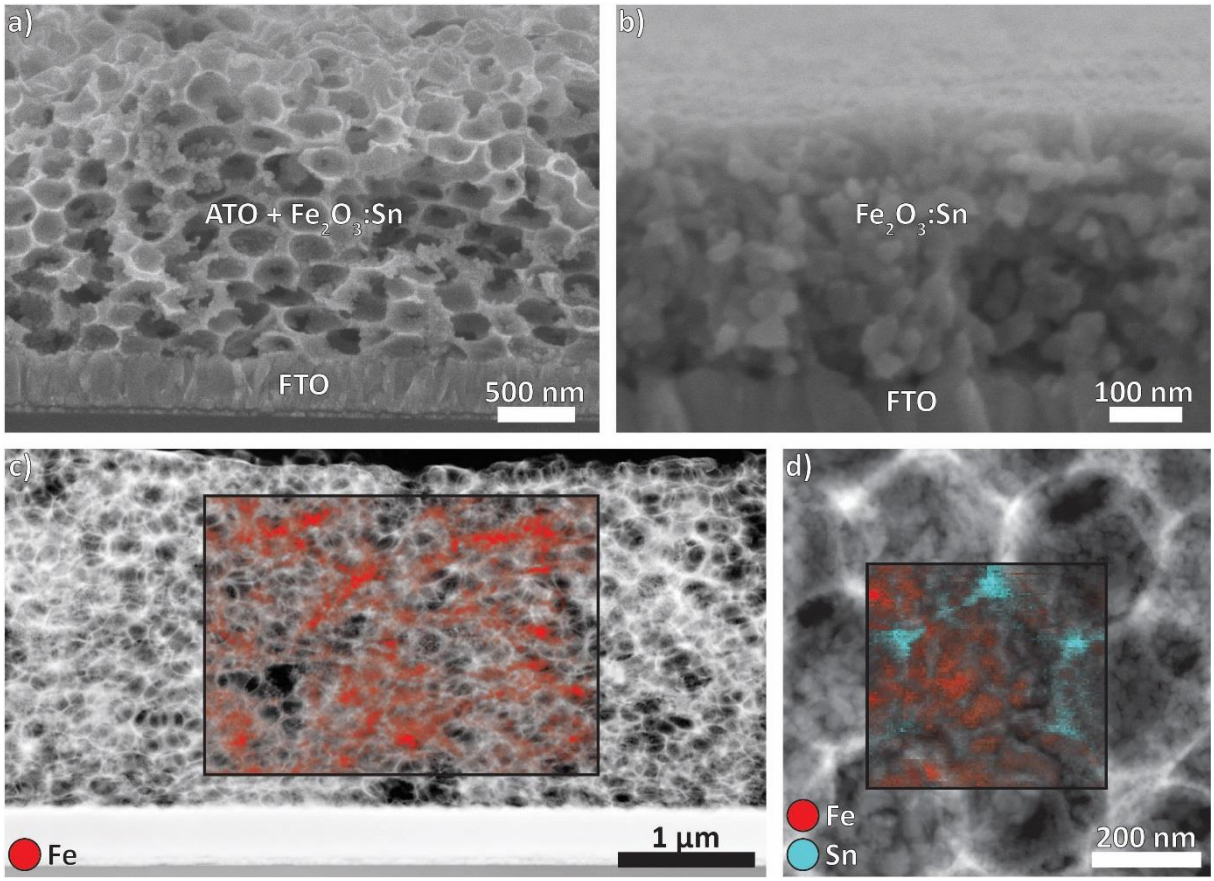

Figure 5-10: SEM cross section images of (a) the ATO + Sn:Fe_2O_3 host–guest morphology and (b) the mesoporous Sn:Fe_2O_3 absorber layer. In (c) and (d), EDX maps of a cross-section of the host–guest morphology, which were acquired in STEM, are shown. (c) shows good infiltration of the absorber in the scaffold down to the bottom, although some pores remain unfilled, and (d) shows one pore with several hematite nanoparticles. The figure is taken from [4].

5.8. Supporting Information

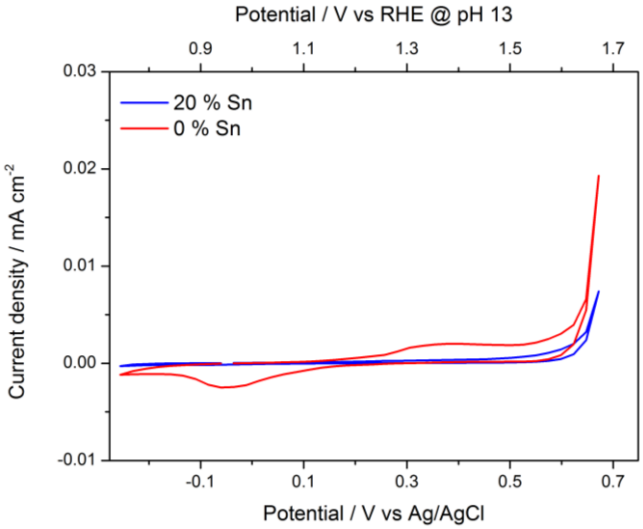

Figure SI 5-1: Dark cyclic voltammograms recorded on single layer films of pure hematite, and of hematite prepared with 20 % Sn-precursor in the synthesis.

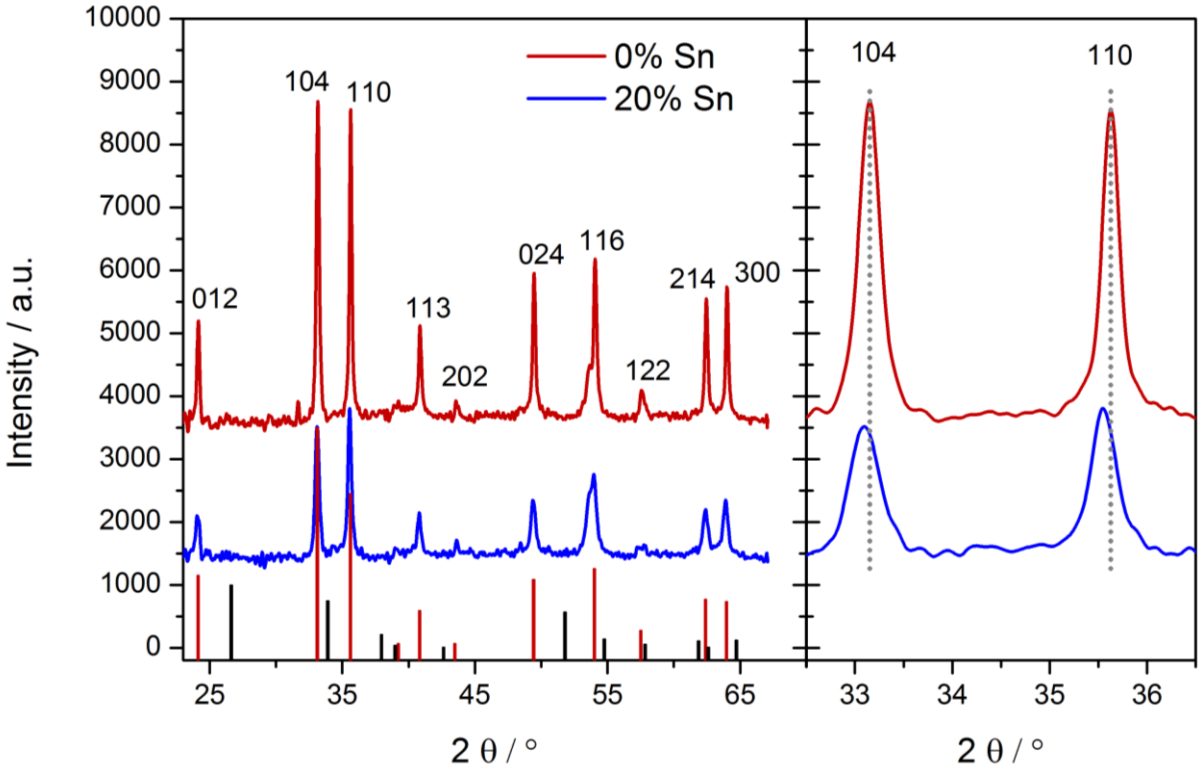

Figure SI 5-2: Powder XRD data of hematite layers prepared with 0 % and 20 % Sn-precursor in the synthesis. Below the ICDD card 01-085-0987 of hematite (red) and the ICDD card 01-075-9493 of SnO_2 (black). The right hand panel shows the peak shift attributed to lattice distortion upon inclusion of Sn-atoms.

The powder XRD spectra in Figure SI 5-1Figure SI exclusively show the α-Fe_2O_3 hematite phase, with a peak shift of approximately 0.1° to smaller angles upon Sn-inclusion (20 % sample), indicating a lattice distortion brought about by inclusion of impurity atoms.[1] This shift corresponds to an increase of the lattice parameter, *a*, from 5.036 to 5.043 Å. Additionally, the inversion of intensities of the two reflections in the range of 33 to 36° 2θ is observed, similar to a Sn-doped hematite described by Berry *et al.*[1] The mean crystallite size, as calculated from the broadening of the (104) reflection according to the Scherrer equation, drops from 50 to 30 nm upon inclusion of Sn. This is in good agreement with the reduction in particle size upon Sn-inclusion observed in SEM and TEM. Hence, our XRD, SEM and TEM investigations agree on a reduction in feature size upon Sn-incorporation. Although this observation fits the general trend, we note that this change in feature size is less extreme than in other reports, such as the reduction in hematite nanowire length from 600 to 100 nm upon Sn-doping reported by Ling *et al.*[2]

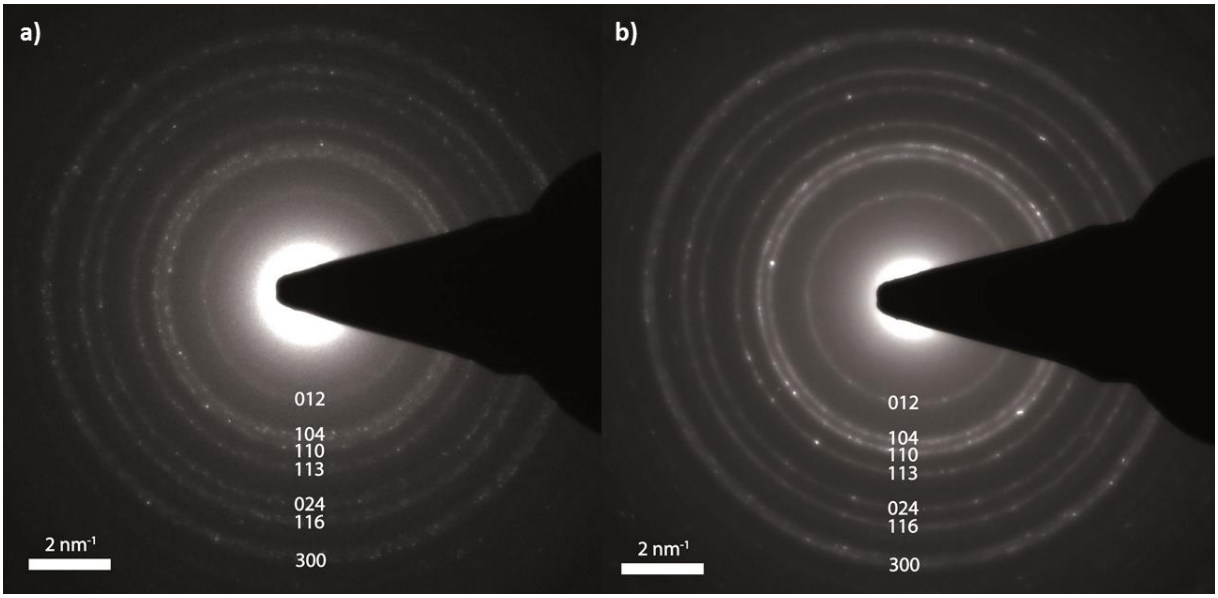

Figure SI 5-3: Electron diffraction patterns obtained in TEM of a) 20 % and b) 0 % Sn samples.

Diffraction patterns of several hundred particles confirmed the hematite structure, to which all reflections could be assigned.

EIS data were fitted to the Randles' equivalent circuit shown in the inset of Figure SI 5-4, with parallel resistances, R_p, of the order of 10 kΩ cm^{-2} corresponding to the small dark current. The capacitances determined in this way are shown as Mott-Schottky plots in Figure SI 5-4. As these electrodes are not perfectly compact and uniform layers, the data are not linear over the entire range. However, at low applied anodic biases, a linear fit can be made, yielding flatband potentials, V_{FB}, of *ca.* 0.7 and 0.4 V vs RHE for 0 % and 20 % samples, respectively. Another indicator of V_{FB} is the onset potential of anodic transient photoactivity.[5] The photocurrent-voltage curves under chopped illumination, shown in Figure SI 5-5, reveal that

V_{FB} is of the order of 0.6 and 0.3 V vs RHE for the 0 % and 20 % photoanodes, respectively, in good agreement with the values determined from the Mott-Schottky analysis.

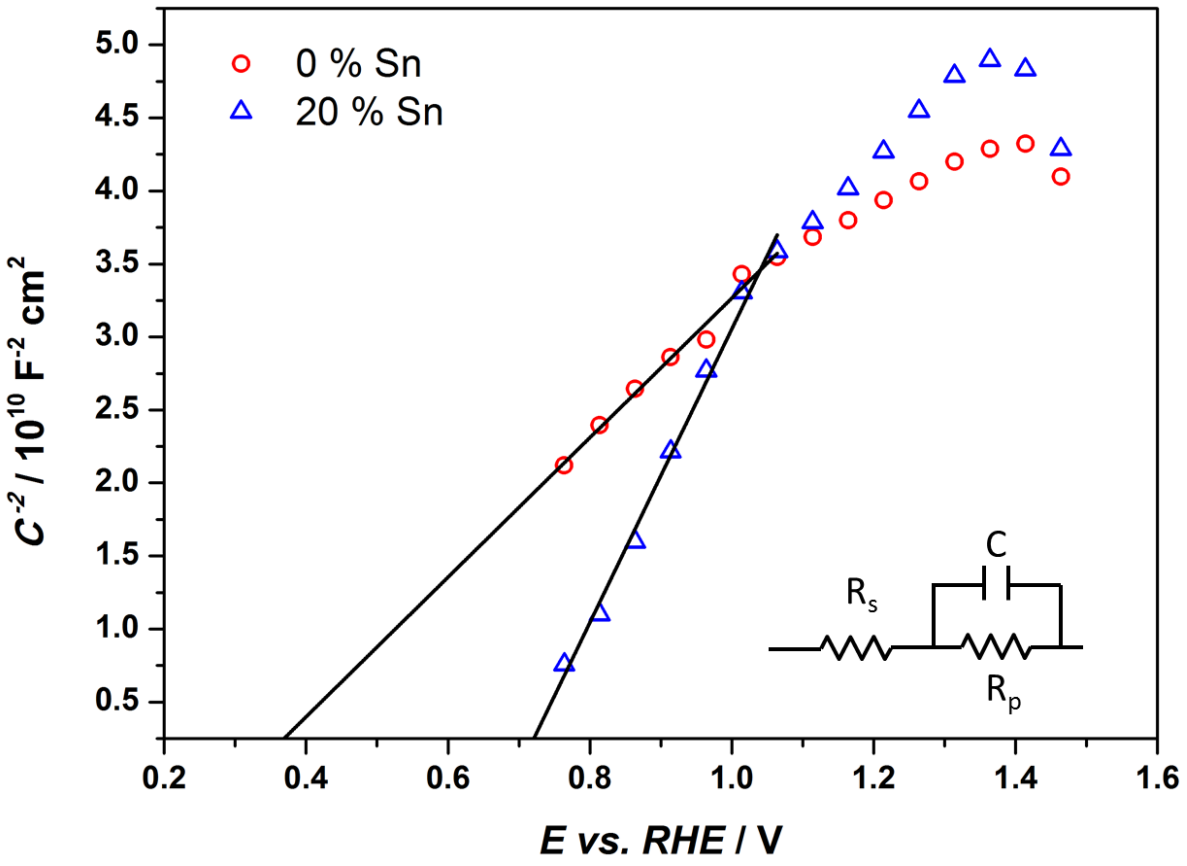

Figure SI 5-4: Mott-Schottky plots obtained from hematite photoanodes prepared with 0 % and 20 % Sn-precursor in the synthesis.

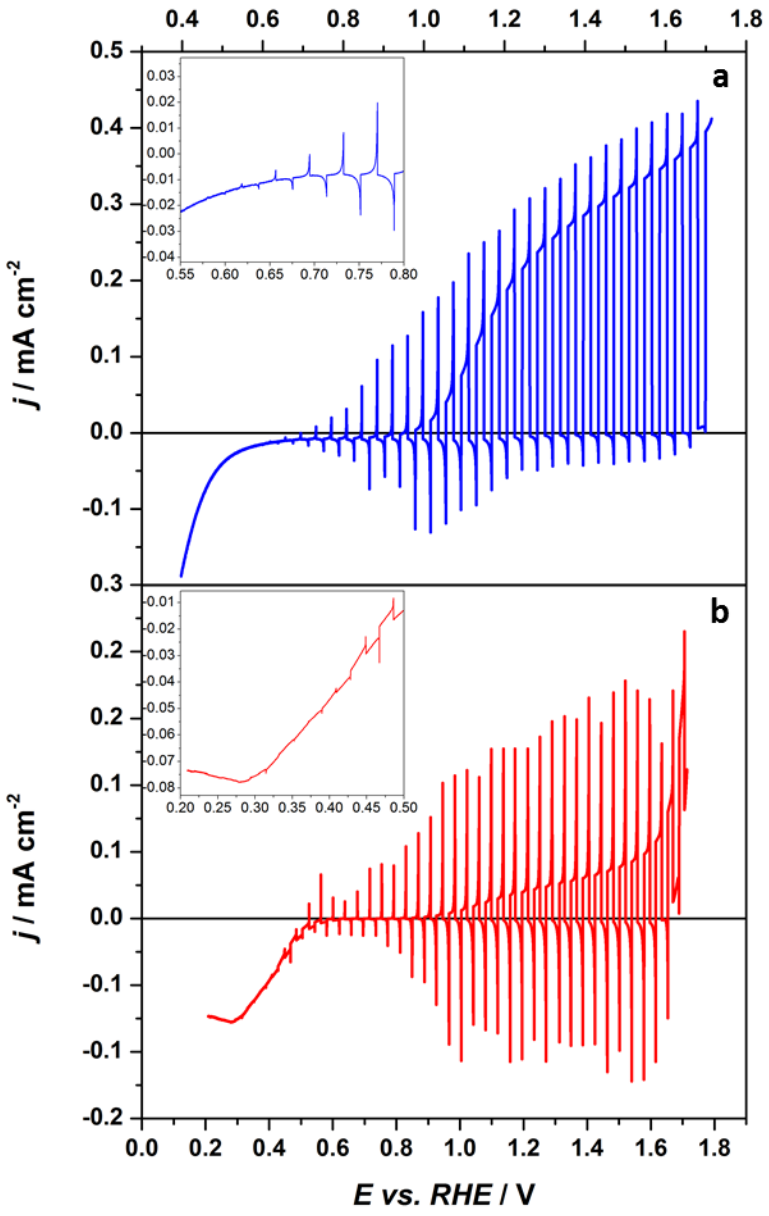

Figure SI 5-5: Current density under chopped illumination of hematite photoanodes prepared with 20 % (a) and 0 % (b) Sn-precursor in the synthesis. Monochromatic light (455 nm) chopped at 1 Hz, intensity ca. 10^{17} $cm^{-2}s^{-1}$, scan rate: 40 mVs^{-1}. The insets show the onset of transient photocurrent activity close to the flat band potential.

In order to calculate the doping density and the width of the space charge layer according to equation 6 (in the main text) the value of the dielectric constant, ε_r, is required. There is a wide range of ε_r values reported in the literature.[6,7] We have calculated W_{SC} from equation 6 with ε_r equal to 25[8] and 57[7] to illustrate the sensitivity of W_{SC} to this parameter, see Figure SI 5-6. For the higher value of the dielectric constant, the plots show that the assumption that the width of the space charge regions should be smaller than the particle radius, R will no longer be met for 30 nm particles, and the capacitance should saturate at high applied bias. However no experimental evidence for saturation of the capacitance was seen in the Mott Schottky plots, and we therefore believe that the dielectric constant is small enough that the

condition $W_{sc} < R$ is satisfied. This conclusion is supported by recent theoretical calculations that predict ε_r values close to 25.[8]

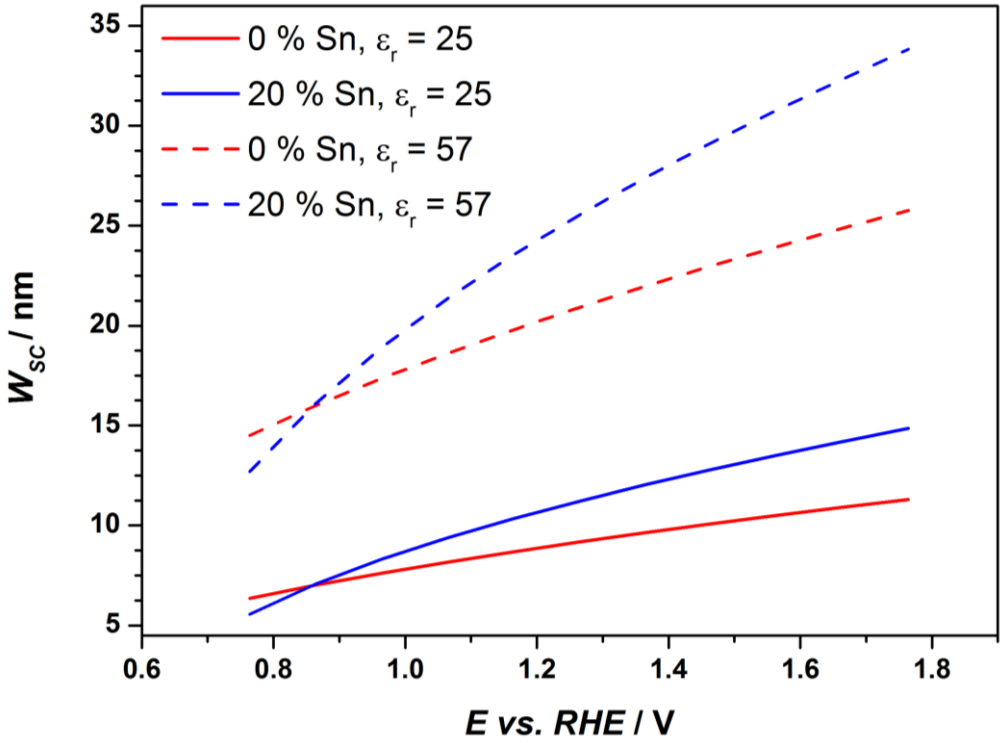

Figure SI 5-6: Calculated width of the space charge region for hematite photoanodes prepared with 0 % and 20 % Sn-precursor in the synthesis. V_{FB} was estimated from Mott-Schottky analysis and the transient anodic onset of photocurrent. For the pure hematite sample, donor densities of 3.2 10^{19} cm^{-3}, and of 1.3 10^{19} cm^{-3} were used in combination with dielectric constants of 25 and 57, respectively. For the Sn-enriched hematite sample, donor densities of 1.5 $\times 10^{19}$ cm^{-3}, and of 6.6 $\times$ 10^{18} cm^{-3} were used in combination with dielectric constants of 25 and 57, respectively.

5.9. Acknowledgments

The work was supported by the German Research Foundation, DFG (SPP 1613), Nanosystems Initiative Munich (NIM) and LMUexcellent funded by the DFG, the Bavarian research network 'Solar Technologies Go Hybrid', the Center for NanoScience (CeNS) and LMUmentoring. Ilina Kondofersky is gratefully acknowledged for insightful discussions. We also thank Steffen Schmidt and Florian Auras for SEM measurements.

5.10. References

(1) Bolton, J. R.; Strickler, S. J.; Connolly, J. S. *Nature* **1985**, *316*, 495.

(2) Brillet, J.; Cornuz, M.; Le, F. F.; Yum, J.-H.; Gratzel, M.; Sivula, K. *J. Mater. Res.* **2010**, *25*, 17.

(3) Neumann, B.; Bogdanoff, P.; Tributsch, H. *J. Phys. Chem. C* **2009**, *113*, 20980.

(4) Brillet, J.; Yum, J. H.; Cornuz, M.; Hisatomi, T.; Solarska, R.; Augustynski, J.; Graetzel, M.; Sivula, K. *Nature Photonics* **2012**, *6*, 823.
(5) Khaselev, O.; Turner, J. A. *Science* **1998**, *280*, 425.
(6) Nozik, A. J. *Appl. Phys. Lett.* **1976**, *29*, 150.
(7) Sivula, K.; Le, F. F.; Gratzel, M. *ChemSusChem* **2011**, *4*, 432.
(8) Katz, M. J.; Riha, S. C.; Jeong, N. C.; Martinson, A. B. F.; Farha, O. K.; Hupp, J. T. *Coordination Chemistry Reviews* **2012**, *256*, 2521.
(9) Cesar, I.; Kay, A.; Martinez, J. A. G.; Gratzel, M. *Journal of the American Chemical Society* **2006**, *128*, 4582.
(10) Kay, A.; Cesar, I.; Graetzel, M. *Journal of the American Chemical Society* **2006**, *128*, 15714.
(11) Cesar, I.; Sivula, K.; Kay, A.; Zboril, R.; Graetzel, M. *Journal of Physical Chemistry C* **2009**, *113*, 772.
(12) Kim, J. Y.; Magesh, G.; Youn, D. H.; Jang, J.-W.; Kubota, J.; Domen, K.; Lee, J. S. *Sci. Rep.* **2013**, *3*.
(13) Tilley, S. D.; Cornuz, M.; Sivula, K.; Graetzel, M. *Angew. Chem., Int. Ed.* **2010**, *49*, 6405.
(14) Klahr, B.; Gimenez, S.; Fabregat-Santiago, F.; Bisquert, J.; Hamann, T. W. *Journal of the American Chemical Society* **2012**, *134*, 16693.
(15) Riha, S. C.; Klahr, B. M.; Tyo, E. C.; Seifert, S.; Vajda, S.; Pellin, M. J.; Hamann, T. W.; Martinson, A. B. F. *Acs Nano* **2013**, *7*, 2396.
(16) Barroso, M.; Cowan, A. J.; Pendlebury, S. R.; Graetzel, M.; Klug, D. R.; Durrant, J. R. *Journal of the American Chemical Society* **2011**, *133*, 14868.
(17) Peter, L. M.; Wijayantha, K. G. U.; Tahir, A. *Faraday Discussions* **2011**.
(18) Hahn, N. T.; Mullins, C. B. *Chemistry of Materials* **2010**, *22*, 6474.
(19) Bohn, C. D.; Agrawal, A. K.; Walter, E. C.; Vaudin, M. D.; Herzing, A. A.; Haney, P. M.; Talin, A. A.; Szalai, V. A. *Journal of Physical Chemistry C* **2012**, *116*, 15290.
(20) Frydrych, J.; Machala, L.; Tucek, J.; Siskova, K.; Filip, J.; Pechousek, J.; Safarova, K.; Vondracek, M.; Seo, J. H.; Schneeweiss, O.; Graetzel, M.; Sivula, K.; Zboril, R. *Journal of Materials Chemistry* **2012**, *22*, 23232.
(21) Ling, Y.; Wang, G.; Wheeler, D. A.; Zhang, J. Z.; Li, Y. *Nano Lett.* **2011**, *11*, 2119.
(22) Sivula, K.; Zboril, R.; Le Formal, F.; Robert, R.; Weidenkaff, A.; Tucek, J.; Frydrych, J.; Graetzel, M. *Journal of the American Chemical Society* **2010**, *132*, 7436.
(23) Saremi-Yarahmadi, S.; Wijayantha, K. G. U.; Tahir, A. A.; Vaidhyanathan, B. *Journal of Physical Chemistry C* **2009**, *113*, 4768.
(24) Chemelewski, W. D.; Hahn, N. T.; Mullins, C. B. *Journal of Physical Chemistry C* **2012**, *116*, 5256.
(25) Lukowski, M. A.; Jin, S. *Journal of Physical Chemistry C* **2011**, *115*, 12388.
(26) Franking, R.; Li, L. S.; Lukowski, M. A.; Meng, F.; Tan, Y. Z.; Hamers, R. J.; Jin, S. *Energy & Environmental Science* **2013**, *6*, 500.
(27) Zhang, P.; Kleiman-Shwarsctein, A.; Hu, Y.-S.; Lefton, J.; Sharma, S.; Forman, A. J.; McFarland, E. *Energy & Environmental Science* **2011**, *4*, 1020.

(28) Wang, G.; Ling, Y.; Wheeler, D. A.; George, K. E. N.; Horsley, K.; Heske, C.; Zhang, J. Z.; Li, Y. *Nano Letters* **2011**, *11*, 3503.
(29) Lian, X.; Yang, X.; Liu, S.; Xu, Y.; Jiang, C.; Chen, J.; Wang, R. *Applied Surface Science* **2012**, *258*, 2307.
(30) Deng, J.; Zhong, J.; Pu, A.; Zhang, D.; Li, M.; Sun, X.; Lee, S.-T. *Journal of Applied Physics* **2012**, *112*.
(31) Hu, Y.-S.; Kleiman-Shwarsctein, A.; Forman, A. J.; Hazen, D.; Park, J.-N.; McFarland, E. W. *Chemistry of Materials* **2008**, *20*, 3803.
(32) Mao, A.; Park, N.-G.; Han, G. Y.; Park, J. H. *Nanotechnology* **2011**, *22*.
(33) Kleiman-Shwarsctein, A.; Hu, Y.-S.; Forman, A. J.; Stucky, G. D.; McFarland, E. W. *Journal of Physical Chemistry C* **2008**, *112*, 15900.
(34) Kumari, S.; Tripathi, C.; Singh, A. P.; Chauhan, D.; Shrivastav, R.; Dass, S.; Satsangi, V. R. *Current Science* **2006**, *91*, 1062.
(35) Khan, S. U. M.; Zhou, Z. Y. *Journal of Electroanalytical Chemistry* **1993**, *357*, 407.
(36) Liao, P.; Toroker, M. C.; Carter, E. A. *Nano Letters* **2011**, *11*, 1775.
(37) Zandi, O., Klahr, B.M., Hamann, T.W. *Energy & Environmental Science* **2013**, *6*.
(38) Liao, P.; Keith, J. A.; Carter, E. A. *Journal of the American Chemical Society* **2012**, *134*, 13296.
(39) Busch, M.; Ahlberg, E.; Panas, I. *Physical Chemistry Chemical Physics* **2011**, *13*, 15062.
(40) Tang, H.; Matin, M. A.; Wang, H.; Deutsch, T.; Al-Jassim, M.; Turner, J.; Yan, Y. *Journal of Applied Physics* **2011**, *110*.
(41) Dotan, H.; Sivula, K.; Gratzel, M.; Rothschild, A.; Warren, S. C. *Energy Environ. Sci.* **2011**, *4*, 958.
(42) Gärtner, W. W. *Physical Review* **1959**, *116*, 84.
(43) Dareedwards, M. P.; Goodenough, J. B.; Hamnett, A.; Trevellick, P. R. *Journal of the Chemical Society-Faraday Transactions I* **1983**, *79*, 2027.
(44) Cummings, C. Y.; Marken, F.; Peter, L. M.; Tahir, A. A.; Wijayantha, K. G. U. *Chemical Communications* **2012**, *48*, 2027.
(45) Peter, L. M. *Journal of Solid State Electrochemistry* **2013**, *17*, 315.
(46) Ponomarev, E. A.; Peter, L. M. *Journal of Electroanalytical Chemistry* **1995**, *396*, 219.
(47) Peter, L. M.; Ponomarev, E. A.; Fermin, D. J. *Journal of Electroanalytical Chemistry* **1997**, *427*, 79.
(48) Wijayantha, K. G. U.; Saremi-Yarahmadi, S.; Peter, L. M. *Physical Chemistry Chemical Physics* **2011**, *13*, 5264.
(49) Peter, L. M.; Vanmaekelbergh, D. In *Adv. Electrochem. Sci. Eng.*; Alkire, R. C. K., D.M., Ed. Weinheim, 1999; Vol. 6, p 77.
(50) Peter, L. M. T., H. In *Nanostructured And Photoelectrochemical Systems For Solar Photon Conversion*; Archer, M. D. N., A.J, Ed.; Imperial College Press: London, 2008; Vol. 3, p 675.
(51) Fermin, D. J.; Ponomarev, E. A.; Peter, L. M. *J. Electroanal. Chem.* **1999**, *473*, 192.
(52) Redel, E.; Mirtchev, P.; Huai, C.; Petrov, S.; Ozin, G. A. *Acs Nano* **2011**, *5*, 2861.
(53) Klahr, B. M.; Martinson, A. B. F.; Hamann, T. W. *Langmuir* **2011**, *27*, 461.

(54) Morrish, R.; Rahman, M.; MacElroy, J. M. D.; Wolden, C. A. *Chemsuschem* **2011**, *4*, 474.
(55) Hamd, W.; Cobo, S.; Fize, J.; Baldinozzi, G.; Schwartz, W.; Reymermier, M.; Pereira, A.; Fontecave, M.; Artero, V.; Laberty-Robert, C.; Sanchez, C. *Physical Chemistry Chemical Physics* **2012**, *14*, 13224.
(56) Glasscock, J. A.; Barnes, P. R. F.; Plumb, I. C.; Bendavid, A.; Martin, P. J. *Thin Solid Films* **2008**, *516*, 1716.
(57) Lunt, R.; Jackson, A.; Walsh, A. *Chemical Physics Letters* **2013**, *586*, 67.
(58) Barroso, M.; Mesa, C. A.; Pendlebury, S. R.; Cowan, A. J.; Hisatomi, T.; Sivula, K.; Graetzel, M.; Klug, D. R.; Durrant, J. R. *Proceedings of the National Academy of Sciences of the United States of America* **2012**, *109*, 15640.
(59) Feckl, J. M.; Dunn, H. K.; Zehetmaier, P. M.; Müller, A.; Pendlebury, S. R.; Zeller, P.; Fominykh, K.; Kondofersky, I.; Döblinger, M.; Durrant, J. R.; Scheu, C.; Peter, L.; Fattakhova-Rohlfing, D.; Bein, T. *Adv. Mater. Interfaces* **2015**, DOI: 10.1002/admi.201500358.
(60) Sivula, K.; Formal, F. Le; Grätzel, M. *Chem. Mater.* **2009**, *21* (13), 2862.
(61) Kondofersky, I.; Dunn, H. K.; Müller, A.; Mandlmeier, B.; Feckl, J. M.; Fattakhova-Rohlfing, D.; Scheu, C.; Peter, L. M.; Bein, T. *ACS Appl. Mater. Interfaces* **2015**, *7*, 4623.

6. Dual Absorber Fe_2O_3/WO_3 Host-Guest Architectures for Improved Charge Generation and Transfer in Photoelectrochemical Water Splitting

This chapter is based on a manuscript by Alexander Müller, Ilina Kondofersky, Alena Folger, Dina Fattakhova-Rohlfing, Thomas Bein and Christina Scheu, which is to be submitted.

6.1. Introduction

Driven by climate change, rapid population growth and dwindling resources, research into alternative, sustainable energies is thriving. Solar cells and wind turbines, which harness the power of the sun, already play a major role in the energy mix of some countries, with their market share expected to increase. However, storage of the generated electricity is a challenge. One of many possible solutions is photoelectrochemical water splitting, which uses sun light as an energy source to generate oxygen and hydrogen from water. While suitable photoelectrode materials have been studied since 1972[1], research has intensified in the last few years and several photocathode and photoanode materials (such as TiO_2, Si or Cu_2O and Fe_2O_3, WO_3 or $BiVO_4$, respectively) have been investigated.[2–4] Efficient photoanodes, in particular, are difficult to realize. Producing one oxygen molecule requires four holes, making recombination likely and requiring significant optimization of factors such as composition, electronic structure and morphology. All efforts notwithstanding, it is becoming more and more obvious that limitations intrinsic to many single absorber materials investigated so far, such as large band gaps, slow surface kinetics or fast bulk electron-hole recombination, are difficult to overcome. One approach towards solving this problem is the combination of different photoabsorber materials. Such a combination can increase the efficiency in several ways such as by optical absorption enhancement, enhanced charge separation, faster surface kinetics, or the modification of the electronic structure of the interface between both materials.[5] For photoanodes, a dual absorber approach has, for one reason or another, been successful for several systems such as WO_3/TiO_2[6], $WO_3/BiVO_4$[7], TiO_2/Fe_2O_3[8] and Fe_2O_3/WO_3[5].

The Fe_2O_3/WO_3 system is a good model and a promising photoanode for many reasons. The individual materials are abundant and therefore cheap, non-toxic and corrosion-resistant.[9,10] Consequently, both materials have been intensively studied, and the influence of different morphologies, dopants, surface modifications etc. for both systems is well-investigated.[9,11] WO_3 has a band gap of 2.5-2.8 eV and absorbs mostly in the blue and UV spectral range.[10,12,13] Because of good charge transport properties and fast surface kinetics, it has proven itself a

suitable candidate for water photoelectrolysis.[13] However, the large band gap limits the overall theoretical solar-to-hydrogen efficiency to 8 %.[14] Fe_2O_3, on the other hand, has a band gap between 1.9 and 2.2 eV and also absorbs a large fraction of visible light, driving the potential solar-to-hydrogen efficiency up to 16.8 %.[9,14] Unfortunately, the expected efficiency is greatly reduced by several loss mechanisms such as high bulk and surface recombination rates and slow kinetics for the oxygen evolution reaction. Combining Fe_2O_3 and WO_3 can improve the performance of the individual materials in several ways. Compared to bare WO_3, a larger spectral range is absorbed. The band alignment of Fe_2O_3 and WO_3 allows for the injection of electrons from Fe_2O_3 into WO_3, with the latter being a better electron conductor.[15] Sivula *et al.* found the deposition of Fe_2O_3 onto WO_3 scaffolds to drastically improve electron charge collection.[16] Furthermore, the rate of the oxygen evolution reaction of Fe_2O_3 was shown to be significantly improved by surface treatment of Fe_2O_3 by a WO_3 layer.[5,17]

In addition to the strategies discussed above, nanostructuring is commonly employed to improve photoelectrodes.[18,19] Several morphologies have so far been synthesized in the Fe_2O_3/WO_3 system, including flat and porous films,[20–24] host-guest architectures,[16] and nanowires.[5,25] Here, we systematically employed WO_3 both as a scaffold and as a surface treatment, allowing correlation between morphology and performance. Mesoporous Sn-doped Fe_2O_3 photoabsorber layers were prepared by a sol-gel approach and deposited onto a continuous, macroporous WO_3 scaffold.[26] The performance was increased even further by depositing a WO_3 surface layer and increasing the Fe_2O_3/WO_3 interfacial area, thus reaching photocurrents of up to 0.7 mA/cm^2 at 1.23 V vs. the reversible hydrogen electrode (RHE). The viability of this host-guest approach was confirmed by comparing the macroporous photoanodes to mesoporous reference samples.[16,25,27–31] As WO_3 only absorbs a small fraction of blue light, whereas hematite strongly absorbs in this region, measuring photocurrent transients under UV and under blue light illumination allowed for a more nuanced discussion of the impact of the morphology on the photoelectrochemical performance and gave further insights into a complex interplay of several effects.

6.2. Materials and Methods

6.2.1. Synthesis and Deposition of Polymethylmethacrylate (PMMA) Spheres

Polymethylmethacrylate (PMMA) spheres were synthesized according to a well-established procedure.[27,32,33] In brief, sodium dodecylsulfate (5 mg, 0.02 mmol) was added to deoxygenated water (98 ml) under nitrogen purging at 40 °C. Further, methylmethacrylate (MMA) (35.6 g, 0.35 mol) was added to the solution which was subsequently heated to 70 °C for 1 hour under reflux and vigorous stirring. Potassium peroxydisulfate (56 mg, 0.2 mmol) was dissolved in water (2 mL) and added as a polymerization initiator. The polymerization reaction was stopped after 45 min by cooling the suspension to room temperature under continuous stirring. The resulting 300 nm PMMA spheres were washed twice with water by centrifugation (19,000 rpm, 20 min) and dispersed in water.

PMMA spheres were deposited on fluorine-doped tin oxide (FTO) substrates (TEC 15 Glass, Dyesol) by placing the substrates vertically in an aqueous PMMA solution. The solution along with the substrates was placed in an 80 °C oven until the water had evaporated, resulting in opaline PMMA films on FTO.

6.2.2. Preparation of WO_3 Films

The precursor solution for WO_3 was prepared by adding 0.8 g of $(NH_4)_6H_2W_{12}O_{40} \cdot xH_2O$ to 3 mL of deionized water (Millipore Q). To create flat layers, this solution was dip-coated onto the FTO substrate under ambient conditions at a rate of 38 mm/min. The samples were subsequently calcined at 500 °C with a ramp of 3 °C/min and a dwell time of 5 h. By applying the same procedure to PMMA or hematite films, macroporous inverse opal scaffolds and overlayers, respectively, could be prepared.

6.2.3. Synthesis and Deposition of Tin-Doped Hematite

A procedure developed by Dunn *et al.*[26] was applied for the synthesis of tin-doped hematite. 0.25 g Pluronic® P123 were dissolved in 10 mL *tert*-butanol under vigorous stirring. 0.1106 g (0.3 mmol) $Sn(CH_3COO)_4$ were added to the solution and stirred for 5 h. Next, $Fe(NO_3)_3 \cdot 9H_2O$ (0.505 g, 1.25 mmol) was added at room temperature and sonicated for 15 min. 2.5 mL water were then added and the solution was left to stir for 17 h under ambient conditions. Prior to spin coating, the resulting suspension was filtered through a filter with a pore diameter of 200 nm. The electrodes were prepared by depositing the filtered solution (100 µL) onto FTO or the macroporous scaffold, respectively, by spin coating at 1000 rpm for 30 s. The films were then calcined at 600 °C with a ramp of 3 °C/min and a dwell time of 30 min.

6.2.4. Crystallographic and Morphological Characterization

Powder X-ray diffraction (XRD) patterns were acquired on a STOE powder diffractometer (Cu-Kα1, λ = 1.5406 Å) equipped with a position-sensitive Mythen-1K detector in transmission geometry.

Scanning electron microscopy (SEM) measurements were performed on a Zeiss Auriga scanning electron microscope with a field emission gun operated at 4 kV and equipped with an EDAX solid state energy-dispersive X-ray (EDX) spectroscopy detector.

Morphology, crystallography and elemental distribution were investigated using a probe-corrected FEI Titan Themis transmission electron microscope (TEM) with an extreme field emission gun operating at 300 kV. Scanning TEM (STEM) images were acquired with an annular dark-field (ADF) detector and the distribution of Fe_2O_3 and WO_3 was mapped by

collecting EDX spectra in STEM with four Super-X Bruker solid state detectors. Samples in cross-sectional geometry were prepared following a procedure developed by Strecker *et al.*[34]

6.2.5. Optical Characterization

UV-Vis spectra were measured under illumination through the substrate on a Perkin Elmer Lambda 1050 UV/Visible/NIR spectrophotometer with an integrating sphere. The absorbance of the films was calculated by measuring both transmittance and reflectance and correcting for the absorbance of the FTO substrate using an expression derived by Klahr *et al*.[35]

6.2.6. Photoelectrochemical Characterization

Current-voltage (CV) and incident photon-to-current efficiency (IPCE) curves were measured with a μ-Autolab III potentiostat with a FRA2 impedance analyzer. All but an area of 0.2 cm^2 was masked with a Teflon-coated glass fiber adhesive tape. The sample was placed into a quartz cell filled with an aqueous 0.1 M NaOH electrolyte and connected, with an Ag/AgCl reference electrode and a Pt mesh counter electrode, to the potentiostat. To obtain CV curves, the films were illuminated through the substrate by an AM 1.5 solar simulator (Solar Light Model 16S) at 100 mW cm^{-2} by scanning from negative to positive potentials in the dark or under illumination at a sweep rate of 20 mV/s.

IPCE measurements were performed under monochromatic light chopped with a frequency of 1 Hz. Samples were illuminated through the substrate by a 150 W Xenon lamp equipped with a monochromator and order-sorting filters. All IPCE values were measured at a sample bias of 1.23 V vs. RHE under simulated solar irradiation. The light intensity at the electrode was determined using a certified, KG5-filtered Fraunhofer ISE silicon reference cell.

Photocurrent transient data were acquired with a 365 nm or a 455 nm light-emitting diode and a chopping frequency of 2 Hz at an applied potential of 1.23 V vs. RHE. Transfer efficiencies were calculated as the ratio of the steady-state and the initial photocurrent density. As transfer efficiencies measured with 365 nm light did not deviate by more than ± 2 % from those measured with 455 nm light and are effectively independent of the illumination wavelength, the transfer efficiencies averaged over both wavelengths will be discussed.

6.3. Results and Discussion

Two series of samples were prepared via sol-gel synthesis procedures (Figure 6-1).

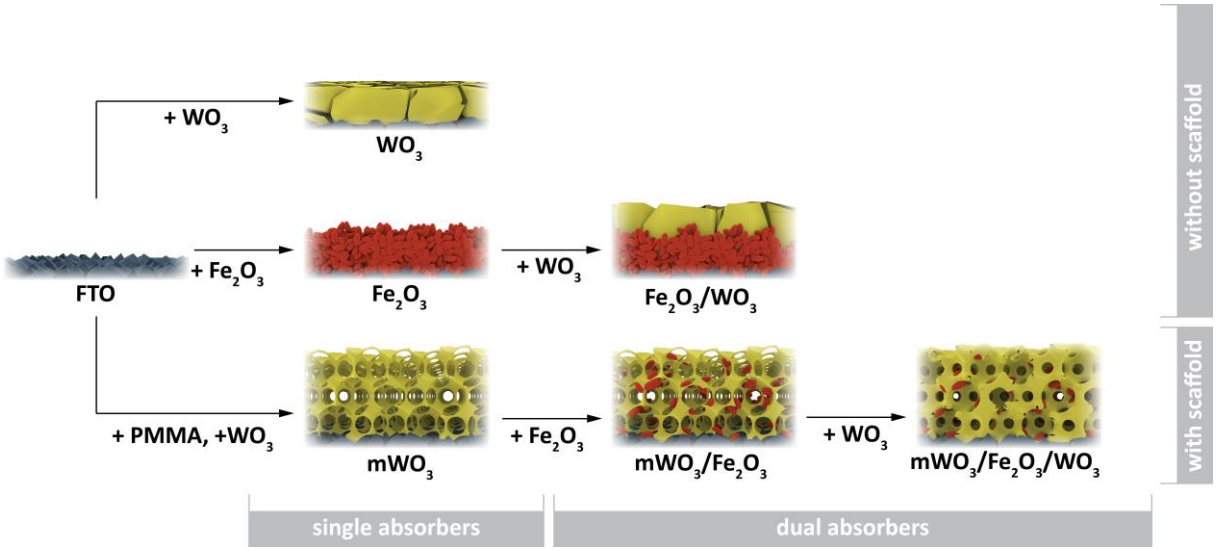

Figure 6-1: Schematic showing the synthesis procedures for all samples.

The first series of flat layers served as references to the host-guest electrodes and allowed analyzing performance-enhancing factors on simpler model systems. The model systems comprised three samples, including a compact WO_3 and a mesoporous Fe_2O_3:Sn layer coated onto FTO as well as a dual absorber photoelectrode prepared by depositing a WO_3 overlayer onto a Fe_2O_3:Sn film. These samples are labeled "WO_3", "Fe_2O_3" and "Fe_2O_3/WO_3", respectively. The second series demonstrated the performance-enhancing benefits of the host-guest architecture. A macroporous WO_3 scaffold was infiltrated by Fe_2O_3:Sn and coated with an additional WO_3 overlayer. In the remainder of the text, these samples are labeled "mWO_3", "mWO_3/Fe_2O_3", and "$mWO_3/Fe_2O_3/WO_3$", respectively. It should be noted that WO_3 can potentially fulfill several functions. At wavelengths below the optical absorption limit, WO_3 acts as a photoabsorber. Furthermore, due to favorable band alignment, it can act as a majority charge carrier collector of electrons generated in Fe_2O_3.[16] Finally, WO_3 can act as a surface treatment to Fe_2O_3 photoanodes, suppressing electron-hole recombination on the surface.[5] Therefore, the samples in this study were prepared so that these possible performance-enhancing effects could be studied.

XRD patterns confirmed the successful synthesis of phase-pure Fe_2O_3:Sn in the hematite structure and monoclinic WO_3 (Figure SI 6-1).[36,37] Contaminant phases could not be detected by XRD, SEM or TEM. In accordance with previous work by Dunn *et al.*, cross-sectional analysis of mesoporous Fe_2O_3 layers showed ~ 50 nm thick mesoporous films composed of individual nanoparticles with an average size of ~ 40 nm x 80 nm (Figure 6-2b and c).[26] WO_3, in contrast, forms ~ 100 nm thick, cracked layers composed of large, compact platelets sized between a few hundred nanometers to a few micrometers (Figure SI 6-2). The Fe_2O_3/WO_3 dual absorber

retains these morphologies, with WO_3 both infiltrating the Fe_2O_3 layer and forming a ~ 50 nm thick layer on top (Figure 6-2a, c and d). By forming a compact top layer, WO_3 decreases the exposed Fe_2O_3 surface area.

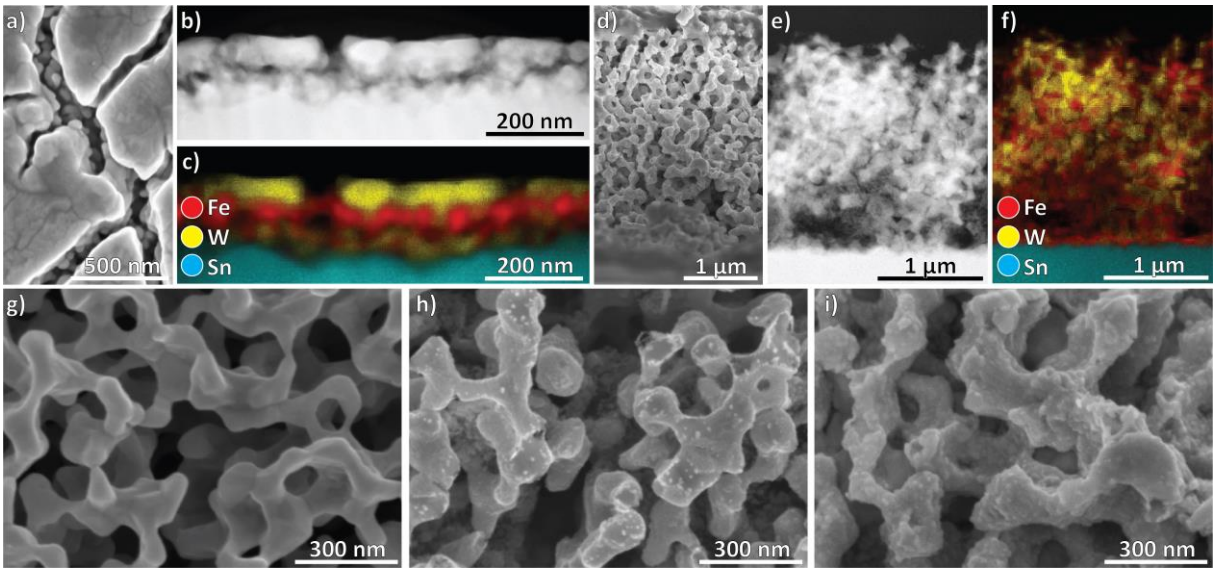

Figure 6-2: Morphological characterization. a) Top-view SEM image of the Fe_2O_3/WO_3 thin films. Fe_2O_3 is visible through cracks in the WO_3 layer. ADF-STEM images and EDX maps of Fe_2O_3/WO_3 are shown in b) and c). d) Cross-section SEM image of $mWO_3/Fe_2O_3/WO_3$. ADF-STEM images and EDX maps of $mWO_3/Fe_2O_3/WO_3$ are shown in e) and f) Compared to the pure WO_3 scaffold shown in g), deposited Fe_2O_3 nanoparticles are clearly seen in h). In i) a SEM image of $mWO_3/Fe_2O_3/WO_3$ is shown. By depositing a WO_3 overlayer, the whole structure is coated.

In contrast, the macroporous samples have an open, porous morphology (Figure 6-2d). The macroporous WO_3 scaffold forms a ~ 2.5 µm thick layer with ~ 150 nm wide pores (Figure 6-2g). Even though the scaffold is distorted compared to a perfect inverse opal structure, it is continuous and reaches the back contact. This is expected to be beneficial for charge transport. Hematite nanoparticles fully infiltrate the scaffold and are homogenously distributed throughout the whole film (Figure 6-2e and f). An additional thin layer of Fe_2O_3 nanoparticles forms on the FTO substrate (Figure 6-2f). In contrast to the flat layers, a WO_3 overlayer fully infiltrates the scaffold and thinly coats WO_3 scaffold and Fe_2O_3 nanoparticles alike without top layer formation (Figure 6-2i).

The crystal structures of the materials were investigated by TEM. Monocrystallinity of the hematite nanoparticles has been shown by Dunn *et al*.[26] Both the WO_3 scaffold and the WO_3 overlayer are highly crystalline, with mWO_3 having domains of several hundred nanometers in size (Figure 6-3a and b). In both Fe_2O_3/WO_3 and mWO_3/Fe_2O_3, an abrupt interface between Fe_2O_3 and WO_3 without a specific orientation relationship or amorphous phases was found (Figure 6-3c).

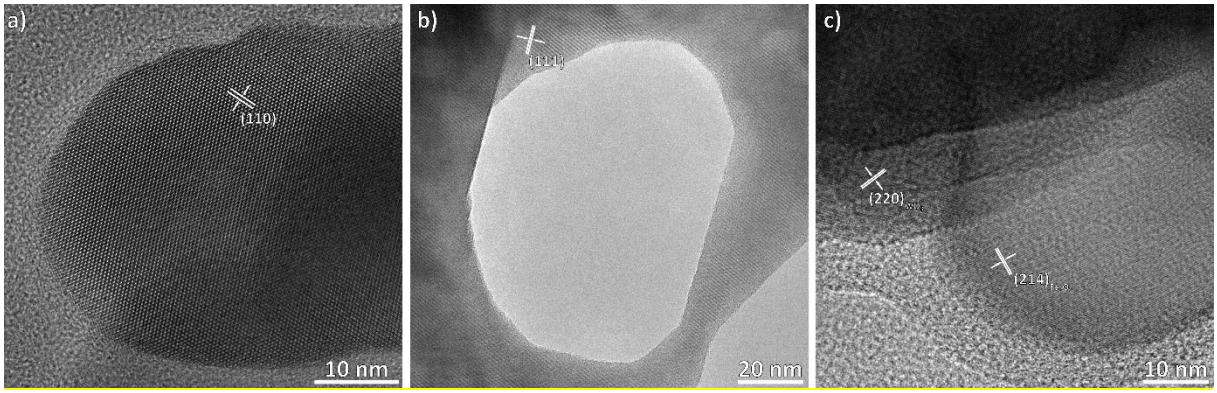

Figure 6-3: Investigation of the crystal structures of a) the WO_3 overlayer in Fe_2O_3/WO_3 and b) the WO_3 scaffold. c) Interface between Fe_2O_3 and WO_3.

*Light absorption of all samples was assessed with UV-Vis measurements (*Figure 6-4*). To correlate them with photoelectrochemical measurements, they were measured under substrate illumination.*

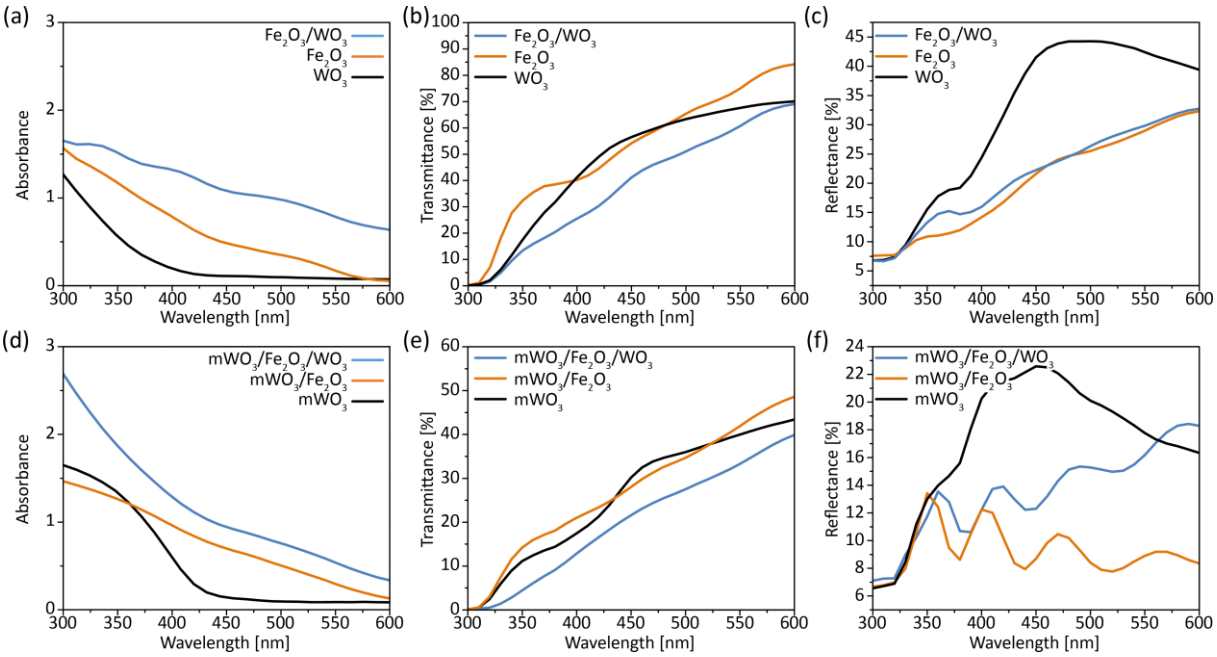

Figure 6-4: UV-Vis, reflectance and transmittance spectra of mesoporous (a, b and c) and macroporous (d, e and f) samples.

*As expected based on the band gap, bare WO_3 only absorbs light up to a wavelength of ~ 425 nm. In comparison, Fe_2O_3 absorbs light up to a wavelength of ~ 560 nm, consistent with a band gap of 2.2 eV, and thereby a much larger percentage of the solar spectrum. Of the flat layers, Fe_2O_3 absorbs more light than WO_3 throughout the whole spectral range. In both flat and macroporous samples, more light is absorbed upon deposition of a mesoporous Fe_2O_3:Sn layer or a WO_3 overlayer. Notable is the strong scattering contribution of both compact and macroporous WO_3, which is reduced for all dual absorbers (*Figure 6-4*c and f). As the UV-Vis*

spectra were acquired under substrate illumination, light must be backscattered by WO_3 and absorbed by the Fe_2O_3 layer. WO_3 thereby acts as a reflective layer and leads to significantly increased absorbance in the visible range.

All samples were photoelectrochemically characterized by CV measurements under AM 1.5 illumination and IPCE measurements (Figure 6-5). Among the flat layers, Fe_2O_3 has a higher current density than WO_3, which can be explained by increased light harvesting in the visible region. In accordance with the drop in light absorbance seen in the UV-Vis spectra, the IPCE spectrum of bare WO_3 drops to 0 % at *~ 425 nm, whereas the IPCE spectrum of Fe_2O_3 drops to 0 % at a much longer wavelength of ~ 560 nm.* Depositing a WO_3 layer onto Fe_2O_3, thus creating a dual absorber, increases the current density threefold compared to Fe_2O_3 and 17-fold compared to WO_3, with currents of 0.23 mA/cm^2 at 1.23 V vs. RHE and a maximum IPCE of up to 13 % at 340 nm. This dual absorber not only outperforms the single components, but also the sum of current densities obtained from the individual absorber layers, suggesting that the increased performance cannot be explained solely by increased light absorption. Another important feature of the dual absorber photoanodes is a cathodic shift of the onset potential by nearly 200 mV. Such a shift is usually attributed to the reduction of loss pathways due to either charge transfer catalysis or suppression of surface recombination.[38–40]

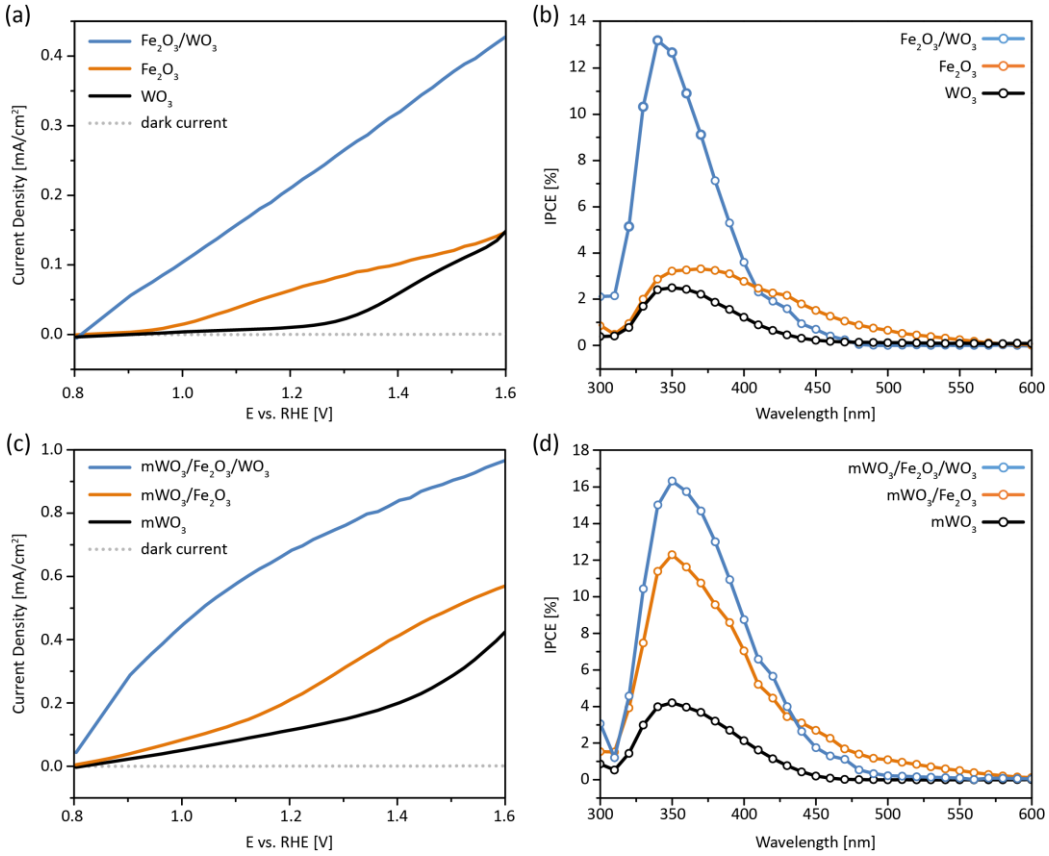

Figure 6-5: CV and IPCE measurements of flat (a and b) and macroporous layers (c and d) measured under AM 1.5 illumination.

The macroporous films show trends similar to the flat layer model systems (Figure 6-5). The performance of the macroporous WO_3 scaffolds is strongly increased compared to WO_3 flat layers. As shown by UV/Vis measurements, the deposition of Fe_2O_3 leads to increased light absorption in the visible range and a shift of the IPCE curve, increasing the current density up to 0.24 mA/cm^2 at 1.23 V vs. RHE. A substantial performance increase to 0.7 mA/cm^2 at 1.23 V vs. RHE with a maximum IPCE of 17 % at 350 nm is achieved by depositing an additional WO_3 layer. As for Fe_2O_3/WO_3, CV measurements of $mWO_3/Fe_2O_3/WO_3$ show a steep current onset at 0.8 V vs. RHE. mWO_3/Fe_2O_3, which is also composed of both materials, does not show such a steep onset. The strong performance increase compared to flat layers could be explained by the increase in porosity and therefore surface area, or by the WO_3 scaffold acting as a current collector as described in the literature.[16,27] Of note is the strong performance increase when applying WO_3 as a surface layer compared to having it as a scaffold. Interface-related effects such as suppressed recombination due to the WO_3 surface layer could therefore play a major role. Another possible explanation is the role of WO_3 as a scattering layer, thereby increasing the light harvesting efficiency of Fe_2O_3.

The photocurrents discussed so far were measured under AM 1.5 illumination. However, given the band structures of Fe_2O_3 and WO_3 and based on our UV/Vis measurements, different processes are expected to take place under illumination with UV and with visible light (Figure SI 6-3).[15] Under UV illumination, electrons generated in Fe_2O_3 can be injected into WO_3 and holes generated in WO_3 can be injected into Fe_2O_3 (Figure 6-6a). Light of a longer wavelength, however, only generates electron-hole pairs in Fe_2O_3, of which the electrons can, according to the band diagram, be injected into WO_3 (Figure SI 6-3). To gain further insight into the behavior of the dual absorber system, photocurrent transients were measured under chopped illumination with UV (365 nm) and blue (455 nm) light. Due to increased light absorption by both Fe_2O_3 and WO_3 in the UV region, steady-state photocurrents acquired under UV illumination are consistently higher than those measured with blue light (Figure 6-6b). WO_3 is a highly efficient photocatalyst, leading to higher photocurrents than Fe_2O_3 under UV illumination.[13] Blue light, however, is not absorbed by WO_3 *(*Figure 6-4*)* and higher photocurrents are reached with Fe_2O_3.

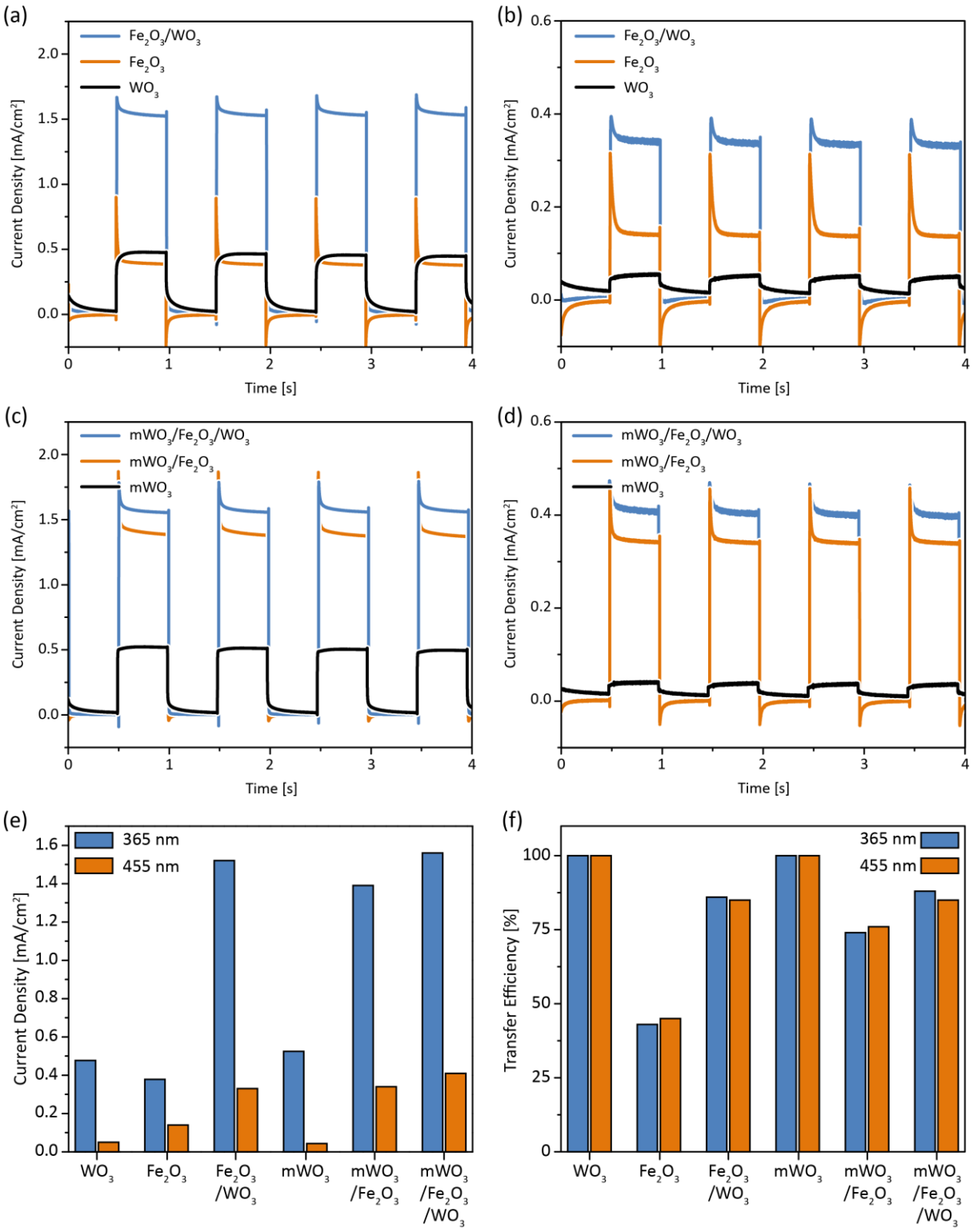

Figure 6-6: Photocurrent transients of flat layers under (a) UV (365 nm) and (b) blue (455 nm) illumination at an applied potential of 1.23 V vs. RHE. Photocurrent transients of the macroporous layers under 365 nm and 455 nm illumination are shown in (c) and (d), respectively. e) Steady-state photocurrent densities under illumination with 365 nm and 455 nm light at a potential of 1.23 V vs. RHE. f) Transfer efficiencies under illumination with 365 nm and 455 nm light extracted from photocurrent transients measured at 1.23 V ca. RHE.

Photocurrent transients reflect all processes influencing charge transfer and transport in the electrode (Figure 6-6).[26,41] Upon illumination, movement of photo-generated holes to the surface leads to a charging or displacement current. If holes accumulate, either due to slow surface kinetics or due to slow electron transport to the back contact, they recombine with electrons, and the initial photocurrent decays to a lower steady-state photocurrent. For Fe_2O_3, this leads to a characteristic "spike and overshoot" photocurrent, whereas fast surface kinetics and good electron conductivity of pure WO_3 lead to a rectangular transient form suggestive of complete charge carrier extraction.[41] By depositing Fe_2O_3 on a WO_3 scaffold, the difference between initial and steady-state photocurrent decreases compared to Fe_2O_3 and deposition of an additional WO_3 layer further brings the shape of the photocurrent transient even closer to a rectangle. As is to be expected from the fast surface kinetics and good charge transport properties the material is known for, both WO_3 and mWO_3 have transfer efficiencies of 100 %.[13] In comparison, pure Sn-doped Fe_2O_3 has a transfer efficiency of 41 %, confirming previous work by Dunn *et al*.[26] The transfer efficiency can be improved to 75 % by depositing the Sn-doped Fe_2O_3 layer onto a WO_3 scaffold. In line with discussion in the literature, the WO_3 scaffold could act as a charge collector and thereby increase the electron diffusion length.[16,27] In comparison, surface treatment by the deposition of an additional WO_3 layer has a greater effect on the transfer efficiency than the introduction of a WO_3 scaffold and increases the transfer efficiency to 85 and 88 % for flat Fe_2O_3/WO_3 and macroporous $mWO_3/Fe_2O_3/WO_3$, respectively. The improved performance could stem from an enhanced rate of Faradaic reactions on the interface due to the surface treatment with WO_3. However, additional studies are needed to elucidate the mechanism behind this effect.

For both illumination wavelengths, photocurrent densities reached by the dual absorbers, regardless of whether WO_3 was applied as a surface layer or as a scaffold, are very similar. This is in contrast to measurements under the full AM 1.5 solar spectrum, where a much larger difference in photocurrent densities was observed for the different morphologies. This could potentially be explained by the complex interplay of several factors, such as faster surface kinetics, improved current collection and enhanced light absorption, in which WO_3 influences Fe_2O_3. However, future studies will be necessary to fully understand this effect.

6.4. Conclusion

To analyze the effects of WO_3 on Fe_2O_3 in photoelectrochemical water splitting, dual absorbers were prepared with WO_3 as a scaffold and/or as a surface layer. Both approaches significantly increased the performance, validating both the host-guest approach and the surface layer concept. By combining them, current densities of 0.7 mA/cm^2 at 1.23 V vs. RHE under AM 1.5 illumination with an IPCE of 17 % at 350 nm were reached. The performance increases were investigated by CV, IPCE, photocurrent transient and UV-Vis measurements and we could identify several beneficial effects responsible for improved charge carrier generation and transport. Importantly, WO_3 strongly reflects visible light, which is then absorbed by Fe_2O_3, resulting in higher photocurrents. The dual absorber therefore exhibits

significantly increased light absorption. Compared to Fe_2O_3, a cathodic shift of the onset potential from 1.0 to 0.8 V and an increase in transfer efficiencies, reaching up to 88 %, were measured. We conclude that the investigated device architecture is a promising approach for the design of Fe_2O_3/WO_3 dual absorber photoanodes by combining different beneficial effects to generate substantially improved devices.

6.5. Acknowledgements

The work was supported by the German Research Foundation (DFG) via the priority program SPP 1613, the Nanosystems Initiative Munich (NIM) and LMUexcellent, the Bavarian research network "Solar Technologies Go Hybrid", and the Center for Nanoscience (CeNS). We thank the students Zachary Edelen and Marina Polo Collado for participating in the research. Steffen Schmidt and Halina Dunn are gratefully acknowledged for insightful discussions.

6.6. Supporting Information

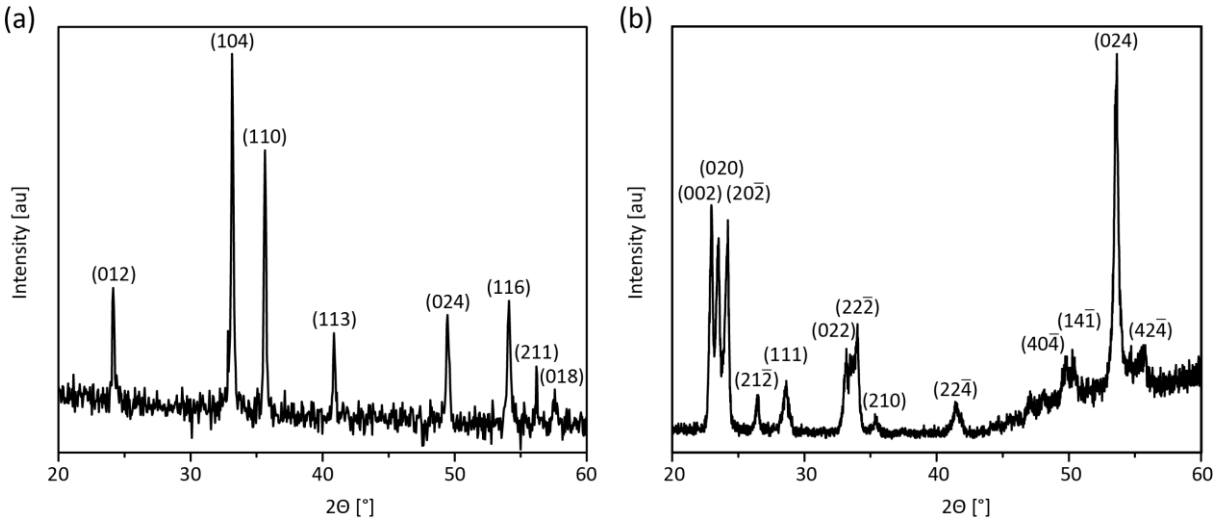

Figure SI 6-1: XRD diffractograms of a) Fe_2O_3 and b) WO_3. The reflections were assigned using references 34 and 35.

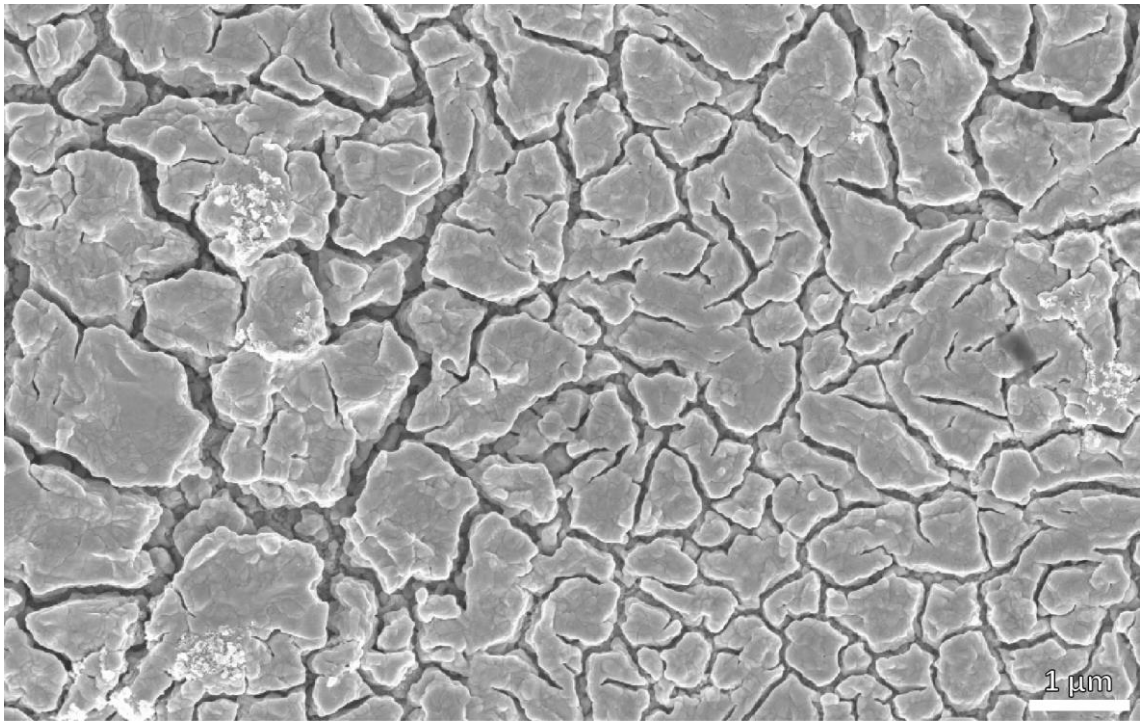

Figure SI 6-2: Top-view image of a WO_3 layer, showing the differently sized platelets.

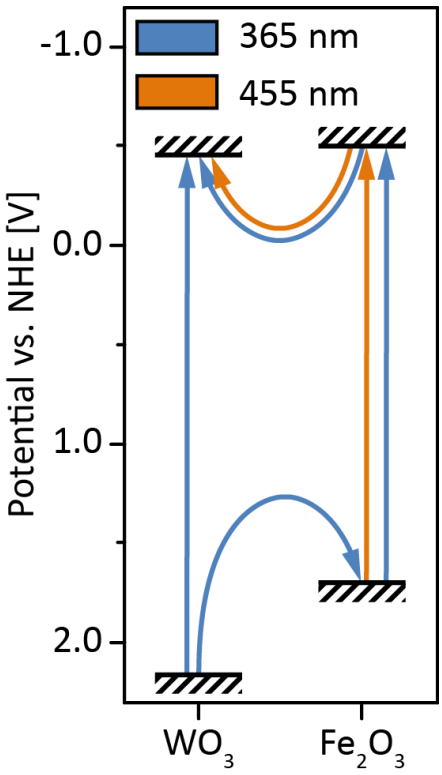

Figure SI 6-3: a) Simplified band structure of WO_3 and Fe_2O_3 showing the processes taking place under UV (365 nm) and under blue (455 nm) light according to reference 15.

6.7. References

(1) Fujishima, A.; Honda, K. *Nature* **1972**, *238* (5358), 37.

(2) Grätzel, M. *Nature* **2001**, *414* (6861), 338.

(3) Hisatomi, T.; Kubota, J.; Domen, K. *Chem. Soc. Rev.* **2014**, *43* (22), 7520.

(4) Li, Z.; Luo, W.; Zhang, M.; Feng, J.; Zou, Z. *Energy Environ. Sci.* **2013**, *6* (2), 347.

(5) Kronawitter, C. X.; Vayssieres, L.; Shen, S.; Guo, L.; Wheeler, D. A.; Zhang, J. Z.; Antoun, B. R.; Mao, S. S. *Energy Environ. Sci.* **2011**, *4* (10), 3889.

(6) Wang, J.; Han, Y.; Feng, M.; Chen, J.; Li, X.; Zhang, S. *J. Mater. Sci.* **2011**, *46* (2), 416.

(7) Su, J.; Guo, L.; Bao, N.; Grimes, C. a. *Nano Lett.* **2011**, *11* (5), 1928.

(8) Luan, P.; Xie, M.; Liu, D.; Fu, X.; Jing, L. *Sci. Rep.* **2014**, *4*, 1.

(9) Sivula, K.; Le Formal, F.; Grätzel, M. *ChemSusChem* **2011**, *4* (4), 432.

(10) Hodes, G.; Cahen, D.; Manassen, J. *Nature* **1976**, *260* (5549), 312.

(11) Liu, X.; Wang, F.; Wang, Q. *Phys. Chem. Chem. Phys.* **2012**, *14* (22), 7894.

(12) Granqvist, C. G. *Sol. Energy Mater. Sol. Cells* **2000**, *60* (3), 201.

(13) Santato, C.; Ulmann, M.; Augustyński, J. *J. Phys. Chem. B* **2001**, *105* (5), 936.

(14) Murphy, A. B.; Barnes, P. R. F.; Randeniya, L. K.; Plumb, I. C.; Grey, I. E.; Horne, M. D.; Glasscock, J. A. *Int. J. Hydrogen Energy* **2006**, *31* (14), 1999.

(15) van de Krol, R.; Liang, Y.; Schoonman, J. *J. Mater. Chem.* **2008**, *18* (20), 2311.

(16) Sivula, K.; Formal, F. Le; Grätzel, M. *Chem. Mater.* **2009**, *21* (13), 2862.

(17) Kishi, T.; Aritsuka, M. *Surf. Coatings Technol.* **1988**, *34* (3), 345.

(18) Osterloh, F. E. *Chem. Soc. Rev.* **2013**, *42* (6), 2294.

(19) Zhang, P.; Gao, L.; Song, X.; Sun, J. *Adv. Mater.* **2015**, *27* (3), 562.

(20) Luo, W.; Yu, T.; Wang, Y.; Li, Z.; Ye, J.; Zou, Z. *J. Phys. D. Appl. Phys.* **2007**, *40* (4), 1091.

(21) Memar, A.; Daud, W. R. W.; Hosseini, S.; Eftekhari, E.; Minggu, L. J. *Sol. Energy* **2010**, *84* (8), 1538.

(22) Hosseini, S.; Eftekhari, E.; Masoudi Soltani, S.; Memar, A.; Eghbali Babadi, F.; Dastorian Jamnani, B.; Ismail, M. H. S.; Jeffery Minggu, L. *J. Environ. Chem. Eng.* **2013**, *1* (4), 1309.

(23) Hosseini, S.; Eftekhari, E.; Masoudi Soltani, S.; Babadi, F. E.; Minggu, L. J.; Ismail, M. H. S. *Appl. Surf. Sci.* **2014**, *289*, 53.

(24) Mao, A.; Kim, J. K.; Shin, K.; Wang, D. H.; Yoo, P. J.; Han, G. Y.; Park, J. H. *J. Power Sources* **2012**, *210*, 32.

(25) Jin, T.; Diao, P.; Wu, Q.; Xu, D.; Hu, D.; Xie, Y.; Zhang, M. *Appl. Catal. B Environ.* **2014**, *148-149*, 304.

(26) Dunn, H. K.; Feckl, J. M.; Müller, A.; Fattakhova-Rohlfing, D.; Morehead, S. G.; Roos, J.; Peter, L. M. P.; Scheu, C.; Bein, T. *Phys. Chem. Chem. Phys.* **2014**, *16* (44), 24610.

(27) Kondofersky, I.; Dunn, H. K.; Müller, A.; Mandlmeier, B.; Feckl, J. M.; Fattakhova-Rohlfing, D.; Scheu, C.; Peter, L. M.; Bein, T. *ACS Appl. Mater. Interfaces* **2015**, *7*, 4623.

(28) Riha, S. C.; Devries Vermeer, M. J.; Pellin, M. J.; Hupp, J. T.; Martinson, A. B. F. *ACS Appl. Mater. Interfaces* **2013**, *5* (2), 360.

(29) Sun, Y.; Chemelewski, W. D.; Berglund, S. P.; Li, C.; He, H.; Shi, G.; Mullins, C. B. *ACS Appl. Mater. Interfaces* **2014**, *6* (8), 5494.

(30) Wang, L.; Palacios-Padrós, A.; Kirchgeorg, R.; Tighineanu, A.; Schmuki, P. *ChemSusChem* **2014**, *7* (2), 421.
(31) Tsui, K.; Zhang, Y.; Yang, S.; Fan, Z. *Nano Lett.* **2014**, *14*, 2123.
(32) Mandlmeier, B.; Minar, N. K.; Feckl, J. M.; Fattakhova-Rohlfing, D.; Bein, T. *J. Mater. Chem. A* **2014**, *2* (18), 6504.
(33) Liu, Y.; Peters, K.; Mandlmeier, B.; Müller, A.; Fominykh, K.; Rathousky, J.; Scheu, C.; Fattakhova-Rohlfing, D. *Electrochim. Acta* **2014**, *140*, 108.
(34) Strecker, A.; Salzberger, U.; Mayer, J. *Prakt. Metallogr.* **1993**, *30* (10), 482.
(35) Klahr, B. M.; Martinson, A. B. F.; Hamann, T. W. *Langmuir* **2011**, *27* (1), 461.
(36) Maslen, E. N.; Streltsov, V. a.; Streltsova, N. R.; Ishizawa, N. *Acta Crystallogr. Sect. B* **1994**, *50* (1903), 435.
(37) Tanisaki, S. *J. Phys. Soc. Japan* **1960**, *15* (4), 573.
(38) Hisatomi, T.; Le Formal, F.; Cornuz, M.; Brillet, J.; Tétreault, N.; Sivula, K.; Grätzel, M. *Energy Environ. Sci.* **2011**, *4* (7), 2512.
(39) Tilley, S. D.; Cornuz, M.; Sivula, K.; Grätzel, M. *Angew. Chemie - Int. Ed.* **2010**, *122*, 6549.
(40) Zhong, D. K.; Sun, J.; Inumaru, H.; Gamelin, D. R. *J. Am. Chem. Soc.* **2009**, *131*, 6086.
(41) Peter, L. M.; Wijayantha, K. G. U.; Tahir, A. A. *Faraday Discuss.* **2012**, *155* (0), 309.

7. Nanostructured Ternary FeCrAl Oxide Photocathodes for Water Photoelectrolysis

This chapter is based on a manuscript by Ilina Kondofersky, Alexander Müller, Halina K. Dunn, Alesja Ivanova, Goran Štefaníc, Martin Ehrensperger, Christina Scheu, Bruce A. Parkinson, Dina Fattakhova-Rohlfing and Thomas Bein, which is under review.

7.1. Introduction

Solar energy is becoming increasingly important as an abundant and renewable energy source and the photoelectrolysis of water using illuminated semiconductor electrodes is considered an important technology for the generation of hydrogen in a sustainable and efficient way.[1] The most critical issue for the development of photoelectrolysis cells is the development of suitable photoabsorber materials that combine stability and efficient solar light harvesting with fast kinetics of the interfacial water splitting reactions.[2] To date, numerous material systems have been investigated. Among those more intensively studied as photoanode materials are $BiVO_4$[3], α-Fe_2O_3[4], WO_3[5] and TiO_2[6] and, as photocathode materials, p-Si[7], Cu_2O[8] or $CuFeO_2$[9]. However, in spite of significant efforts, the progress towards efficient solar water splitting systems has been slow. The efficiency of all known photoabsorbers is limited by factors such as poor light harvesting, losses caused by inefficient electron-hole pair separation, bulk and interfacial recombination or high overpotentials for the overall water splitting reaction and instability of the photoelectrodes. Consequently, discovering and optimizing novel photoabsorber materials is important for the development of competitive photoelectrochemical cells. This is a very demanding task due to the practically unlimited number of potential material classes and elemental combinations. An extremely powerful approach is offered by high-throughput theoretical[10-11] and experimental[12-18] screening methods. However, the identification of promising materials with specific stochiometrics is only the first step and, aided by characterization and increasing understanding of material properties, synthesis strategies have to be refined to obtain electrodes with optimized compositions and morphologies.

Recently, the Solar Hydrogen Activity research Kit (SHArK) project, a distributed science research project[19] identified a p-type ternary oxide semiconductor containing the earth-abundant and inexpensive elements Fe, Cr and Al. Combinatorial optimization identified the highest photoelectrolysis activity for the hydrogen evolution reaction at a stoichiometry near $Fe_{0.84}Cr_{1.0}Al_{0.16}O_3$. The discovered material features a band gap of 1.8 eV. While the incident

photon-to-charge-carrier efficiency (IPCE) of around 1 x 10^{-4} % at 500 nm is very low, a promising photovoltage of around 0.95 V was reached. Sliozberg *et al*.[20] obtained higher photocurrents of 10 µA cm^{-2} at 0.5 V vs. RHE under AM 1.5 with an IPCE of 0.3 % at 350 nm by depositing thicker films using reactive magnetron co-sputtering, demonstrating that the performance of this material can be improved by employing different fabrication routes.

Inspired by the potential of this recently discovered material, we focused on the development of large-scale photocathode morphologies based on ternary FeCrAl oxides. We report a sol-gel synthesis method that yielded mesoporous thin films with photocurrents of 0.25 mA cm^{-2} at 1.23 V vs RHE. The performance can be improved further by introducing a template and synthesizing a periodic, porous inverse-opal structure. After optimization, a photocurrent of 0.68 mA cm^{-2} under AM 1.5 illumination with an IPCE of 28 % at 400 nm was reached. We also describe extensive structural and electrochemical studies aimed at understanding the correlation between synthesis conditions, structure and photoelectrochemical behavior of the novel material.

7.2. Materials and Methods

7.2.1. Synthesis

Mesoporous FeCrAl oxide layers were prepared by dissolving the precursor salts $Fe(NO_3)_3$*$9H_2O$, $Cr(NO_3)$*$9H_2O$ and $Al(NO_3)_3$*$9H_2O$ in ethanol, resulting in 0.5 M solutions. The precursor solutions were mixed in a ratio of 0.42 : 0.5 : 0.08, respectively, to achieve the targeted composition. This solution was spin coated (800 rpm for 30 s) onto fluorine-doped tin oxide glass, FTO (TEC 15 Glass, Dyesol), resulting in films that were calcined at 525 °C for 1.5 h (2 °C/min heat ramp).

Macroporous films were synthesized by pre-depositing polymethylmethacrylate (PMMA) spheres as a template. PMMA spheres with a diameter of 300 nm were prepared according to a procedure previously described by us[21-22]. In brief, the particles were synthesized by adding methylmethacrylate (MMA) (35.6 g, 0.35 mol) and sodium dodecylsulfate (SDS) (5 mg, 0.02 mmol) to deoxygenated water (98 mL) under nitrogen purging at 40 °C. The resulting emulsion was heated to 70 °C for 1 hour under reflux and vigorous stirring. The polymerization was initiated by adding potassium peroxydisulfate (56 mg, 0.2 mmol) dissolved in water (2 mL) and stopped after 2.5 hours by cooling the suspension to room temperature under atmospheric conditions. The resulting PMMA spheres were washed with water by centrifugation (19000 rpm, 20 min) and redispersed in water.

The FTO substrates were placed vertically in an aqueous PMMA solution (11 wt.-%) and the solution was dried over night at 70 °C. These templated films were infiltrated with the FeCrAl precursor solution via spin coating and calcined at 525 °C for 1.5 h (2 °C/min heat ramp).

7.2.2. Crystallographic and Morphological Characterization

X-ray diffraction analysis (XRD) was carried out on a STOE powder diffractometer (Cu-Kα1, l = 1.5406 Å) equipped with a position-sensitive Mythen-1K detector in transmission geometry. X-ray photoelectron spectroscopy (XPS) measurements of the particles on an FTO substrate were performed using a VSW TA10 X ray source, providing monochromatic Mg-Kα radiation, and a VSW HA100 hemispherical analyzer. The samples were cleaned by Ar^+ sputtering (VSW AS10 ion source) for 8 min at 1 keV. Scanning electron microscopy (SEM) measurements were performed on a JEOL JSM-6500F with a field emission gun run at 5 kV and equipped with an Oxford energy-dispersive X-ray (EDX) detector. A probe-corrected FEI Titan Themis with an X-FEG operated at 300 kV was used for transmission electron microscopic (TEM) investigations. Bright field (BF) and high-resolution TEM (HRTEM) images as well as diffraction patterns were acquired with a Ceta 16M camera, scanning, TEM (STEM) images with a annular dark field (ADF) detector, and energy-dispersive X-ray (EDX) spectra and maps with four Super-X Bruker SDD detectors. Samples were prepared either by scraping material of the substrate with a razor blade and depositing it on a holey carbon grid or in a cross-sectional geometry as described by Strecker *et al.*[23]

Film homogeneity and thickness were measured using a Vecco (Dektak 156) profilometer with a 640x489-pixel camera and a diamond tip (radius 12.5 µm).

7.2.3. Optical Characterization

UV-Vis measurements were performed on a Perkin Elmer Lambda 1050 UV/Visible/NIR spectrophotometer with an integrating sphere. The absorbance of each sample was calculated from experimental reflectance and transmittance measurements and fully corrected for reflectance and absorbance of the FTO substrate using an equation derived by Klahr *et al*.[24]

$$Abs_F = \ln\left(\frac{T_{S+F}/T_S}{1-\frac{R_{S+F}-R_S}{T_S^2}}\right)$$

T_S/T_{S+F} and R_S/R_{S+F} correspond to the wavelength-dependent transmissions and reflections of the plain (T_S *and* R_S) and the coated substrate (T_{S+F} and R_{S+F}), respectively.

7.2.4. Photoelectrochemical Characterization

Photoelectrochemical measurements were carried out using a µ-Autolab III potentiostat equipped with a FRA2 impedance analyzer. The samples were masked with a Teflon-coated glass fiber adhesive tape, leaving an area of 0.2 cm^2 exposed. The sample was placed in a quartz cell filled with an aqueous 0.1 M $HClO_4$ electrolyte and connected in a 3 electrode mode, together

with an Ag/AgCl reference electrode and a Pt mesh counter electrode, to the potentiostat. The films were illuminated through the substrate side using an AM1.5 solar simulator (Solar Light Model 16S) at 100 mW cm^{-2}. Current-voltage (I-V) curves were obtained by scanning from positive to negative potentials in the dark or under illumination at a 20 mV/s sweep rate.

Incident photon-to-current efficiency (IPCE) measurements were performed under low-frequency chopped monochromatic light (1 Hz). A 150 W Xenon lamp equipped with a monochromator and order-sorting filters was used as a light source. The sample bias was set to 0.75 V vs. RHE under simulated solar irradiation. The light intensity reaching the electrode was measured using a certified Fraunhofer ISE silicon reference cell equipped with a KG5 filter.

To estimate the electron transfer efficiency, transient current measurements were performed by illuminating the electrode with a 455 nm light emitting diode. The light was switched on and off every 500 ms and the current was measured at potentials ranging from 1.0 – 0.5 V vs. RHE.

7.3. Results and Discussion

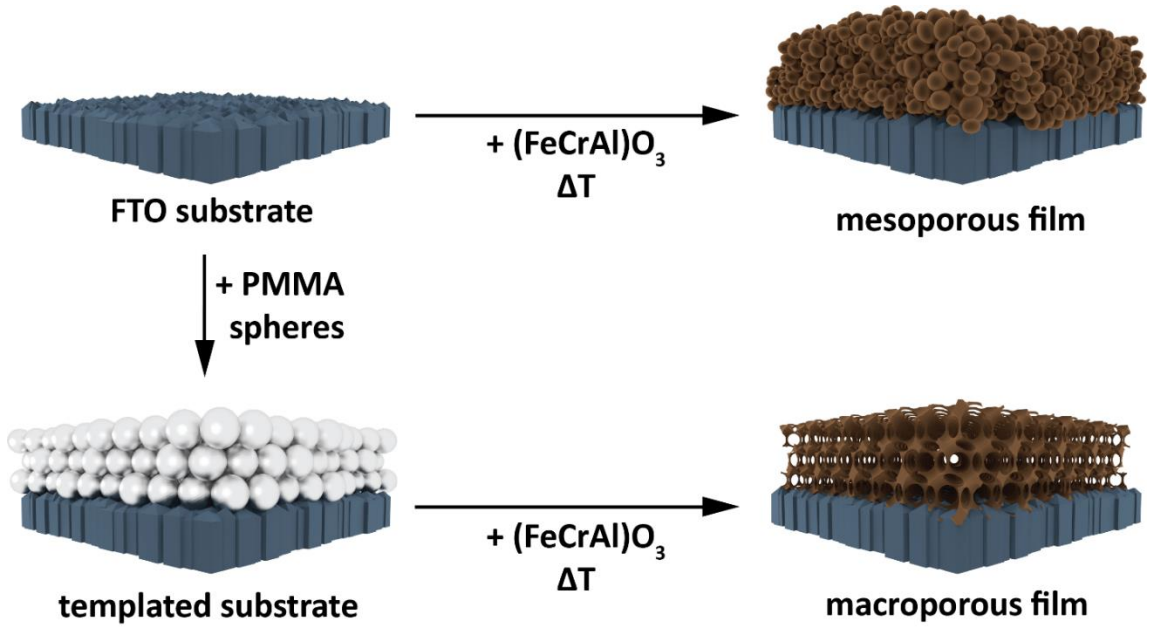

Figure 7-1: Scheme by which mesoporous and macroporous films were synthesized.

FeCrAl oxide photocathodes were synthesized via a sol-gel route (Figure 7-1). Precursor solutions were prepared by dissolving the nitrate salts of Fe^{3+}, Cr^{3+} and Al^{3+} in ethanol in a ratio of 0.43:0.5:0.08. This stoichiometry was discovered via a combinatorial optimization approach and reported to yield the highest IPCE values.[19] The electrodes obtained by spin-coating a freshly prepared precursor solution onto FTO and calcining in air at 525 °C are mesoporous and crack-

free (Figure 7-2a). The film thickness can be varied from 90 to 700 nm by adjusting spin coating speed and time, with the light absorbance scaling linearly with the film thickness (SI Figure 7-4).

X-ray diffraction patterns of the mesoporous films can be indexed by a single phase with the corundum structure and the space group R-3c. Secondary phases with other crystal structure were not found. The lattice parameters were obtained by a Le Bail[25] refinement (SI Figure 7-6) as a = 4.9832(1) Å and c = 13.6143(3) Å. This is in excellent agreement (deviation < 1%) with the lattice parameters obtained by Rowley *et al*.[19]

Although XRD analysis of the powder material points to the formation of a single phase, cross section TEM analysis of the films surprisingly reveals a phase separation. The different phases found in TEM could not be resolved by XRD, indicating that both phases form in the corundum structure and have very similar lattice parameters. This was also confirmed by HRTEM and FFT measurements. Near the FTO substrate, a Cr-rich phase with an average Fe:Cr:Al ratio of (20±4:75±5:5±1) at-% forms columnar grains with a size of up to 250 nm in the corundum structure. Above this region, a mesoporous network of Fe-rich nanoparticles with an average composition of Fe:Cr:Al = (59±7:18±4:23±6) at-% is formed. These, also can be separated into large ellipsoid nanoparticles with a diameter of (5.6±0.8) nm decorated with small spherical nanoparticles with a diameter of (1.5±0.2) nm (SI Figure 7-9). The chemical composition of these particles is slightly different, as the small particles are Al-enriched (Fe:Cr:Al ratio of (71±4:9±4:21±6) at-% whereas the large particles have a Fe:Cr:Al ratio of (76±6:11±2:13±4) at-%).

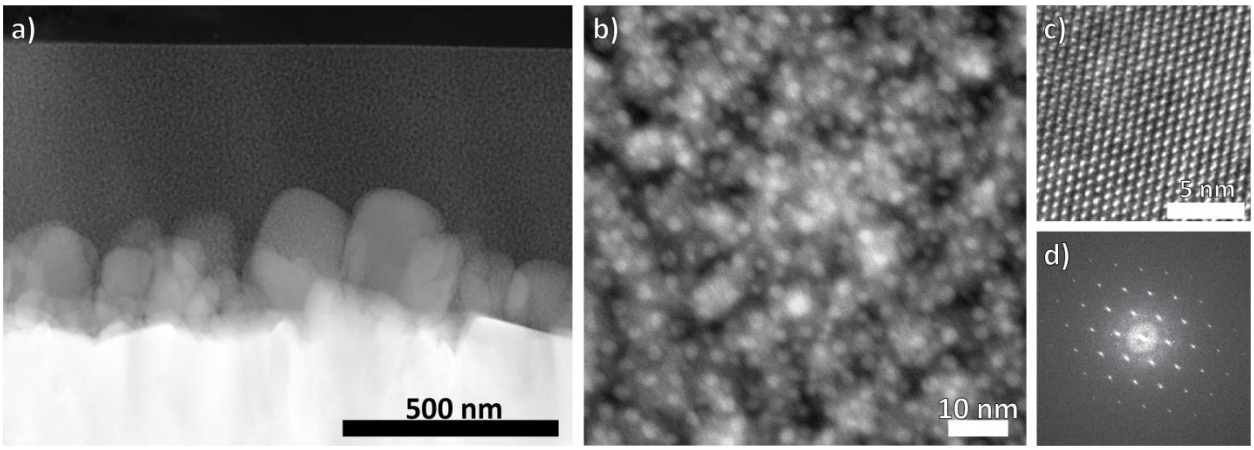

Figure 7-2: TEM images of the mesoporous FeCrAl oxide film. a) shows a cross section overview image, b) an image of the nanoparticles in the Fe-rich region. In c) and d), a HRTEM image and the corresponding FFT of the Cr-rich phase are shown. The image shows the (001) plane.

X-ray photoelectron spectroscopy was used to detect signals of iron, chromium and aluminum of the upper, Fe-rich layer of a 500 nm thick, mesoporous FeCrAl oxide film (Figure 7-3). Peak positions and shapes indicate an oxidation state of +3 for all metal ions. Assignment of the

chemical species was done according to Moulder *et al*.[26] Quantification yielded a Fe:Cr:Al ratio of 55:17:28, which is in good agreement with the EDX results. The valence state of Fe was estimated as +3 by comparing the energy positions of the 2p 3/2 peaks to those of the pure oxides[27] (Figure 7-3). In a similar fashion, the energy position of the Cr 2p 3/2 peak is characteristic for the oxidation state +3.[27-28] The broadening of the peak can be explained either by a shake-up peak or by trace elements of Cr in a higher oxidation state[27]. As Cr^{4+} and Cr^{5+} compounds are unstable[29], Cr^{6+} would be most likely, even though the energy shift is not as big as with reference Cr^{6+}-containing compounds. Further, no distinct Cr^{6+}-containing compounds were found by XRD or TEM, making a shake-up peak and therefore Cr in the oxidation state +3 most likely. Despite the poor energy resolution and the small signal-to-noise ratio, the position of the Al 2p peak supports an Al^{3+}-containing oxide.[30] The valence state +3 can therefore be verified for Fe, Cr and Al in the upper region of the film.

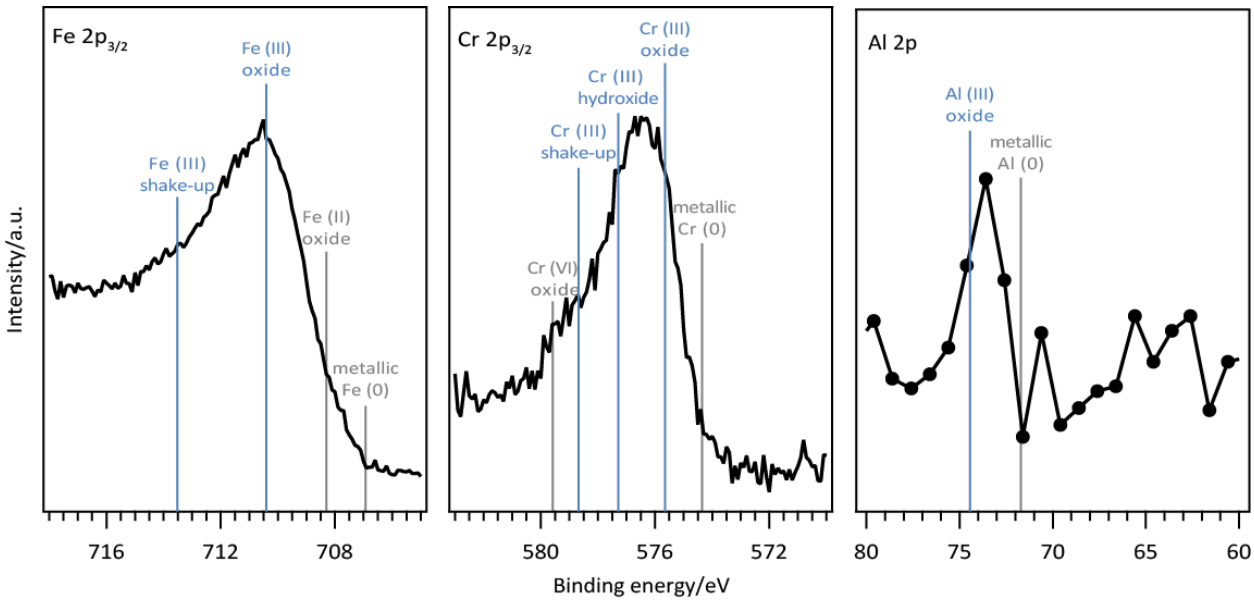

Figure 7-3: X-ray photoelectron spectra of the Fe $2p_{3/2}$, Cr $2p_{3/2}$ and Al 2p edges of the Fe-rich phase in the mesoporous film.

The separation into different phases, all in the corundum structure, is in contrast to previous experimental work, as Steinwehr *et al*. showed that FeCrAl oxides form solid solutions with a miscibility gap only at high Al-contents[31]. The formation of large, compact Cr-rich nanoparticles at the FTO indicates that a heterogeneous nucleation takes place before other phases form. In accordance, the precursor $Cr(NO_3)_3*9H_2O$ is less stable than the other two and dissociates at 100 °C[32], whereas $Fe(NO_3)_3*9H_2O$[33] and $Al(NO_3)_3*9H_2O$[34] are stable up to 250 °C. While these temperatures neglect the influence of the solvent, the trend should stay the same, explaining the phase separation. As an alternative, we attempted aging the precursor solution, which lead to the spontaneous formation of small nanoparticles with a homogenous elemental distribution

(see SI). Films synthesized by depositing these nanoparticles unto FTO, however, lead to films with very low photocurrents (SI Figure 7-2).

The photoelectrochemical characteristics of mesoporous FeCrAl oxide films of different thicknesses were determined in 0.1 M perchloric acid under AM 1.5 substrate illumination. As expected, the optical absorbance increases linearly with the film thickness (SI Figure 7-4). The photocurrent densities follow a similar trend, increasing linearly with the thickness up to 0.25 mA cm^{-2} under AM 1.5 (Figure 7-4a) and an IPCE of 4.9 % at 350 nm (Figure 7-4b) for a 500 nm thick film. Increasing the film thickness further leads to a saturation of the photocurrent, This limiting behavior is not observed for thin films of around 40 nm, where the current density remains constant independent of the illumination direction (SI Figure 7-7). The generated charge carriers can be collected equally well regardless of the sample being illuminated through the substrate or the electrolyte side since most of the light is transmitted resulting in only a small gradient of carrier concentration across the film and a short path to be collected at the electrode/electrolyte interface. Thicker films have carriers created more deeply in the structure and rely on charge carrier transport issues over long distances across the loosely connected, individual particles.

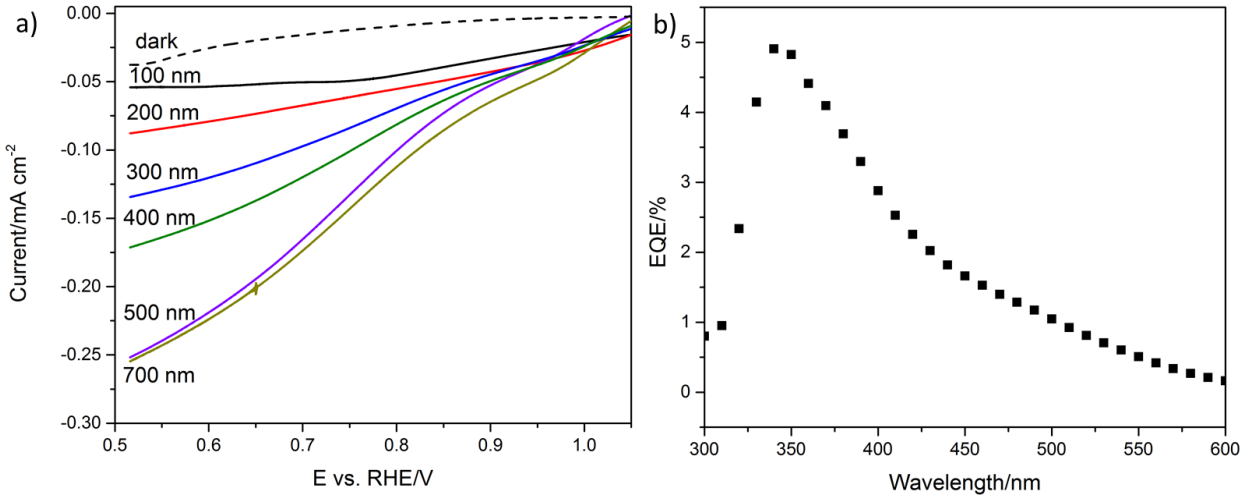

Figure 7-4: a) Cyclic voltammetry curves for mesoporous FeCrAl oxide electrodes in dependence of the film thickness. The samples were illuminated through the substrate with AM 1.5. b) IPCE spectrum determined for a 500 nm thick mesoporous film on FTO. The drop in photocurrent at 350 nm is attributed to light absorption by the FTO substrate.

To enhance the performance, we optimized the electrode morphology by nanostructuring the material. Nanostructuring is a proven strategy for increasing the photogenerated carrier collection efficiency by decoupling the light absorption depth from the charge collection depth[35-37]. Periodic, macroporous morphologies are particularly attractive as they provide both a continuous scaffold for the transport of photogenerated charges to the current collector and a large surface for the heterogeneous charge transfer. Furthermore, the large pore size is beneficial

for the infiltration of electrolyte throughout the whole film thickness, for the diffusion of products away from the semiconductor-electrolyte interface and for lowering the current density and thereby the overpotentials for electrode reactions. A so-called colloidal crystal templating approach was used to obtain macroporous FeCrAl oxide electrodes using periodic arrays of PMMA beads as a template[38]. The PMMA layers were assembled on FTO substrates, (SI Figure 7-5) and impregnated with a freshly prepared sol-gel precursor solution via spin-coating. Calcination leads to the crystallization of the precursors and to the combustion of the PMMA template, resulting in crystalline FeCrAl oxide films with a porous, highly periodic inverse opal structure (Figure 7-5) with the FeCrAl oxide forming a continuous semiconductor scaffold. The electrodes obtained in this way have a homogeneous thickness of approximately 3 µm, good coverage, and a good adhesion to the substrate.

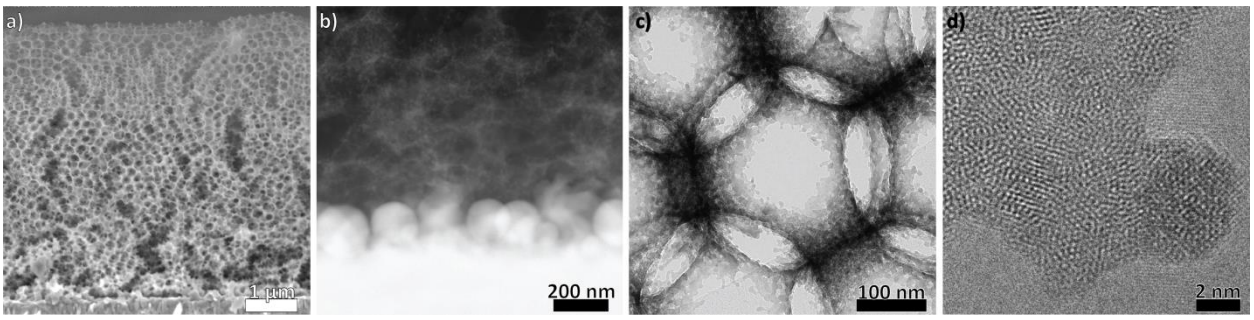

Figure 7-5: a) Cross-sectional SEM image of a macroporous film. b) Cross-sectional TEM image of a macroporous film showing the Cr-rich phase near the substrate. c) BF TEM image of a single pore. d) HRTEM image of a part of the network.

The average pore diameter of (277±10) nm (Figure 7-5c) corresponds to a shrinkage by ca. 9 % during the calcination process to which we attribute the few defects shown in Figure 7-5a. Like in the mesoporous film, a phase segregation into a Cr-rich phase near the interface with an average composition of Fe:Cr:Al = (9±3:90±3:1±1) at-% and a macroporous, Fe-rich phase with an average composition of Fe:Cr:Al = (64±1:25±4:11±5) at-% is observed. The Cr-rich phase forms round nanoparticles with a diameter between 60 and 340 nm. The average composition of the Fe-rich phase was the same over the thickness of the film and no compositional gradients through the film thickness were detected. HRTEM images show the scaffold to be polycrystalline with small grains in the order of 2 to 4 nm. This leads to improved charge transport properties compared to the nanostructured films, where the individual nanoparticles are only partly connected and charge transport is more difficult.

The photoelectrochemical performance of the macroporous FeCrAl films is shown in Figure 7-6 and reveals a dramatic photocurrent increase over the mesoporous films. Compared to a 500 nm thick, mesoporous film, the current density is increased by over 60 % reaching a value of

0.68 mA cm^{-2} at 0.5 V vs. RHE. The IPCE of the macroporous film is also increased significantly throughout the whole wavelength range of 300 to 600 nm, reaching a maximum of 28 % at 400 nm (Figure 7-6b).

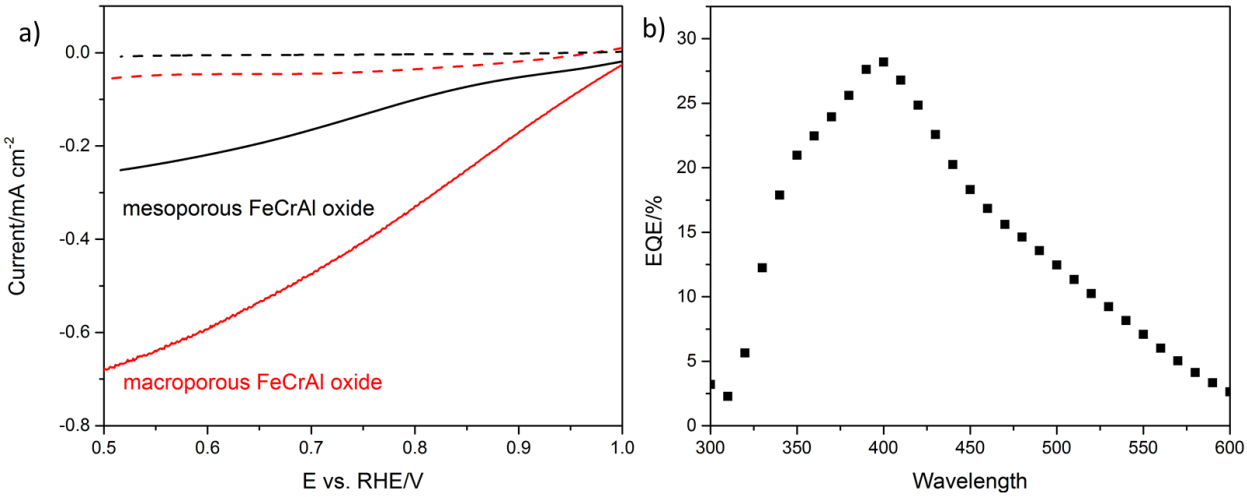

Figure 7-6: a) Linear sweep voltammograms of the macroporous FeCrAl films with AM 1.5 illumination through the substrate. Dashed curves are dark current sweeps. For comparison, the voltammogram of a 500 nm thick, mesoporous film is also shown. b) IPCE spectra determined for the same inverse opal FeCrAl film on FTO.

The IPCE maximum for macroporous films is redshifted to 400 nm, compared to the mesoporous film, which has a maximum at 350 nm. This shift is attributed to the inverse opal structure acting as a photonic crystal[40-41], with transmission measurements (Figure SI 7-9) confirming a stop band centered at 380 nm. An additional shoulder at 350 nm is at the same position as the maximum measured for mesoporous films and can be attributed to the material itself. The drop at 350 nm is attributed to absorption of light by the FTO substrate.

The transfer efficiency of charges to the electrolyte η_{trans} can be assessed from transient current measurements. By illuminating the electrode with chopped light at different chopping frequencies and potentials, photocurrent transients can be measured. From them, the instantaneous current I_{Inst} and the steady-state current I_{ss} can be measured with the ratio of I_{Inst} and I_{ss} being a measure of the electron transfer efficiency η_{trans}.

As can be seen in Figure 7-7a, the shape of the transients is characteristic for the individual morphologies. The mesoporous sample is characterized by a spiky instantaneous current that decays to a constant steady-state current (Figure 7-7a). The transient current of the macroporous sample, on the other hand, shows an instantaneous current closer to the steady-state current, indicating a photocurrent response closer to the ideal square shape that is not limited by recombination. This observation is confirmed by determining the transfer efficiencies of both morphologies at different potentials. A 500 nm thick, mesoporous film shows a transfer efficiency

of 12.5 % at 0.756 V vs. RHE. At this potential, at which the current density is 0.13 mA cm^{-2}, the transfer efficiency reaches a maximum. Under these conditions, the macroporous film has a transfer efficiency of 48.5 %, almost three times as high, indicating superior charge transport properties across the film and explaining the increased transfer efficiency in the macroporous films. The improved electron transfer efficiency has a major contribution to the increased photocurrent shown in Figure 7-6. The increased transfer efficiency indicates that recombination reactions in either the bulk and/or on the surface are decreased. As the macroporous film has a higher surface area the surface recombination velocity should be higher and the increased transfer efficiency can be attributed to decreased bulk recombination due to the short carrier diffusion length. The short carrier diffusion length requires most photogenerated carriers to be produced in a region where there is a space charge field to separate them. In a more two dimensional geometry, with the rather low absorption coefficients especially in the red region of the spectrum, most carriers are generated in the bulk of the grains and recombine before they can diffuse to a space charge region. In the macroporous films, the carriers are very likely to be created in or near a region with a space charge field formed by the electrolyte/semiconductor interface. Therefore there is a higher probability that they will be collected as photocurrent especially in the spectral regions with low absorption coefficients.

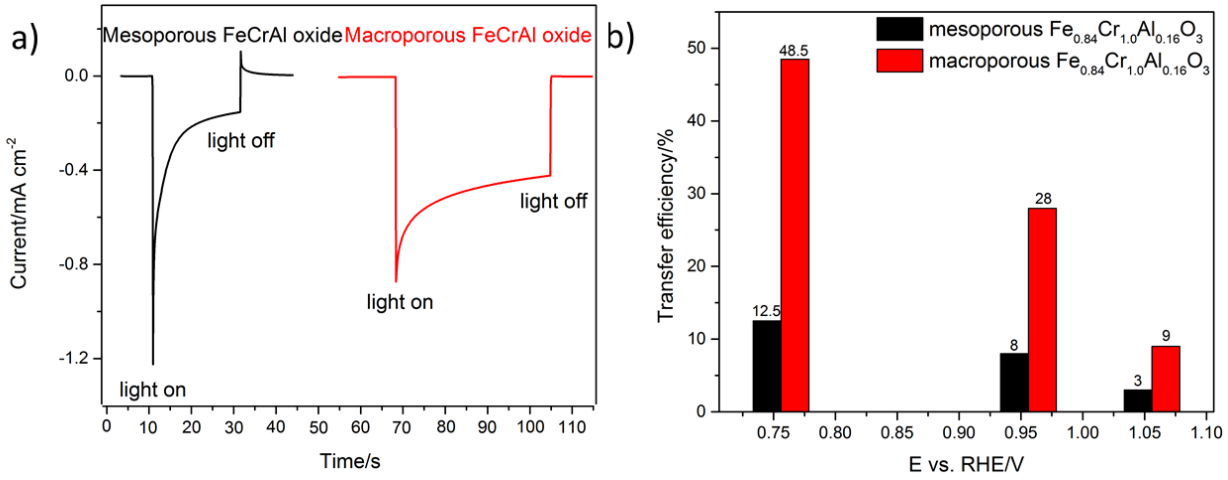

Figure 7-7: a) Photocurrent transients of a mesoporous and a macroporous FeCrAl oxide film. b) Collection efficiency η_{trans} determined for mesoporous and inverse opal macroporous FeCrAl oxide films by transient photocurrent response measurements. The samples were illuminated with a 455 nm diode through the substrate side.

Photoelectrochemical characterization of the electrodes revealed that the macroporous structure was not only beneficial for the device architecture, regarding the solid to electrolyte junction, but also proved beneficial for the charge transport across the metal oxide film. Macroporous structures show a nearly threefold increase of current density compared to the mesoporous FeCrAl oxide film, reaching values of up to 0.68 mA cm^{-2} at 0.5 V vs. RHE under AM 1.5 without any additional catalysts. Compared to devices reported so far in literature, we

demonstrate a 68-fold current density increase[20] as a result of introducing macropores. The main contribution to this electrochemical performance was achieved by the increased electron transfer efficiency to the electrolyte and therefore reduced recombination.

7.4. Conclusion

We presented the synthesis and characterization of semiconducting FeCrAl oxide photocathodes with different porous morphologies and investigated them for solar-driven hydrogen evolution. Mesoporous FeCrAl oxide films were synthesized using a novel sol-gel synthesis to generate large area crack-free films that were characterized and had their thickness optimized to reach a current density of 0.25 mA cm^{-2} under AM 1.5 at 0.5 V vs. RHE with an IPCE of 4.9 %. EDX measurements performed in the TEM showed that a phase separation occurs, with a Cr oxide rich phase adjacent to the substrate and a Fe rich oxide phase on the top. Template synthesis of an inverse opal macroporous $Fe_{0.84}Cr_{1.0}Al_{0.16}O_3$ electrode drastically increased the photocurrent to 0.68 mA cm^{-2} under AM 1.5 at 0.5 V vs. RHE and an IPCE of 28 % at 400 nm without the use of hydrogen evolution catalysts. The collection of minority carriers at the semiconductor/electrolyte interface increased nearly 4 times compared to the optimized mesoporous electrode and are the highest reported so far for this novel material, showing that it is a promising candidate for photoelectrochemical water splitting. Further studies on different morphologies and architectures could additionally improve the device performance. This work shows the potential of nanostructured multinary mixed metal oxides as electrode materials for photoelectrochemical water splitting.

7.5. Acknowledgments

The work was supported by the German Research Foundation (DFG) via the SPP 1613, the Nanosystems Initiative Munich (NIM) and LMUexcellent funded by the DFG, the Bavarian research network ‘Solar Technologies Go Hybrid’, and the Center for Nanoscience (CeNS). We thank the students Nedzada Imamovic, Chih-Chun Huang, Zachary Edelen and Marina Polo Collado for participating in the research. The authors gratefully acknowledge electron microscopy measurements by Steffen Schmidt and Alexander Hufnagel for insightful discussions. Bruce A. Parkinson acknowledges funding from the Division of Chemical Sciences, Geosciences, and Biosciences, Office of Basic Energy Sciences of the U.S. Department of Energy through Grant #DE-FG02-05ER15750. The SHArK project was initially funded by a Dreyfus Grant and has recently been supported by the NSF Funded Center for Chemical Innovation entitled ‘Powering the Planet’ under grant # CHE-1305124. Bruce A. Parkinson also acknowledges support from the Humboldt Foundation.

7.6. Supporting Information

Aging of the FeCrAl oxide precursor solution by stirring under ambient conditions from 0 to 7 days leads to the spontaneous formation of nanoparticles. The resulting nanoparticles are around 1.5-2 nm in size after 3 days (SI Figure 7-1a) and reach 5 nm after 7 days (SI Figure 7-1b). TEM analysis revealed that the formed nanoparticles were already crystalline in solution without additional thermal treatment. Inductively coupled plasma atomic emission spectroscopy (ICP-AAS) analysis on the washed powder (SI Table 7-1) revealed a composition of Fe:Cr:Al = 0.36:0.59:0.05, which is very close to the targeted composition of Fe:Cr:Al = 0.43:0.5:0.08. TEM-EDX analysis of several dozen individual nanoparticles shows a similar composition with a homogeneous distribution of the individual elements in each nanocrystal without any phase separation or surface enrichment. The spontaneous formation of a crystalline phase with the targeted composition provides important evidence that the metal oxide composition harnessed in a high-throughput experiment indeed corresponds to a new thermodynamically stable solid solution and not a mixture of individual oxides.

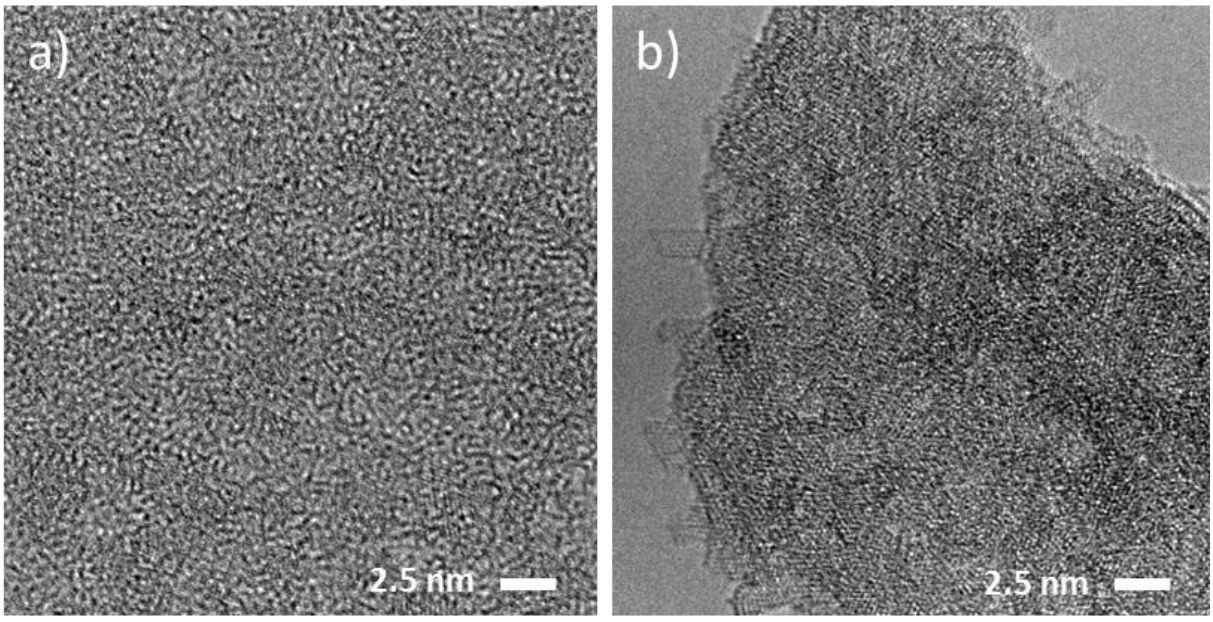

Figure SI 7-1: TEM images of uncalcined FeCrAl nanoparticles formed in the precursor solution after a) 3 days and b) 7 days.

Table SI 7-1: Element composition of FeCrAl oxide nanoparticles formed in the precursor solution. ICP-AAS and TEM-EDX analysis were performed on the particles to compare the element content.

Element	Targeted concentration	ICP-AAS (mol-%)	TEM-EDX (atomic-%)
Fe	0.84	0.72	89
Cr	1.00	1.17	99
Al	0.16	0.11	11

Although aging of the precursor solutions described above leads to a direct formation of targeted crystalline nanoparticles, the films prepared from these solutions show very low photocurrent of 1 nA cm^{-2} at 0.55 V vs. RHE (SI Figure 7-2). The SEM images (SI Figure 7-3) indicate that the films obtained after calcination of aged solutions deposited on FTO substrates are composed of large platelets with an average size of 400 nm and 40 nm thickness. The platelets are randomly oriented on the substrate exposing a large fraction of the FTO substrate. The poor coverage of the conducting substrate and poor electrical contact between the single platelets could account for the low electrode performance.

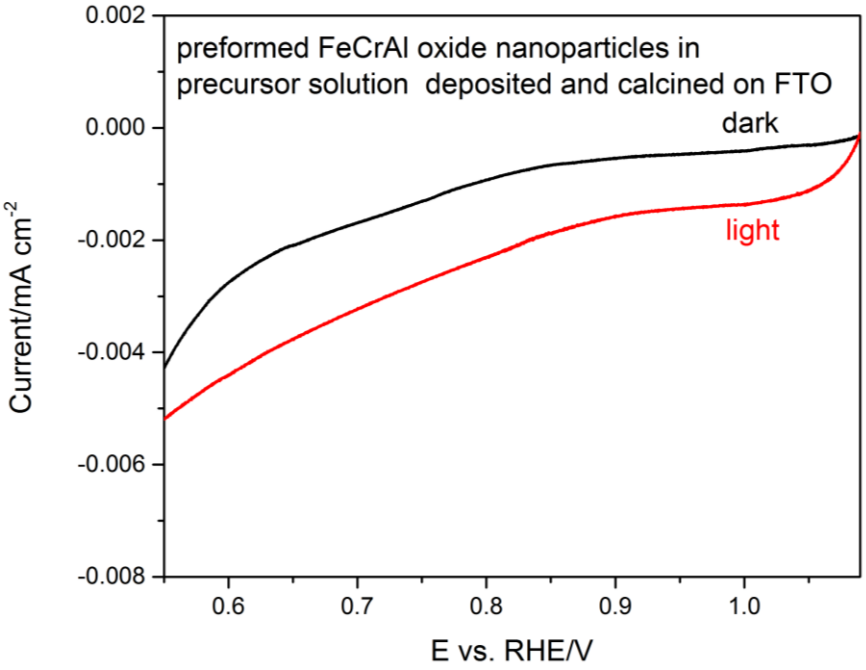

Figure SI 7-2: Cyclic voltammetry curves for a calcined FeCrAl oxide film on FTO synthesized from preformed crystalline nanoparticles in the precursor solution. The photoelectrochemical measurements were performed under substrate illumination and AM 1.5 in 0.1 M perchloric acid as electrolyte.

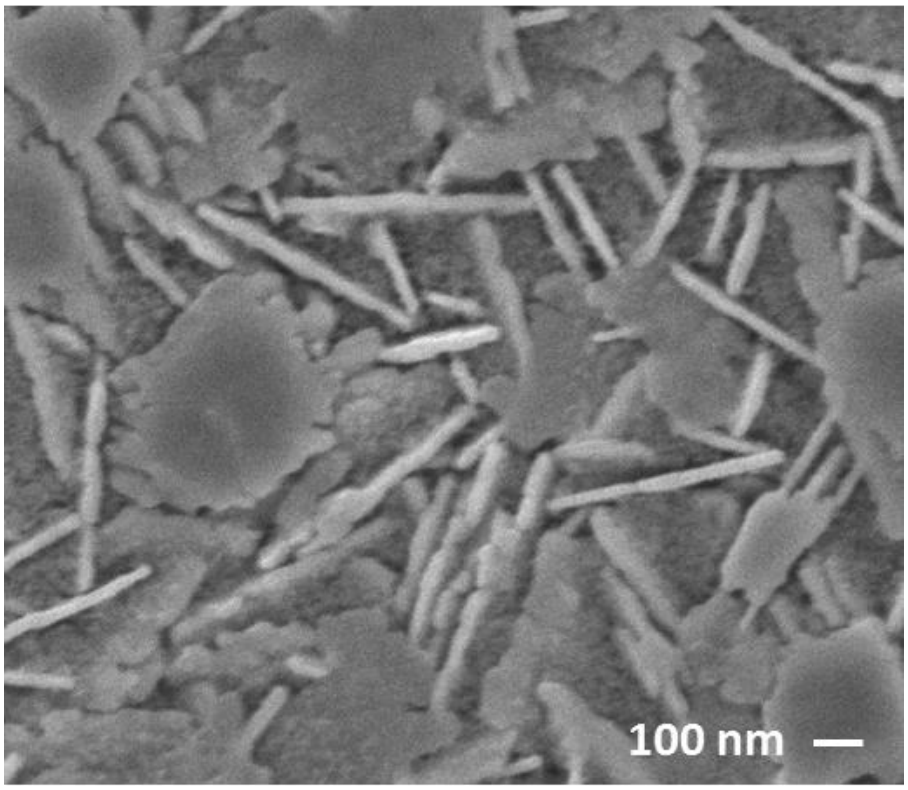

Figure SI 7-3: SEM images of FeCrAl oxide films obtained from a precursor solution aged for 4 days. The precursor solution was deposited on FTO substrate via spin-coating and calcined at 525 °C.

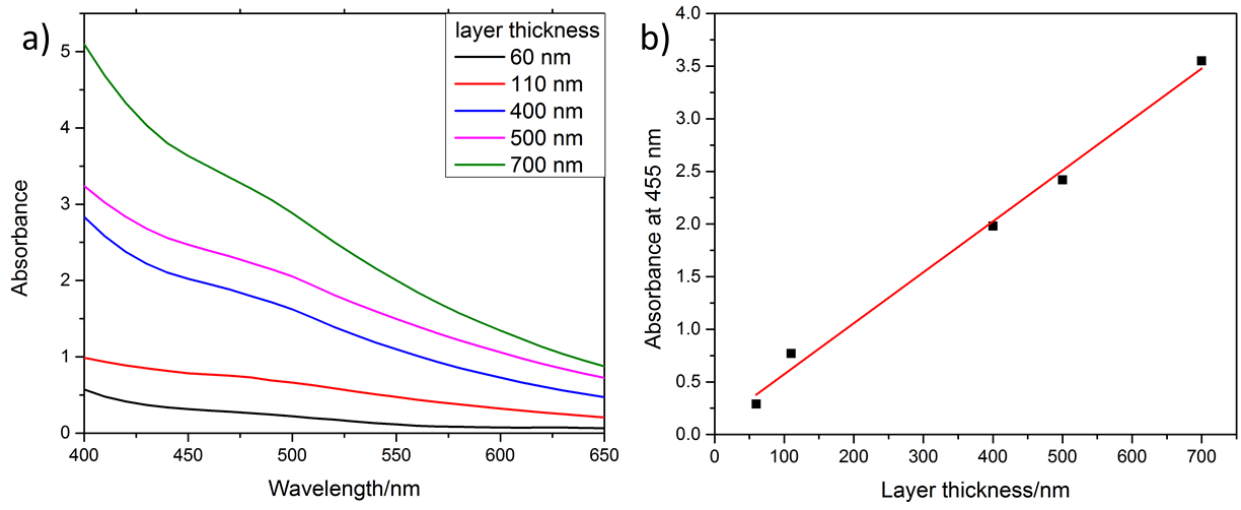

Figure SI 7-4: a) Absorbance spectra of mesoporous FeCrAl oxide layers coated on FTO with increasing film thickness. b) Linear absorbance increase of FeCrAl oxide layers at 455 nm with film thickness.

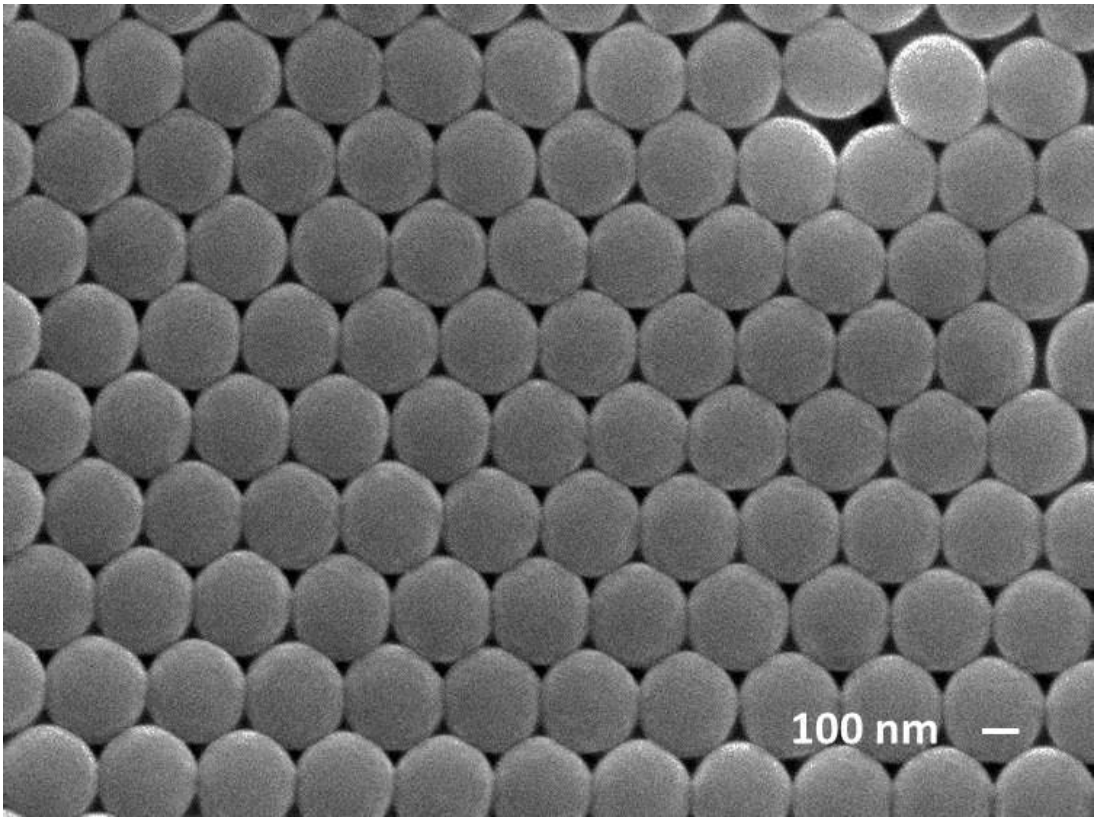

Figure SI 7-5: SEM image of highly ordered PMMA spheres on FTO.

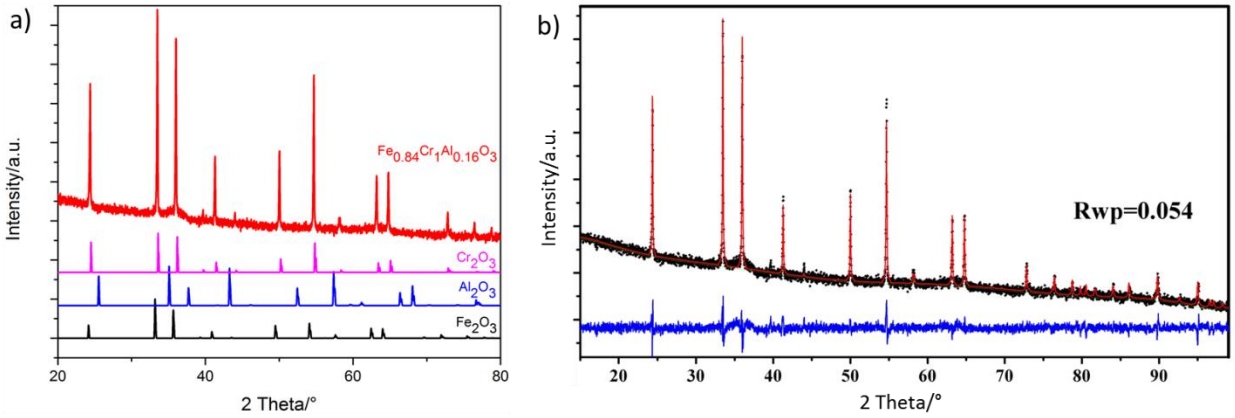

Figure SI 7-6: a) Powder-XRD pattern of mesoporous FeCrAl oxide. The individual metal oxides Cr_2O_3 (ICDD card number 38-1479), Fe_2O_3 (ICDD card number 33-664) and Al_2O_3 (ICDD card number 46-1212) are shown for comparison. b) Results of the whole-powder-pattern profile refinement (Le Bail method). The observed intensity data is plotted in the upper field as ♦, the calculated pattern is shown as a red line in the same field, and the difference between the observed and calculated patterns is shown as a blue line in the lower field.

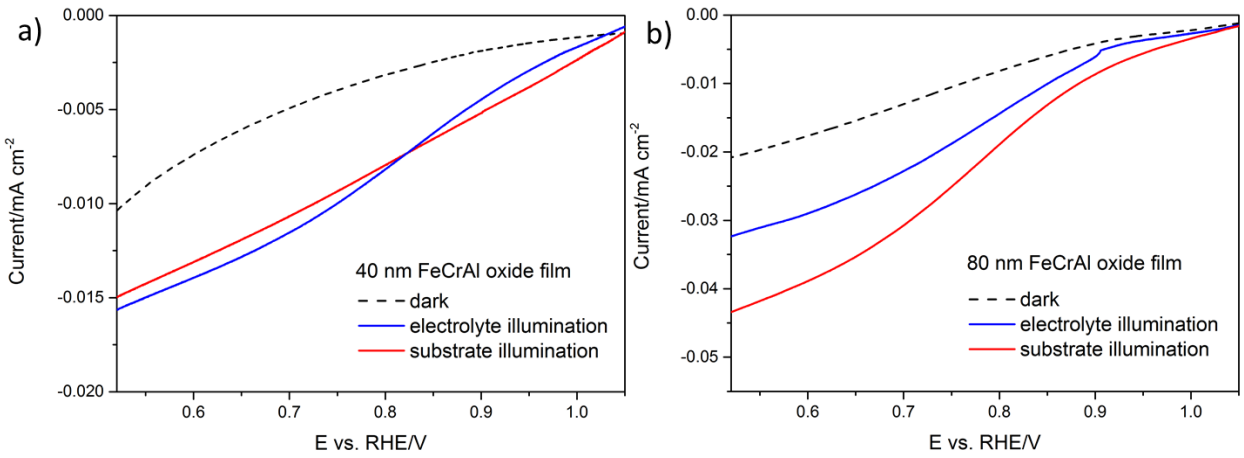

Figure SI 7-7: Cyclic voltammetry curves for a) 40 nm and b) 80 nm mesoporous FeCrAl oxide films on FTO under electrolyte and substrate illumination. The photoelectrochemical measurements were performed under AM 1.5 in 0.1 M perchloric acid.

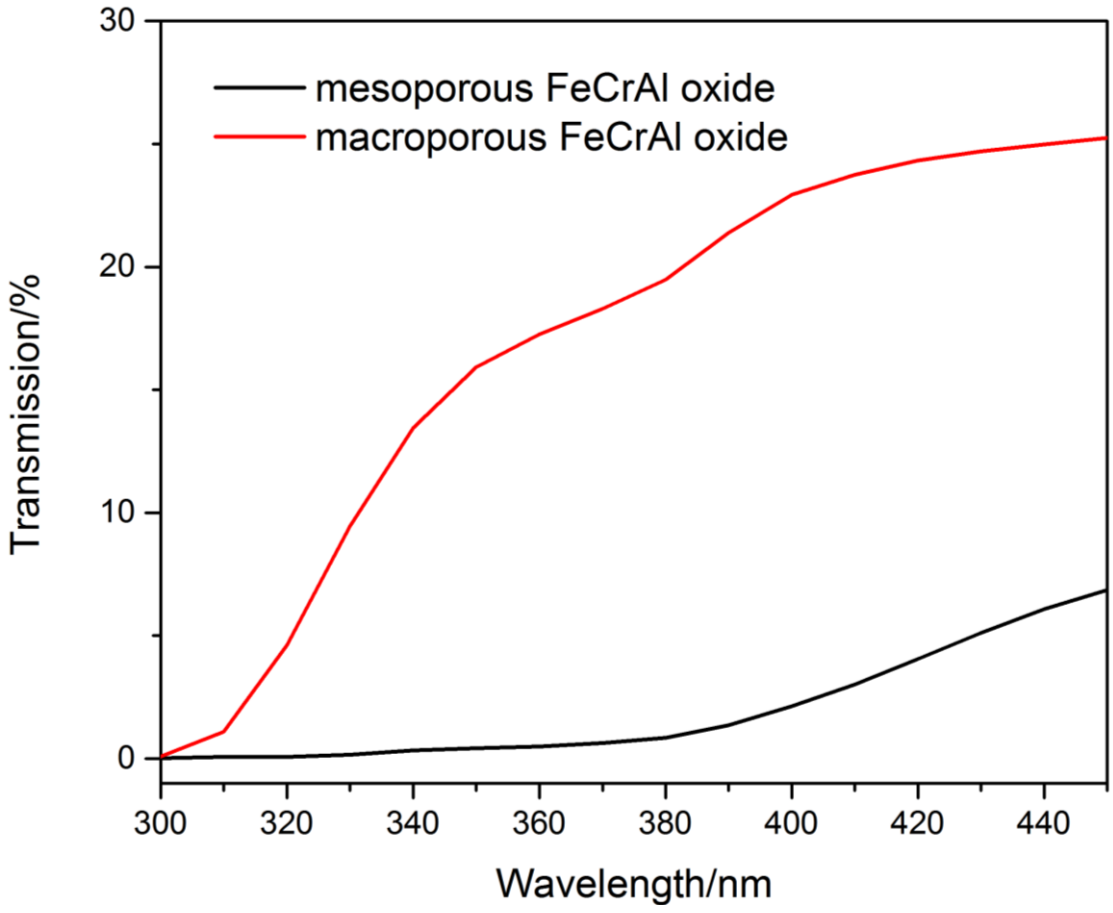

Figure SI 7-8: Transmission measurements on mesoporous and macroporous electrodes.

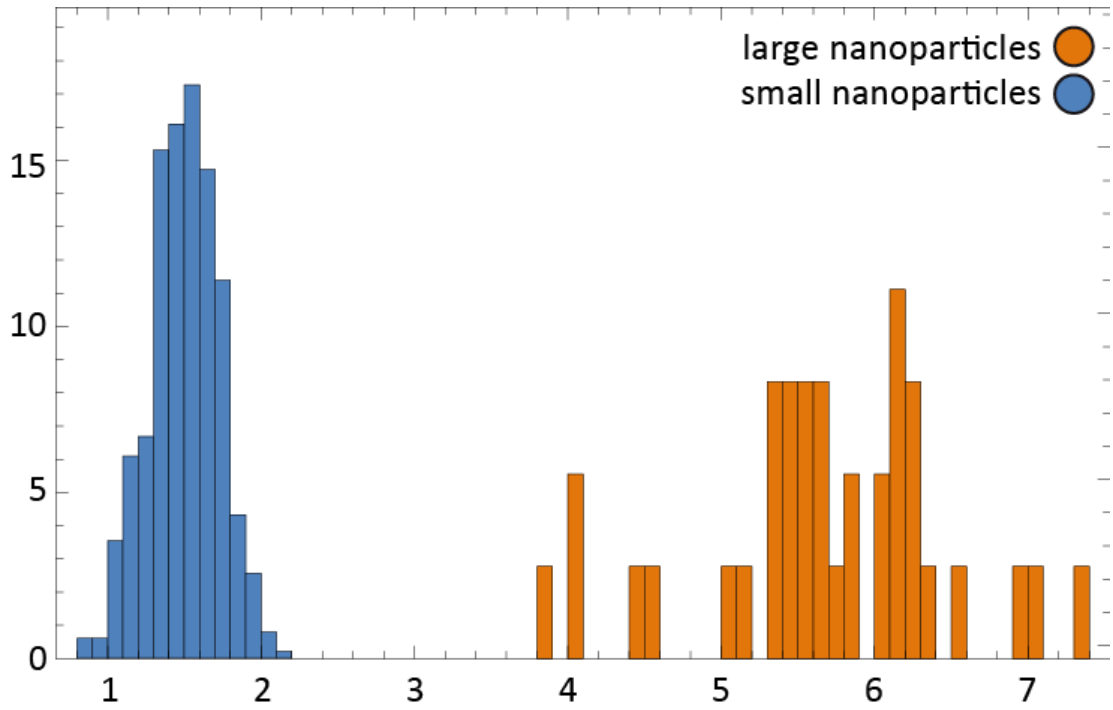

Figure SI 7-9: TEM particle size distribution of and the two different kinds of Fe-rich nanoparticles in a mesoporous FeCrAl oxide film.

7.7. References

(1) Grätzel, M. *Nature* **2001,** *414*, 338-344.

(2) Walter, M. G.; Warren, E. L.; McKone, J. R.; Boettcher, S. W.; Mi, Q.; Santori, E. A.; Lewis, N. S. *Chem. Rev.* **2010,** *110*, 6446-6473.

(3) Abdi, F. F.; Han, L.; Smets, A. H. M.; Zeman, M.; Dam, B.; van de Krol, R. *Nat. Commun.* **2013,** *4,* 2195-2197.

(4) Sivula, K.; Le Formal, F.; Grätzel, M. *ChemSusChem* **2011,** *4*, 432-449.

(5) Tacca, A.; Meda, L.; Marra, G.; Savoini, A.; Caramori, S.; Cristino, V.; Bignozzi, C. A.; Pedro, V. G.; Boix, P. P.; Gimenez, S.; Bisquert, J. *ChemPhysChem* **2012,** *13*, 3025-3034.

(6) Fujishima, A.; Honda, K. *Nature* **1972,** *238*, 37-38.

(7) Dominey, R. N.; Lewis, N. S.; Bruce, J. A.; Bookbinder, D. C.; Wrighton, M. S. *J. Am. Chem. Soc.* **1982,** *104*, 467-482.

(8) Paracchino, A.; Laporte, V.; Sivula, K.; Grätzel, M.; Thimsen, E. *Nat. Mater.* **2011,** *10* (6), 456-461.

(9) Prévot, M. S.; Guijarro, N.; Sivula, K. *ChemSusChem* **2015**, 1359-1367.

(10) Castelli, I. E.; Olsen, T.; Datta, S.; Landis, D. D.; Dahl, S.; Thygesen, K. S.; Jacobsen, K. W., *Energy Environ. Sci.* **2012,** *5*, 5814-5819.

(11) Castelli, I. E.; Landis, D. D.; Thygesen, K. S.; Dahl, S.; Chorkendorff, I.; Jaramillo, T. F.; Jacobsen, K. W. *Energy Environ. Sci.* **2012,** *5*, 9034-9043.
(12) Woodhouse, M.; Parkinson, B. A. *Chem. Soc. Rev.* **2009,** *38*, 197-210.
(13) Woodhouse, M.; Parkinson, B. A. *Chem. Mater.* **2008,** *20*, 2495-2502.
(14) Parkinson, B. *Energy Environ. Sci.* **2010,** *3,* 509-511.
(15) Anunson, P. N.; Winkler, G. R.; Winkler, J. R.; Parkinson, B. A.; Schuttlefield Christus, J. D. *J. Chem. Educ.* **2013,** *90*, 1333-1340.
(16) Borgmann, S.; Schuhmann, W.; Potyrailo, R.; Mirsky, V. *Combinatorial Methods for Chemical and Biological Sensors*, Eds. Springer New York: **2009**, 331-370.
(17) Sliozberg, K.; Schäfer, D.; Meyer, R.; Ludwig, A.; Schuhmann, W. *ChemPlusChem* **2015,** *80*, 136-140.
(18) Schuppert, A. K.; Savan, A.; Ludwig, A.; Mayrhofer, K. J. J. *Electrochim. Acta* **2014,** *144*, 332-340.
(19) Rowley, J. G.; Do, T. D.; Cleary, D. A.; Parkinson, B. A. *ACS Appl. Mater. Interfaces* **2014,** *6*, 9046-9052.
(20) Sliozberg, K.; Stein, H.; Khare, C.; Parkinson, B. A.; Ludwig, A.; Schuhmann, W. *ACS Appl. Mater. Interfaces* **2015**, 7, 4883-4889.
(21) Mandlmeier, B.; Minar, N. K.; Feckl, J. M.; Fattakhova-Rohlfing, D.; Bein, T. *J. Mater. Chem. A* **2014,** *2*, 6504-6511.
(22) Kondofersky, I.; Dunn, H.; Müller, A.; Mandlmeier, B.; Feckl, J. M.; Fattakhova-Rohlfing, D.; Scheu, C.; Peter, L. M.; Bein, T. *ACS Appl. Mater. Interfaces* **2015**, 7, 4623-4630.
(23) Strecker, A.; Salzberger, U.; Mayer, J. *Prakt. Metallogr.* **1993,** *30*, 482-495.
(24) Klahr, B. M.; Martinson, A. B. F.; Hamann, T. W. *Langmuir* **2011,** *27* (1), 461-468.
(25) Le Bail, A.; Duroy, H.; Fourquet, J. L. *Mater. Res. Bull.* **1988,** *23*, 447-452.
(26) Moulder, J.; Stickle, W.; Sobol, P.; Bomben, K., Handbook of X-ray Photoelectron Spectroscopy; Perkin-Elmer Corporation: Eden Prairie, MN, **1992**.
(27) Biesinger, M. C.; Payne, B. P.; Grosvenor, A. P.; Lau, L. W. M.; Gerson, A. R.; Smart, R. S. C., *Appl. Surf. Sci.* **2011,** *257*, 2717-2730.
(28) Galtayries, A.; Warocquier-Clérout, R.; Nagel, M. D.; Marcus, P., *Surf. Interface Anal.* **2006,** *38*, 186-190.
(29) Wiberg, E.; Wiberg, N., *Inorganic Chemistry*. Academic Press: 2001.
(30) Strohmeier, B. R. *Surf. Interface Anal.* **1990,** *15*, 51-56.
(31) Steinwehr, H.E.v. *Z. Kristallogr. Miner.* **1967**, 125, 377-403.
(32) Małecki, A.; Małecka, B.; Gajerski, R.; Łabuś, S., , S. *J. Therm. Anal. Calorim.* **2003**, 72, 135-144.
(33) Wieczorek-Ciurowa, K.; Kozak, A. J. *J. Therm. Anal. Calorim.* **1999,** *58* (3), 647-651.
(34) El-Shereafy, E.; Abousekkina, M. M.; Mashaly, A.; El-Ashry, M. *Radioanal. Nucl. Chem.* **1998,** *237*, 183-186.

(35) Fu, Y.; Chen, J.; Zhang, H. *Chem. Phys. Lett.* **2001,** *350*, 491-494.
(36) Tilley, S. D.; Cornuz, M.; Sivula, K.; Grätzel, M. *Angew. Chem. Int. Ed.* **2010,** *49*, 6405-6408.
(37) Cesar, I.; Sivula, K.; Kay, A.; Zboril, R.; Grätzel, M. *J. Phys. Chem. C* **2008,** *113*, 772-782.
(38) Fattakhova-Rohlfing, D.; Zaleska, A.; Bein, T., *Chem. Rev.* **2014,** *114*, 9487-9558.
(39) Woodcock, L. V. *Nature* **1997,** *385*, 141-143.
(40) Schroden, R. C.; Al-Daous, M.; Blanford, C. F.; Stein, A., *Chem. Mater.* **2002,** *14*, 3305-3315.
(41) Waterhouse, G. I. N.; Waterland, M. R. *Polyhedron* **2007,** *26*, 356-368.

8. Conclusion and Outlook

The aim of this thesis was the structural characterization of photoelectrodes for water splitting. Such photoelectrodes are made out of semiconductors with desirable properties, such as a small band gap, valence and conduction band straddling the redox potentials of water, good light absorption and efficient charge transport. As no material investigated so far fulfills all requirements, several strategies to improve the performance have been developed. A very promising one is to structure the material on the nanoscale and thereby increase the surface area, at which the reaction happens. The structure therefore is a very important factor which can be analyzed in detail by SEM and TEM. Together with measurements of the properties, three different materials systems were investigated in this way: noble metal nanoparticles on TiO_2, Fe_2O_3/WO_3 dual absorbers and the novel material FeCrAl oxide.

TiO_2 in its anatase modification is a popular photoanode and photocatalyst material. However, it has a large band gap of 3.2 eV, which limits light absorption to the UV region of the solar spectrum. By depositing an additional photosensitizer, in this study noble metal nanoparticles, the performance can be vastly increased. Noble metal nanoparticles absorb light by localized surface plasmon resonance, and the position and width of the absorption band is influenced by the particle size distribution, particle size and the dielectric constant of the environment. They can therefore be tailored to absorb visible light. In addition, they also act as co-catalysts. Size, crystal structure and distribution of the nanoparticles have a big effect on the efficiencies of both processes and were therefore investigated in detail to understand the properties. In Chapter 4, experiments in which an anatase layer was plasma-deposited onto a FTO substrate are described. This pure anatase layer also served as a reference sample. Au nanoparticles were then deposited onto the anatase layers by two different methods, photo- and plasma deposition. The second method was also used to deposit Au/Ag nanoparticles. The structures of all four samples were characterized mostly using TEM cross-sections, the optical properties by UV-Vis spectroscopy and the photocatalytic performance by measuring the amount of evolved hydrogen under UV light and using the sacrificial donor MeOH. Photodeposited nanoparticles grow both on top and inside the porous anatase layer, and the measured particle size distribution could be described by two log-normal distributions, one for particles inside and one for particles on top of the anatase. In contrast, plasma-deposited nanoparticles were only found on top of the anatase. Except for a few larger nanoparticles, which were ascribed to a coarsening process, the size distribution could be described by a single log-normal function. In addition to defect-free nanoparticles, all samples had nanoparticles with several defects like stacking faults, grain boundaries or five-fold twinning. The Au/Ag nanoparticles formed a core-shell structure, with Au as the core and Ag as the shell materials. The surface energies of the two metals were identified as the driving force for this particular

arrangement being favorable. Only plasma-deposited Au-TiO_2 showed a significant LSPR effect, with photodeposited Au-TiO_2 having a minor LSPR band and plasma-deposited Au/Ag-TiO_2 having none. The position, width, and intensity of the bands could in all cases be explained by the distribution and sizes distribution of the nanoparticles. The water splitting performance of photodeposited Au-TiO_2 was the highest, which could be correlated to the close contact with the TiO_2 substrate. In spite of photodeposited and plasma-desposited Au-TiO_2 having similar noble metal contents and that of Au/Ag-TiO_2 being only half as high, Ag/Au-TiO_2 outperformed Au-TiO_2. Previous investigations explained this by an electron transfer from the Ag shell to the Au core and the subsequent creation of highly active surface sites. Combining the results of all characterization methods resulted in an enhanced understanding of the complex interplay between synthesis, structure and properties.

Due to its narrow band gap, hematite is a promising contender for photoelectrochemical water splitting. However, it has several disadvantages and one performance-enhancing approach, doping, was investigated in detail in Chapter 5. Mesoporous hematite films were deposited by a sol-gel approach, which could be modified for the production of Sn-doped films by adding a Sn-precursor. Investigation by IMPS showed the rate constant for hole transfer to be increased by more than an order of magnitude compared to undoped films, leading to a significant performance increase. The dopant was incorporated into the hematite structure without phase separation or the formation of tin oxide clusters and could mostly be found at the surface of the hematite nanoparticles. This hints at a structure-function relationship between the surface enrichment by Sn and the increased hole transfer. Two additional performance-enhancing approaches are also described in brief in Chapter 5. The recombination of electrons and holes at the surface could be suppressed by deposition of pre-formed Co_3O_4 nanoparticles, whereas electron conductivity could be increased by introducing a conducting ATO scaffold.

The gained insights then fueled work on a dual absorber approach and in Chapter 6, two series of Fe_2O_3/WO_3 dual absorbers were designed in a way that the effect of the morphology of WO_3 on the performance could be investigated. The first series consisted of a compact WO_3 layer, a mesoporous, tin-doped Fe_2O_3 layer and a mesoporous, tin-doped Fe_2O_3 layer that was infiltrated with WO_3. This series allowed analyzing the effect of depositing WO_3 as a surface treatment. WO_3 can fulfill several roles, among them that of a charge collector of electrons generated in Fe_2O_3, and was in the second series introduced as a macroporous current collector. In all samples, WO_3 formed large crystalline domains and good charge transport properties can be expected. An abrupt interface between Fe_2O_3 and WO_3 without orientation relationships or amorphous phases was found for all samples. UV-Vis measurements showed WO_3 to strongly scatter at wavelengths above $\sim$ 350 nm, and this contribution to be reduced by Fe_2O_3. WO_3 can therefore act as a reflective layer. WO_3 further increased the transfer efficiencies compared to pure Fe_2O_3 and led to the reduction of the onset potential from 1.0 to 0.8 V, presumably due to the reduction of loss pathways. The combination of all these

beneficial effects led to the dual absorbers producing photocurrents several times higher than those of the individual materials.

In Chapter 7, the sol-gel synthesis and investigation of a novel material, FeCrAl oxide, which was previously identified by a combinatorial approach and published, is described. The synthesis yielded mesoporous layers, with a phase separation into large, Cr-rich nanoparticles at the substrate and a network of small, Fe-rich nanoparticles and ultrasmall, Al-rich nanoparticles on top. Introducing an opaline PMMA template led to a macroporous inverse opal structure, for which a phase separation into a Cr-rich phase near the substrate and a Fe-rich phase on top was observed. The phase separation of both samples could be explained by the stability of the precursors, with $Cr(NO_3)_3$ decomposing at lower temperatures than the other two. The macroporous structure had a fourfold increase of the minority collection efficiency, which could be correlated to the formation of a continuous scaffold compared to individual nanoparticles in the mesoporous sample. Further, the low surface roughness of the macroporous structure led to enhanced light absorption by making it act as a photonic crystal. Accordingly, the macroporous structure showed higher photocurrents than the mesoporous structure and signifies a promising first step into the optimization of the material.

In all three studies, correlating synthesis conditions, structural investigations and properties allowed for a better understanding of the materials systems and validated the research approach. All studies presented in this thesis are exemplary of promising future research directions: in Chapter 4, a material was modified to improve the performance, in Chapter 5 two photoabsorbers were combined and in Chapter 6 a completely new material was investigated. A combination of all approaches, by identifying promising materials, combining and then modifying them, is certain to negate several of the problems plaguing currently investigated materials systems and yield photoelectrodes with high performances. In addition, there are also several ways in which the electron microscopic investigation can be enhanced. For example, the analysis of the electronic structures of novel materials by EELS or the three-dimensional acquisition of nanostructures by tomography should allow for significantly deeper insights and exciting opportunities.

9. Curriculum Vitae

Current Position

Ludwig Maximilian University & Max Planck Institut für Eisenforschung
Ph.D. candidate under the supervision of Christina Scheu
Thesis: Transmission Electron Micoscopic Investigation of Several Nanostructured Photoelectrodes for Photoelectrochemical Water Splitting
Expected graduation: November 2015

Education

Ludwig Maximilian University March 2012
M.Sc. in Chemistry, final grade: very good (1.41)
Major: inorganic and physical chemistry; Minor: materials science
Thesis: Transmission Electron Microscopy Investigations on $TbMnO_3$ and $BiFeO_3$ Thin Films

Ludwig Maximilian University February 2010
B.Sc. in Chemistry and Biochemistry, final grade: good (2.20)
Thesis: Synthesis and Properties of KCo_2As_2, the series $KCo_{2-x}Fe_xAs_2$ and P-/Ca-substituted $SrRh_2As_2$

Gymnasium Starnberg June 2006
Abitur, final grade: 1.7

Teaching Experience

Ludwig Maximilian University of Munich

Instructor: Physical Chemistry 1 Lab Course	Summer 2013
Instructor: Inorganic Chemistry Lab Course	Summer 2013
Instructor: Inorganic Chemistry Lab Course	Winter 2012
Teaching Assistant: Inorganic Chemistry Lab Course	Winter 2010
Teaching Assistant: Inorganic Chemistry 2 Lab Course	Summer 2010

Skills

Bilingual in German and English, conversant in French

Jeol JEM-2010, FEI Titan, probe-corrected FEI Themis

Wolfram Mathematica, Gatan Digital Micrograph, FEI TIA, Blender, JEMS, Adobe Illustrator, Adobe Photoshop, Microsoft Office

10. Publications and Presentations

10.1. Publications

J. M. Feckl, H. K. Dunn, P. M. Zehetmaier, A. Müller, S. R. Pendlebury, P. Zeller, K. Fominykh, I. Kondofersky, M. Döblinger, J. R. Durrant, C. Scheu, L. M. Peter, D. Fattakhova-Rohlfing, T. Bein: Ultrasmall Co_3O_4 Nanoparticles Strongly Enhance Solar Water Splitting on Mesoporous Hematite, Advanced Materials Interfaces, DOI: 10.1002/admi.201500358 (2015).

K. Fominykh, P. Chernev, I. Zaharieva, J. Sicklinger, G. Stefanic, M. Döblinger, A. Müller, A. Pokharel, S. Böcklein, C. Scheu, T. Bein, D. Fattakhova-Rohlfing: Iron-Doped Nickel Oxide Nanocrystals as Highly Efficient Electrocatalysts for Alkaline Water Splitting, ACS Nano 9 (5), 5180-5188 (2015).

I. Kondofersky, H. K. Dunn, A. Müller, B. Mandlmeier, J. M. Feckl, D. Fattakhova-Rohlfing, C. Scheu, L. M. Peter, T. Bein: Electron Collection in Host-Guest Nanostructured Hematite Photoanodes for Water Splitting: The Influence of Scaffold Doping Density, ACS Applied Materials & Interfaces, 7 (8), 4623-4630 (2015).

T. Dennenwaldt, M. Lübbe, M. Winklhofer, A. Müller, M. Döblinger, H. Sadat Nabi, M. Gandman, T. Cohen Hyams, W. D. Kaplan, W. Moritz, R. Pentcheva, C. Scheu: Insights into the structural, electronic, and magnetic properties of $Fe_{2-x}Ti_xO_3/Fe_2O_3$ thin films with x=0.44 grown on Al_2O_3 (0001), Journal of Materials Science 50 (1), 122-137 (2015).

S. Farokhipoor, C. Magen, S. Venkatesan, J. Íñiguez, C. J. M Daumont, D. Rubi, E. Snoeck, M. Mostovoy, C. de Graaf, A. Müller, M. Döblinger, C. Scheu, B. Noheda: Artificial Chemical and Magnetic Structure at the Domain Walls of an Epitaxial Oxide, Nature 515 (7527), 379-383 (2014).

H. K. Dunn, J. M. Feckl, A. Müller, D. Fattakhova-Rohlfing, S. G. Morehead, J. Roos, L. M. Peter, C. Scheu, T. Bein: Tin-doping speeds up hole transfer during light driven water oxidation at hematite photoanodes, Physical Chemistry Chemical Physics 16 (44), 24610-24620 (2014).

Y. Liu, K. Peters, B. Mandlmeier, A. Müller, K. Forminykh, J. Rathousky, C. Scheu, D. Fattakhova-Rohlfing: Macroporous Indium Tin Oxide Electrode Layers as Conducting Substrates for Immobilization of Bulky Electroactive Guests, Electrochimica Acta 140, 108-115 (2014).

I. Kondofersky, A. Müller, H. K. Dunn, B. A. Parkinson, D. Fattakhova-Rohlfing, C. Scheu, T. Bein: Nanostructured FeCrAl Oxide Photocathodes for Water Photoelectrolysis, submitted.

A. Müller, I. Kondofersky, A. Folger, D. Fattakhova-Rohlfing, T. Bein, C. Scheu: Dual Absorber Fe_2O_3/WO_3 Host-Guest Architectures for Improved Charge Generation and Transfer in Photoelectrochemical Water Splitting, in preparation.

H. K. Dunn, S. R. Pendlebury, J. M. Feckl, A. Müller, J. Roos, S. D. Kloß, D. Fattakhova-Rohlfing, C. Scheu, J. R. Durrant, T. Bein. Majority Carrier Diffusion in Photoelectrodes for Water Splitting: The Example of Hematite, in preparation.

A. Müller, S. Peglow, M. Karnahl, A. Kruth, H. Junge, V. Brüser, C. Scheu: Au and Au/Ag Nanoparticles on Titania Layers: Correlation of Deposition Method, Morphology and Photo(electro)catalytic Properties, in preparation.

A. Hufnagel, K. Peters, A. Müller, C. Scheu, D. Fattakhova-Rohlfing, T. Bein: Current Enhancement by Distributed Electron Collectors for Zink Ferrite Water Oxidation Photoanodes Prepared by Atomic Layer Deposition, in preparation.

A. Müller, A. Folger, M. Kucera, C. Carter, C. Scheu: Reducing the Complexity of Focused Ion Beam Tomography Data Sets with Motion Detection Algorithms, in preparation.

10.2. Poster Presentations

The Effect of Different Au Nanoparticles on the Water-Splitting Performance of Au-TiO_2/FTO Layers, IAM Nano, Hamburg, Germany (Jul. 2015).

Three-Dimensional Analysis of Photoelectrodes by FIB Sectioning, nanoGe Solar Fuel 15, Palma de Mallorca, Spain (Mar. 2015).

TEM Studies of Noble Metal Nanoparticles on TiO_2, SPP 1613 Annual Meeting, Darmstadt, Germany (Sept. 2014).

A Year's Worth of Transmission Electron Microscopy Studies on Various Hematite Systems for Water Splitting, SPP 1613 Annual Meeting, Ellwangen, Germany (Oct. 2013).

TEM Investigations on Thin Ti-Fe-O Films on Al_2O_3, SPP 1613 Kick-Off Meeting, Erlangen, Germany (Nov. 2012).

Transmission Electron Microscopy Studies on Domain Walls in $TbMnO_3$ Thin Films, MACAN Thermodynamics Workshop, Istanbul, Turkey (Nov. 2012).

Transmission Electron Microscopy Studies on Domain Walls in $TbMnO_3$ Thin Films, CeNS Workshop, Venice, Italy (Sept. 2012).

10.3. Oral Presentations

Metal Oxide Nanostructures for Electrochemical and Photoelectrochemical Water Splitting, SPP 1613 Kick-Off Meeting, Bergisch Gladbach, Germany (Oct. 2015).

Transmission Electron Microscopy and its Application to Nanostructured Photoelectrodes for Water Splitting, Seminar Talk, INP Greifswald, Greifswald, Germany (Jul. 2015).

An Introduction to TEM and the Case Study of Gold Nanoparticles on Titania, Ebernburg, Germany (Mar. 2015).

Coupling Analysis and Theory to Improve Photocatalysis, MISTI Meeting, Cambridge, MA, USA (Nov. 2014).

An Introduction to Transmission Electron Microscopy, MIT Materials Lectures: The Basics Series, MIT, Cambridge, MA, USA (Nov. 2014).

Novel Materials and Morphologies for Photoelectrochemical Water Splitting, SPP 1613 Annual Meeting, Darmstadt, Germany (Sept. 2014).

Improving the Efficiency of Photoanodic Water Oxidation, PICS, Marseille, France (May 2014).

Transmission Electron Microscopy, SPP 1613 Meeting, Hannover, Germany (Feb. 2014).

Improving the Efficiency of Hematite Photoanodes, Mechanics Meets Energy, Winterberg, Germany (Jan. 2014).

Nuclear Power in Germany: The Influence of Fukushima on Germany's Energy Landscape, Southern Methodist University, Dallas, TX, USA (Nov. 2013).

Nanostructured Oxide Electrodes for (Photo)electrochemical Water Oxidation, SPP 1613 Annual Meeting, Ellwangen, Germany (Oct. 2013).

Transmission Electron Microscopy Insights into Photo-electrochemical Water Splitting Active Hematite Nanostructures, NIM Summer Retreat, Lenggries, Germany (Jul. 2013).

Transmission Electron Microscopy Insights into Photo-electrochemical Water Splitting-Active Hematite Nanostructures, Mechanics Meets Energy, Düsseldorf, Germany (May 2015).

Transmission Electron Microscopy Insights into Photo-electrochemical Water Splitting Active Hematite Nanostructures, MACAN Capstone Meeting, Haifa, Israel (Apr. 2013).

11. Acknowledgments

Weary traveler, let me warn you: I've worked with many, many people and this is going to be long. So sit down, have a cookie, and let me thank you all.

First off, I would like to thank Tina. I remember traveling to the CeNS workshop in Venice, right after I had started my Ph.D. We had coffee in one of the piazzas and discussed several ideas I had and thought were worth looking into. Tina, you patiently went through them with me and told me that I could potentially follow them all. Ultimately, all of these ideas were discarded because, you know, real life kicked in and I suddenly worked on more projects than I had time for, but this day left me with a very strong impression that I could develop and follow even wacky ideas, and would have your support (I assume that at some point you would have stopped me, but I never quite got that far). This impression stayed with me throughout my whole Ph.D. Having one's advisor's support is wonderful, and afforded me uncommon luxuries such as a Mathematica workshop in London or extended stays in Boston. And as we are on the topic of traveling: A quick back-of-the envelope calculation tells me that I've traveled at least once around the globe. I visited many places I'd never been to, and interacted with scientists of all backgrounds. I believe that this is quite rare, and I am grateful for the many opportunities and the more than generous support.

I'm a microscopist, and whenever people ask me how I spend my day, I tell them that I look at things other people created. It is therefore only fitting that the next people I thank are those in charge of supplying most of the samples, Dina Fattakhova-Rohlfing and Thomas Bein. I could not have asked for a better collaboration, and have learned a lot from both you and the people you work with. Dina, what Tina supplied in knowledge pertaining to TEM, you supplied in electrochemical expertise. I would have been utterly lost without you and am grateful for all the hard work you put into interpreting results, sometimes, and that was a trend of my Ph.D., at ungodly hours. I will also miss going to conferences with you and remember many enjoyable evenings spent talking to you. Thomas, while your busy schedule has not lead me to work as closely with you as I would have liked, your dedication has left a strong impression and I have nothing but the utmost respect for your commitment to fixing even minor details in slides until 1 in the morning.

The time I spent with my group has been very precious in many ways. When I started in the group, I was blessed to enter not just a group of colleagues, but a group of friends. One of the people at the very center of this group was Angi, who must have brought more people into the group than anyone else. That so many decided to stay after working with Angi for just two months is testament to the kind of person she is and I will miss your sage advice almost as much as your Obazda. However, I never worked for Angi but was introduced into the group by Ramona. Ramona, you are one of the kindest people I've ever met and I am glad that you

decided to stick around as a postdoc. I am always happy to come into the office and see you, and then talk about books or the joys and challenges of raising children (I will NEVER procreate and the world has you to thank for it. But, as we discussed, you're ahead of the statistic anyway). I then continued my stay in the group under the tutelage of Sriram, who not only taught me about TEM and multiferroics, but also about how to get published, how to plan a project and many other valuable lessons. And, of course, sometimes you scream down a whole audience giving a talk. Or go hiking in your underpants. So many fun memories… Andi, you handsome devil: I will miss all our talks, spontaneous game sessions while discussing science, and the conferences we've been to. Part of why moving away from Munich was so sad was that I could not sit next to you anymore and I'm happy that I managed to come back to the office and slump down in the chair next to you as often as I did. Christoph, I've known you since we did the theoretical chemistry lab together, and, as I often told you, I would not have survived that one without your helping hand. Joining the group and finding you in it was a welcome surprise. I admire the life balance you've obtained, and the serenity it led to. One day, I too hope to feel like I have time for video games. And until then, I will miss at least talking about them with you. Teresa, we've been to many conferences together and had great fun at them. I will never forget drinking way to much coffee when with you, and must once more apologize. I'm sure you'll be the first to agree that I'm not used to caffeine at all and should stay as far away from it as possible. Chris, while you being split between groups has led to me not knowing you as much as I would have liked to, I fondly remember us trying to drown far too much fish in wine, all while really, really wanting a burger.

At some point, however, all the ancients left and a slew of new people joined. Alena – you are the person in the group I've worked with the closest and I'm very happy that you were willing to follow my crazy ideas and start on a whole new topic, FIB tomography. I could not have asked for a better collaborator, or a more valued friend. Your level-headedness is something I will sorely miss in both areas. From Alena it is, of course, not far to her better half, Stephan. I will miss going running with you, and I will miss the talks we had during those runs. I must also mention the experience of watching you build Ph.D. hats. It is inspiring, and your attention to detail adds a special touch not just to Ph.D. hats, but to everything else you do. It's a logical step from Stephan to Stefan, who manages to have an impressive knowledge of Star Trek all while looking like a perfectly sane person. I always enjoyed coming into your office and striking up a conversation with you. This is a gift you have, and it is far too easy to lose track of time while talking to you. Anna, I think I say everything there is to say when I call you an old woman one last time. I will miss our little kerfuffles a lot. The last person I would like to thank in the group is Katha, and talking about her actually means coming back to Sriram, whom she – and god knows how! – convinced to have some beer at Oktoberfest. Katha, I would like to thank you for always greeting me with a smile when I came into the office and for your encyclopedic and absolutely essential knowledge of all things relating to "Bachelorette", "Bauer sucht Frau" and other series in that vein. I honestly don't know who will make me feel this puzzled anymore and fear that only metal will make me shake my head from now on.

When we moved to Düsseldorf, the group was received with open arms by the group of Gerhard Dehm and I was lucky to find good friends in it. Basti, I knew you were a kindred spirit when you told me that you sleeved even playing cards from board games and I will miss spontaneous Netrunner sessions as much as your devotion to shenanigans. Vera, you are the person keeping him in check and someone to, every now and then, have a serious conversation with. I will miss your frank and honest words which you somehow manage to deliver all while being a fun person. Steffen… Steffen, there's no way I can sum you up without dedicating a whole thesis to theories of you. You are sometimes a conundrum, but always someone I deeply respect. I hope that I will find someone else to annoy with Blender and random coding questions. And one day, we should really work out the thing with the particle sizes. Christoph, you welcomed me with open arms and, unbeknownst to you, I've learned a lot about Mathematica from code you've written and shared with me. And, of course, you were always willing to discuss every FIB question I could come up with. I wish you the best of luck in the times to come, and that you make the right decisions. A person that did not greet me with open arms when I came, but did so the moment he arrived, is Nico. I have no idea how you keep smiling, regardless of what life throws at you, and greatly admire your optimism. I look forward to seeing you soon in Berkeley!

There are people I thank because I enjoyed interacting with them on a personal level, people I thank because I enjoyed working with them and people who offered both. Markus and Steffen, you definitely belong in the third category. I learned all about the practical aspects of TEM from you. And you both supported me far beyond what I could expect from you, even offering me your phone numbers in case something went wrong while measuring evenings or on the weekend (luckily, it never did). Steffen, you were the most pleasant neighbor anyone could ever hope for and I will miss you coming into the office and having a chat. How those manage to turn into conversations of hours, all while we both have to get work done, is beyond me.

Water splitting is a vast field and I would have been overwhelmed in the beginning had it not been for Halina. You patiently answered all my questions and we spent more than one conference (or Ph.D. defense) having a drink together and talking about everything from the inane ("So… British people are incredibly polite, right? So, how do they, you know, meet someone?") to the sophistimacated ("So that's essentially a really simple differential equation, we just need good parameters for…"). If I continue with people who've helped me from the beginning, I need to mention Ilina, who synthesized both the first cross-section I prepared during my Ph.D. and the last. Ilina, you've been here for most of my Ph.D. and it has been an absolute joy and privilege to work with you. And not just working, but truly everything, down to sitting next to you at yet another conference and sharing a piece of chocolate, has been wonderful. In contrast to these two, I've only known Alex for roughly a year. A late arrival, but a great one. Alex, I wish I could have spent more time with you, both working and not, and raised many more glasses to the late Sir Terry. The last people I need to thank from the group of Thomas Bein are Hans, Ksenia and Yujing – I learnt a lot from all of you and am glad that I got to work with you.

The kick-off meeting of my project took me to a scenic castle in Pommersfelden, and there I met Michael. And since this conference, I've had the pleasure of working with him on what were some of the most beautiful samples I ever inserted into the TEM. I thank him for his patience when the sample preparation turned out challenging and took a lot longer than expected, and for being able to work with and learn from someone with his experience. However, he was not the only one I met in this collaboration and I also need to thank Sandra. As you are a physicist by training and therefore always offer a different point of view, I truly enjoyed our scientific conversations. And apart from the science? You are one of the kindest, gentlest people I have met and I'm glad that we are still jointly working on other topics. Within this collaboration, I also need to thank Angela Kruth, Volker Brüser and Henrik Junge, who fall into the category of people whom I wish I could have known better.

I've collaborated with three different groups, and gained a lot from each of these experiences. However, the collaboration with Craig Carter has been the one that has had the greatest impact on my life and which has broadened my horizon in truly unexpected ways. When I first met you in Istanbul, you asked me how I would enter the US illegally and stay undetected for a month. Since then, I've enjoyed every single interaction I've had with you, and the week spent in your castle in France must have been one of the most relaxing I've ever had. Nothing quite like sitting in the sun-lit living room and having a panaché while trying to fix code. Through Craig, I've also had the pleasure of working with Rachel Zucker –no words are necessary here – and Jennie Zheng. Who knew that Germany would win 7-1 against Brazil, all while we were just trying to have dinner at the Laotian place? The exhilarating atmosphere of this moment captured perfectly how much I enjoyed spending time with all of you.

I have now used a lot of words thanking all the people I've worked with. But the Ph.D. time is a stressful time (People have told me that you have to be a bit of a sadist to do that to yourself…) and I would be negligent if I did not express gratitude towards all my friends who gave me emotional support. They are too numerous to list (who am I kidding? I'm not a very social person and they are not that many. However, I do not want to forget and thereby insult anyone) and in many cases have already been listed above. And if I mention my friends, I also need to thank my family for supporting me for many, many years. I would not be where I am without you.

In the acknowledgment section of my Master's thesis, I wrote that I'd be back and delivered on that promise (given my traveling, several dozen times over). In that time, I've met some truly great people, shared many memorable experiences and gained new friends. I wish I could make the same promise this time and it saddens me that I can't. But I am sure that the experiences I've made will not be forgotten, the lessons you've taught me worth it, and the friends I've gained not lost. Thank you all for everything.